Symmetry - Breaking Charge Transfer, Intersystem Crossing and Other Ultrafast Processes in Chromophore Aggregates

Dissertation

In fulfillment of the requirements for the degree of

Doktor rerum naturalium (**Dr. rer. nat**)

Submitted to

Fachbereich 09: Chemie, Pharmazie, Geographie und Geowissenschaften

JOHANNES GUTENBERG UNIVERSITY, MAINZ

This doctoral thesis has been carried out at the

MAX-PLANCK-INSTITUTE FOR POLYMER RESEARCH, MAINZ

Esther del Pino Rosendo

Born in Madrid, Spain

Mainz, 2024

Dean: Univ.-Prof. Dr. Eva Rentschler

1. Reviewer: Prof Dr.

Molecular Electronics

Max Planck Institute for Polymer Research, Mainz

2. Reviewer: Prof Dr.

Institute of Chemistry

Johannes Gutenberg-University, Mainz

Affidavit

I hereby declare that I wrote the dissertation submitted without any unauthorized external assistance and used only sources acknowledged in the work. All textual passages appropriated verbatim or paraphrased from published and unpublished texts, as well as all information obtained from oral sources, are duly indicated and listed following bibliographical rules. In carrying out this research, I complied with the laws of standard scientific practice as formulated in the statutes of Johannes Gutenberg-University Mainz to ensure standard scientific practice.

Mainz, 11. 07. 2024 _____

Esther del Pino Rosendo

Acknowledgments

Science will not happen without at least a good advisor, a good colleague, and a good friend. Luckily, I have plenty of those.

Mainz, Berlin, February – October 2023

Table of Contents

Chapter 1

Introduction and Scope

1.1 Introduction

This dissertation examines light-matter interactions through optical spectroscopy. Light, modulated by a laser system, interacts with matter, whose changes in energy states form the basis of the functioning of organic semiconductors. This thesis focuses on light-matter interaction in chromophore aggregates of organic semiconductors (OSCs). OSCs are being studied and utilized for a broad range of applications, including solar electricity,[1,2] solar fuel production,[3,4] light-emitting diodes,[5–7], and transistors.[8,9] The π-conjugated (section 2.1.3) core or backbone of these materials imparts attractive light-absorption and semiconducting properties. In the thin films often used for optoelectronics, these molecules form aggregates or crystalline structures based on the π-stacking interactions (section 2.4.1), which can significantly impact functional properties. [10–12] Neighboring molecules experience electronic and vibrational coupling interactions (section 2.3.1) that determine their photoactive energy landscape and mediate processes such as light harvesting, charge separation, and charge transport (section 2.4).

Earlier work established the molecular exciton model (section 2.2) to understand how chromophore packing impacts absorption properties through Coulombic coupling interactions (section 2.4.2.1).[13–18] More recently, this model is being extended to consider the significant wavefunction overlap afforded in tightly packed (~3.5 Å) π-stacking arrangements, which can allow for short-range charge-transfer (CT) (section 2.2.2) interactions as well.[19–24] These intermolecular CT interactions can mix with the local intramolecular Frenkel excitons, modifying the potential energy landscape, light harvesting, and charge transport properties. Frenkel-CT mixing (section 2.4.3) has been observed in various π-stacked organic chromophore systems, including pentacene,[22,25–28] perylene derivatives,[29–34] squaraines (chapter 5),[35–37] and also in phthalocyanines (chapter 4). [5,38–46] This mixing has been purported to influence photophysical mechanisms, such as singlet fission (section 5.2) and the formation of free charge carriers via symmetry-breaking (section 4.3.1.3).

1.2 Scope and Motivation

This dissertation begins with a theoretical background provided in Chapter 2, where Molecular Orbital theory is discussed, focusing on π-conjugated orbitals. The chapter also addresses the subsequent π-stacking of molecules and the interactions derived from there. Intramolecular Frenkel excitons and intermolecular Charge Transfer excitons are elucidated through the lens of the Exciton Model, along with the effects of their intermixing.

Chapter 3 outlines the experimental methods employed, provides theoretical background, and describes the setups. It offers an overview of the fundamentals of linear spectroscopy: absorption and fluorescence. Additionally, the chapter provides an in-depth discussion of time-resolved spectroscopy using pulsed laser systems and the methodology for data collection and analysis.

Chapter 4 studies how intermolecular interactions in π-stacked chromophores strongly influence their photophysical properties and function in photonic applications. The photoexcited dynamics of the small molecule semiconductor copper phthalocyanine (CuPc) are characterized in solution and thin film, the latter comprising two different π-stacked architectures, α-CuPc and β-CuPc. In solution, CuPc undergoes ultrafast intersystem crossing (ISC) to the triplet excited state. In the solid state, both α-CuPc and β-CuPc morphologies exhibit a mixing between Frenkel and charge-transfer excitons (Frenkel-CT mixing). This mixing influences the photophysical properties differently based on morphology. In addition to ISC, α-CuPc demonstrates symmetry-breaking charge transfer, which depends on the excitation wavelength. This mechanism is not observed in β-CuPc. These results elucidate how molecular organization mediates the balance of competitive photoexcited decay mechanisms in organic semiconductors.

Chapter 5 presents squaraine aggregates slip stacked and in amorphous form. The effect of aggregation of n-alkyl SQ can be seen when, upon photoexcitation, SQ relax through a complex pathway that involves variable charge transfer character that decreases for longer alkyl chain length. The possibility of excitation and decay to triplet states is also explored because, due to the weak SOC in SQ, the triplets are not expected to be from ISC but eventually from the spin-allowed Singlet Fission process; it is usually CT mediated.

Chapter 2

Theoretical Background

Nothing in life is to be feared; it is only to be understood.

M. Curie [47]

2.1 Molecular Orbital Theory

The 20th century began by breaking away from the concept of Classical Physics and marked a turning point in how we understand the light-matter interaction: Quantum Mechanics. Key figures contributed to this transformation. Max Planck with the Planck constant as a part of the resolution of the black-body radiation problem in 1900.[48] Albert Einstein and the photoelectric effect in 1905, describing electron emission from materials exposed to electromagnetic radiation.[49] In 1913, Niels Bohr proposed his Atomic Model, which suggested quantized orbits for electrons revolving around the atomic nucleus.[50] These contributions laid the crucial groundwork for understanding microscopic phenomena. Almost exactly a hundred years ago, this field was at its peak when De Broglie proposed that particles, such as electrons, could exhibit properties similar to light waves in his doctoral thesis in 1924.[51] The Wave-particle Duality was followed by the publication in 1926 of the most well-known linear partial differential equation, that describes the behavior of the wave function and derives electron energies associated with those wave functions, by Erwin Schrödinger.[52] Born and Oppenheimer published their approximation in 1927, in which the heavier atomic nuclei are treated as effectively stationary compared to the fast-moving electrons, thereby allowing for the Schrödinger equation to be solved separately for the nucleus and the electrons and simplifying the mathematical treatment of molecular behavior.[53,54] Later, in this successful decade, Heisenberg introduced the Uncertainty Principle, and different theories emerged to explain chemical bonding, such as valence bonds.[55] One relevant noun, the word *orbital*, was introduced by Robert Mulliken in 1932,[56] to name the density distribution of electrons in molecules, a concept introduced by Hund. With Hund and Mulliken as the leading promoters, the Molecular Orbital theory was accepted in 1933 as a way to understand molecules' electronic structure and properties using quantum mechanics. It is no surprise that Mulliken was awarded the 1966 Nobel Prize for Chemistry for this theory.[57,58] This section introduces the relevant concepts of Molecular Orbital theory that are the basis of the assumptions from the present work.

2.1.1 Fundaments of Molecular Orbital Theory

The Molecular Orbital (MO) theory in quantum chemistry is a sophisticated model for understanding chemical bonds commonly considered more potent than Lewis- and valence bond theories for predicting molecular properties.

A chemical bond is established when two atoms can share electrons. During this process, atoms can share a maximum of six electrons, forming singular, double, and triple bonds. Molecular Orbital theory describes the behavior of the electrons in a molecule via combinations of the individual atomic wavefunctions, Ψ, from the Schrödinger Equation. The atomic wavefunctions give the probability of finding a valence electron in a specific region of space, delimited by the quantization of the electron energy, and are called atomic *orbitals*. The linear combination of atomic orbitals results in molecular orbitals, Ψ^2, where the electron is localized not around individual atoms but rather occupies molecular orbitals that extend over the entire molecule.

Combining atomic orbitals to form molecular orbitals is known as molecular orbital mixing or hybridization. This approximation can be used when three factors are considered. Firstly, the distance between atoms must be small enough to enable atomic orbital overlap but not so small that the nuclei do not repel each other.

Secondly, for a successful atomic orbital interaction, the symmetry of the orbitals is a crucial factor because the probability of finding an electron between the nuclei must be high. It is important to remember that when orbitals combine, the number of orbitals must be conserved after the operation. This is given by the fact that the functions that define the electron density describe a wave. Thus, in Molecular Orbital Theory, electrons are considered to have a wave-like behavior. Therefore, the phase plays an important role when combined, which affects the total orbital energy.

The energy of the atomic orbitals is the third factor to consider in forming molecular orbitals. If the atomic orbitals' energies are similar, the combination will be successful, and the wavefunctions will be in-phase, resulting in the most stable bonding with lower energy than the atomic orbitals individually, producing regions with a high probability

of finding electrons; this is called a *bonding molecular orbital (MO)*. This is because an attractive force is created when electrons are added to these orbitals, holding the molecule together. In the same way, if the energies of the atomic orbitals are very different, the bonding interactions will tend to be less stable, and the higher the energy difference, the lower the stability. In this way, when the wavefunctions are out-of-phase, the combination results in destructive interference, which can be seen as a node, meaning this is a region of the space where no electrons can be found. This is the case of *antibonding molecular orbitals (MO*)*, named after the effect of nuclei repulsion due to the resultant force. Therefore, those molecular orbitals are higher in energy than the constituent atomic ones.

Electrons occupy the lower-energy bonding orbitals first, following Aufbau and Pauli's exclusion principles. The distribution of electrons in these molecular orbitals determines the molecular properties, including bond length, bond strength, and chemical reactivity. MO theory allows for predicting and interpreting various molecular phenomena, such as molecular stability, bond types (sigma and pi bonds), and unpaired electrons (radicals). It provides insights into the overall electronic structure and spectroscopic properties of molecules.[59]

2.1.2 Molecular Orbitals

To understand how Molecular Orbital Theory approaches molecular orbitals regarding shape, energy, and position, it is necessary first to introduce the essential parameters that define atomic orbitals. Each orbital is associated with a specific energy level and has a unique shape and orientation, given by quantum numbers. Quantum numbers help determine the probable location of an electron in an atom.

The principal quantum number, *n*, represents the energy level of the orbital and determines its size. The azimuthal quantum number, ℓ, defines the shape of the orbital and depends on the value of the principal quantum number. It can have values ranging from 0 to (n-1) and determines the subshell type. A subshell refers to orbitals with the same principal and azimuthal quantum numbers. The values of ℓ are labeled using the letters s, p, d, and f, corresponding to different shapes of orbitals. The magnetic

quantum number, *m*, specifies the orbital orientation in space. It can have integer values of -1, 0, or 1, from -ℓ to + ℓ. The value of ℓ determines the number of orbitals within a subshell.

This work is centered on organic semiconductors, where the interaction between p atomic orbitals is significant. While the s orbital is spherical and has no angular nodes, the p orbitals are dumbbell-shaped and have a nodal plane passing through the nucleus. There are three p orbitals: p_x, p_y, and p_z. The combinations of those can be of two types. Sigma (σ) orbitals are formed when the p orbitals overlap head-to-head, meaning the nuclei of the two atoms are directly aligned along the internuclear axis. Sigma bonds are the strongest type of covalent bonds, which are the bonds where the valence electrons are shared between the atoms forming a molecule.

When atomic orbitals overlap side-by-side, meaning the nuclei of the two atoms are offset from the internuclear axis, π - orbitals are formed. In the case of orbitals combining in phase, in section 2.1.1 defined as bonding-type, σ bonds are more robust than π bonds because they have a more significant overlap of atomic orbitals, and the electron density is concentrated along the internuclear axis, leading to greater stability. π - bonds are weaker because the electron density is more spread out and less concentrated along the internuclear axis. The molecular orbitals that constitute the organic semiconductor are the type of π, but the particular case of π- π-conjugated orbitals will be explained in detail in the next section, 2.1.3.

2.1.3 π - Conjugated Orbitals

MO theory elucidates the phenomenon of electron delocalization within *conjugated systems* composed of pi (π) orbitals, commonly referred to as π -π-conjugated orbitals. These systems consist of combinations of p orbitals from atoms, such as oxygen, nitrogen, and carbon atoms, that are in a chain or a ring with *alternating* single and double bonds. A double bond is formed when two electron pairs are shared between two atoms. It is stronger and shorter (approximately 1.34 Å in the case of Carbon double bonds) than a single bond (approximately 1.54 Å, also for C-C) due to the more significant number of shared electrons and the stronger electrostatic attraction between the bonded nuclei. When the double bonds within the chain are separated

from each other by more than a single bond length, they are referred to as isolated bonds. These molecular orbitals result from the hybridization that occurs when atomic orbitals of different types, such as s, p, or d orbitals, mix to form a set of hybrid orbitals with various shapes and energies that would interfere with the overlapping of parallel p orbitals.

In conjugated systems, characterized by a single degree of π bonding between atoms connected by single bonds, the bond length is shorter than that observed in isolated single bonds. Moreover, in contradiction to expectations within the framework of Valence Bond Theory—where electrons are confined to specific orbitals, independent from one another—there is an absence of rotation within the molecule along the single-bond axis. This characteristic originates from the linear combination of atomic orbitals and the conjugation of the ensuing molecular orbitals, culminating in a system wherein electrons, denoted as *π-conjugated electrons*, traverse unimpededly along the π orbitals. Such movement is the delocalization of the electrons, and the electron density is distributed throughout the entire system, irrespective of the nature of the atomic bond. This delocalization further facilitates *resonance*, a phenomenon characterized by the rapid oscillation of electrons between diverse bonding configurations, which serves to stabilize the molecule and results in orbitals possessing lower energy than those identified in non-conjugated systems. This effect diminishes the system's energy in the case of cyclic molecules such as benzene.

An elementary example of a conjugated system is the 1,3 – butadiene. It has four carbons connected with alternating double bonds. Figure 1 shows the structure of this molecule below the energy diagram of the system. In the left part of the diagram, the four p_z atomic orbitals are separately shown, with an electron despaired in each one. The arbitrary color map shows the sign of the wave function and highlights the electron density around the nuclei. Following Molecular Orbital theory, the right part of Figure 1 presents the result of the combination side-by-side of the four p atomic orbitals, namely another four π molecular orbitals. The relative energy of the orbitals is given to the energy of the atomic system. It shows that from lower to higher energy, the molecular orbitals from a higher number of constructive interactions (dashed horizontal

lines) to a higher number of nodes imply destructive interactions (dashed vertical lines). With lower energy than the original p atomic orbitals, there are two bonding orbitals, π_1, and π_2, with four constructive interactions and with a node in between, respectively, and two antibonding orbitals, π_3* with two nodes and π_4* with no constructive interaction and four nodes. The Aufbau principle states that the molecule's electrons in the ground state first populate the π_1 and π_2 orbitals. This explains why the total energy of the conjugated system is lower than would be expected if the four atomic orbitals would not combine.

One of the properties of extensive chains or rings of conjugated π-orbitals is that they are responsible for the colors of the molecules. The conjugated part of the molecule is referred to as a chromophore, derived from the Greek words: 'chroma,' meaning color, and 'phoreas,' signifying “bearing.“ Utilizing spectroscopy techniques (section 3.1), the color arising from the pronounced absorption of light by π-conjugated electrons in both the visible and ultraviolet regions of the electromagnetic spectrum during transitions to higher energy levels can be analyzed. For instance, in the case of 1,3-butadiene, the excited electrons will occupy the antibonding π* orbitals. This transition will be elaborated upon in subsequent section 2.1.6. Of paramount significance to the present thesis is the fact that chromophores constitute a fundamental component of organic semiconductors.[60,61]

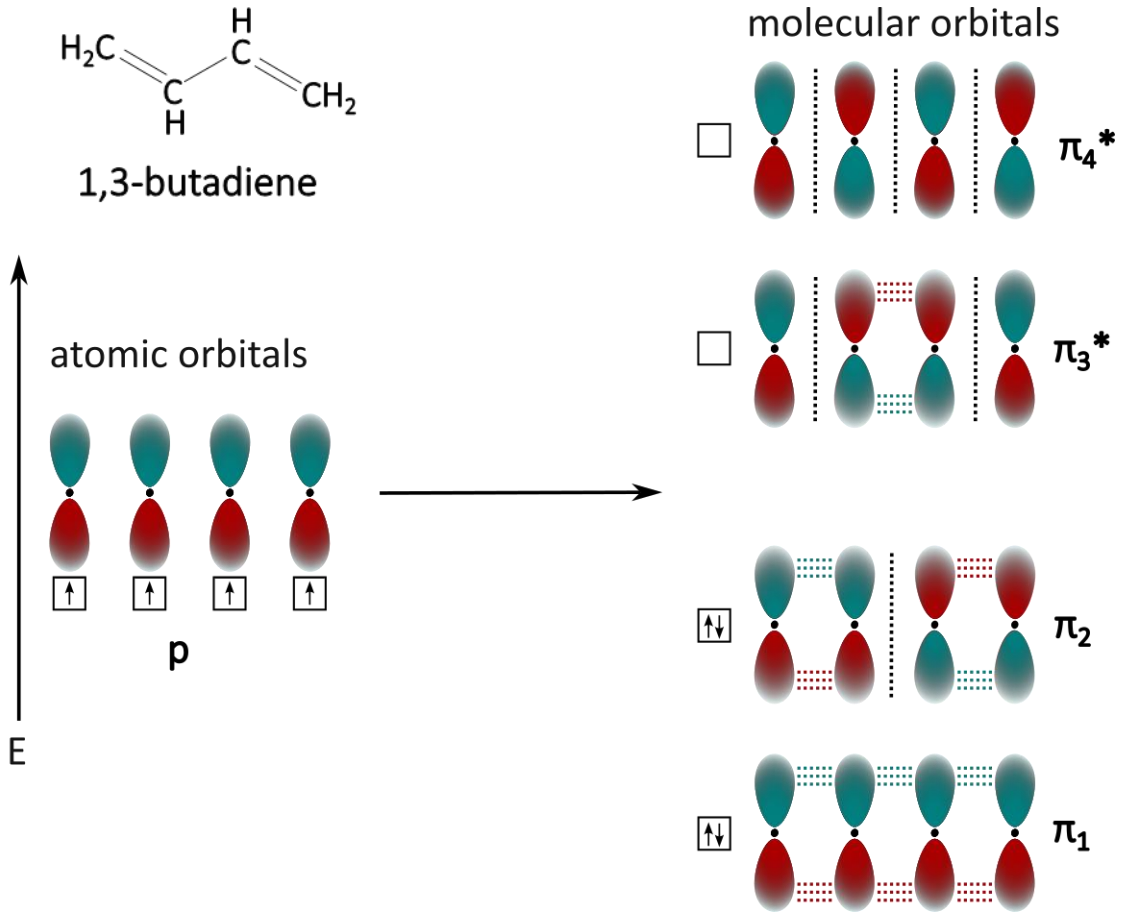

Figure 1: Energetic distribution of the atomic p orbitals versus the molecular π orbitals from 1,3-butadiene. Chemical structure (upper left). With an arbitrary color choice to symbolize the parity of the wavefunctions describing the orbitals. The Carbon atoms are black dots, and the atomic p-orbitals of the four Carbon atoms with the electron up-spin are shown below left. To the right are molecular π orbitals, from the less energetic, π_1, to the highest, π_4. Where π_1 has bonding type and is fully occupied (spin arrows), the dashed horizontal lines mean the four p orbitals overlap. The next, with higher energy but still less than the p orbitals individually, is the bonding π_2, with two pairs of overlapping orbitals and a node in between (dashed vertical black line). Antibonding - unoccupied- π_3^* and π_4^* have higher energy than the individual p orbitals. With two nodes and a single overlap, π_3^*. Three nodes and lack of overlapping have π_4^*.

2.1.4 Spin-Orbit Coupling

In the intricate field of Molecular Orbital Theory, one of the key interactions that cannot be neglected is spin-orbit coupling (SOC), which is enhanced in π-conjugated systems. Here, the electron's intrinsic spin and its orbital motion around the nucleus are interdependent phenomena. As an electron orbits the nucleus, it is subject to the electric field of the protons in the nucleus. However, the relativistic nature of the phenomenon must be considered: from the electron's frame of reference, which is moving, this electric field appears partially as a magnetic field due to those relativistic effects, as described by Special Relativity. This magnetic field interacts with the intrinsic magnetic dipole moment associated with the electron's spin. This interaction between the electron's orbital motion and its spin is called spin-orbit coupling. This influences the energy levels of the atom or a molecule, causing what is known as *fine structure* splitting of energy levels.

The strength of the spin-orbit interaction is proportional to the product of the electron's spin angular momentum operator, $\mathbf{S}$, and the orbital angular momentum operator, $\mathbf{L}$, and it is typically given by the Hamiltonian: $\mathbf{H}_{SOC} = ½\, \xi(r)\, (\mathbf{J}^2 - \mathbf{L}^2 - \mathbf{S}^2)$, where $\xi(r)$ is the spin-orbit coupling constant, dependent on the radial distance from the nucleus. $\mathbf{J}$ is the total angular momentum of the electron. The energy levels split comes from $\mathbf{J} = \mathbf{L} + \mathbf{S}$, and the related additional quantum number is j (quantum numbers in section 2.1.2).[62]

SOC is particularly pronounced in heavy elements, where the greater nuclear charge leads to higher electron velocities and stronger relativistic effects.[63] However, even in π-conjugated systems composed primarily of light elements such as carbon, the effect of SOC becomes substantial. This is due to the delocalized nature of π-electrons. The delocalization provides a pathway for communication and interaction of the electrons over extended molecular distances, giving rise to complex, delocalized spin states.[64]

SOC has significant implications for the electronic and optical properties of π-conjugated systems. Understanding this effect requires a deeper examination of the intrinsic properties of electrons, precisely their spin, a form of intrinsic angular momentum. This angular momentum is quantized, meaning it can only take on specific

discrete values. For an electron, these values are S = +1/2 and −1/2. The total spin quantum number, or spin angular momentum, of a system, S (where $S^2 = \mathbf{S} \cdot \mathbf{S}$), is dictated by the spin states of the electrons involved. These spin states can either align, forming a **triplet state**, T, with a total spin of S = +1, 0, −1, or anti-align, forming a **singlet state**, S, with a spin angular momentum of S = 0. Depending on this alignment of the spins, electrons can exhibit different multiplicities. The **multiplicity**, M, is the number of possible spin states of a particle or system associated with a specific electronic configuration of a molecule. Specifically, it refers to the number of orientations the total spin can take in a magnetic field. It is determined by its total spin quantum number and is given by $M = 2S + 1$. Therefore, the multiplicity of a singlet state is M(S) = 1. Since all electrons are paired in a singlet state, there is no net magnetic moment, and the energy of interaction between different spin states is generally low. In the case of a triplet state, the multiplicity is M(T) = 3, as there are two unpaired electrons, and the system has a net magnetic moment.[65]

2.1.5 How to populate orbitals

It could not have happened at another time but in the golden decade of Quantum Mechanics, when the rules that explained how electrons must occupy orbitals were settled. In the 1920s, **Aufbau's principle** was established, stating that electrons fill orbitals in order of increasing energy: lower energy orbitals are filled before higher energy ones.[66] **Pauli's exclusion principle**, from 1925, is a fundamental principle in quantum mechanics that ensures that there cannot be two identical electrons (valid for the whole set of fermions) occupying the same quantum state simultaneously. If two electrons are in the same system, they must have different quantum numbers. The exclusion principle ensures that no more than two electrons can occupy a single orbital and must have opposite spins: one spin-up and the other spin-down. This is why each orbital can accommodate a maximum of two electrons. It is a consequence of the indistinguishability of identical particles and the antisymmetric nature of their wavefunctions.[67] In 1927, **Hund's rules** specify that when multiple orbitals of the same energy level are available, electrons will first occupy empty orbitals within a subshell rather than pairing up in the same orbital. This is because electrons naturally tend to occupy different orbitals to minimize their mutual repulsion, given by their charge. The

spins must be first parallel so that electrons will enter a new empty orbital of the same subshell with the same spin (either up or down) rather than pairing up with opposite spins in the same orbital. Therefore, the term with maximum multiplicity has the lowest energy for a given electron configuration. For a given multiplicity, the term with the largest value of the total orbital angular momentum quantum number L has the lowest energy. For a specific term, in an atom where the outermost subshell is half-filled or less, the level with the lowest value of the total angular momentum quantum number J is the lowest in energy. Conversely, if the external shell is more than half-filled, the level with the highest value of J is the lowest in energy.[58,68,69]

2.1.6 Frontier Orbitals

In 1981, K. Fukui and R. Hoffmann were awarded the Nobel Prize for Chemistry for their pioneering work on the theory of chemical reactions, particularly for their development of the concept of **frontier orbitals**.[70,71] In the 1950s, Fukui proposed the Frontier Molecular Orbital theory (often abbreviated as FMO), which offers a framework for understanding the reactivity and selectivity of organic reactions. He described the importance of two types of orbitals separated by a *gap*: the highest occupied molecular orbital, HOMO, and the lowest unoccupied molecular orbital, LUMO.[60] In the case of the conjugated π orbitals, the HOMO, usually of bonding type, lower in energy than the individual atomic orbitals, is considered the orbital most relevant for chemical reactivity, as it can *donate* its electrons to other molecular orbitals. On the other hand, the LUMO is an antibonding orbital that the excited electron will occupy, as it can *accept* electrons from the HOMO. The minimum energy needed to promote an electron from the ground state to the first excited state and the energetic difference between both orbitals is known as the HOMO-LUMO Gap. The Planck-Einstein relation, $E_\gamma = h \cdot \nu = h \cdot c/\lambda \ [J/\gamma]$, describes the energy quantum of a photon, E_γ, that will be transferred to the electron, promoting it from HOMO to LUMO and, in this way, it will set the molecule in the so-called excited state. Here, h is the Planck constant, ν the photon frequency inversely proportional to its wavelength, λ.[48,49] In this work, the HOMO-LUMO energy gap will be given in wavelength units.

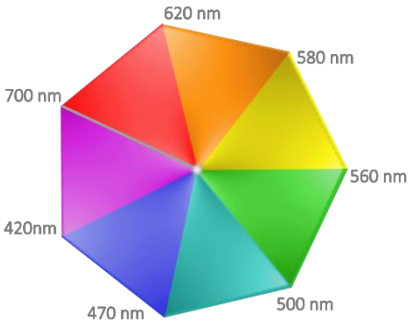

Figure 2: Color wheel.

As it was introduced in section 2.1.3, large chains of conjugated π-orbitals constitute the chromophore part of molecules, which are so-called because the energy gap for the **π -π* transition** is in the range of the 200 to 800 nm, also known as the ultraviolet to visible, uv-vis, part of the electromagnetic spectrum. Molecules with conjugated π-systems will absorb light in this range, and therefore, their visible color is given by the complementary color in the color wheel, Figure 2. An electron undergoes a HOMO to LUMO transition if it conforms to the selection rules for electromagnetic transitions (section 2.1.5). Conjugated systems containing fewer than eight conjugated double bonds primarily absorb light in the ultraviolet range and appear colorless to human perception, as is the case of the 1,3 – butadiene, in which the gap between π_2 and π_3* is 217 nm. Systems with more double bonds absorb photons with longer wavelengths, causing these compounds to exhibit colors ranging from yellow to red. However, compounds exhibiting blue or green hues typically rely on factors beyond having conjugated double bonds.[72] The wider the gap, the more stable the molecule is because this gap is the minimum energy needed to promote an electron from the ground state to the first excited state.

2.2 Exciton Theory

In Section 2.1, Molecular Orbital Theory introduced the concepts of wavefunctions - representing the probability of locating electrons in specific areas - charge distributions and an emphasis on the Pauli Exclusion Principle in the context of the electron. Now, a new particle is being introduced, which will be treated analogously to an electron: a virtual entity known as an exciton. The concept of an exciton arises from the necessity of defining excitation in the case of molecules. In the ground state of a molecule, the electron is moving inside the HOMO. When a photon excites this electron, it moves to the LUMO—this change in orbital leaves a hole – an electron vacancy - in the HOMO. The *electron* in LUMO and the *hole* in the HOMO can be considered as pair of charges with exact opposite signs that interact together following Coulomb´s Law. Their attraction leads to the formation of a bound electron-hole pair, the energy of which is lower than that of a free electron and a hole. This electronically excited state of the molecule is now considered a quasi-particle, exciton, that can move in the conjugated system without a net transfer of charge and is delocalized. The exciton is named after the term "excited ion“ and was first theorized by the physicist Yakov Frenkel in 1931.[73] Although there are many flavors of excitons the most relevant for this work is the Frenkel exciton.

In his 1959 publication, Michael Kasha summarizes three definitions for the concept of exciton. First, exciton states encompass the collective excitation of a group of atoms or molecules rather than the localized excitation of individual constituents within the assembly. Secondly, revisiting the De Broglie duality Principle, an exciton can be characterized as a wave of energy moving through a group of atoms or molecules. This wave comes from the combination of different exciton states. Finally, the exciton is a *neutral* excitation quasiparticle.[74]

2.2.1 Frenkel Exciton

The Frenkel exciton characterizes the excited state of a molecule when the electron-hole pair is confined to the same molecule without traveling to neighboring molecules. Therefore, these quasi-particles are commonly referred to as *intramolecular Frenkel*

excitons. Consequently, the molecule remains electrically neutral in both the ground and excited states. [73]

2.2.2 Charge Transfer Exciton

The Charge Transfer (CT) exciton, characterizing the excited state of a chromophore or system of chromophores, involves electron transfer from the HOMO of the donor to the LUMO of the acceptor. The **donor** molecule or chromophore segments are typically characterized by electron-donating substituents such as amino or hydroxyl groups. These groups tend to donate electron density into the π-conjugated system, lowering the energy required for electronic transitions. Conversely, **acceptor** moieties have a greater affinity for electrons. They serve to reduce the electron density in adjacent regions. These groups are generally characterized by electronegative elements or highly polarized bonds, which lead to a shift of electron density towards themselves.

The CT exciton features a spatial separation in contrast with the Frenkel exciton, where the electron-hole pair is confined within the same molecule. In *intermolecular* CT excitons, the electron localizes on the acceptor molecule and the hole on the donor molecule. However, *intramolecular* CT excitons also exist, as seen in Thermally Activated Delayed Fluorescence (TADF) systems, where this separation occurs within a single molecule.[75]

Frenkel and CT excitons are significant in optoelectronics and crucial for light absorption, energy transfer, and charge separation. Frenkel excitons are characterized by a smaller radius and higher exciton binding energy due to the strong Coulombic attraction between the electron and hole. In contrast, CT excitons have a larger radius and lower binding energy, with the electron and hole located on different molecules or parts of a molecule. This size and binding energy distinction is crucial for understanding their behavior and applications. Compared to Wannier-Mott excitons found in inorganic semiconductors, Frenkel and CT excitons have higher binding energies and smaller radii. WM excitons spread out in the crystal lattice exhibit weaker Coulombic attraction. The interaction between these excitons, particularly in mixed Frenkel-CT systems, leads to innovative applications in various technologies, including solar cells and OLEDs (Chapter 4).[76]

2.3 Spectroscopy

2.3.1 Photophysical Transitions

A photophysical transition occurs between initial and final quantum states with the same chemical structure; no bonds are made or broken. However, the states may differ in electron configuration, nuclear (vibrational) configuration, or spin configuration (triplet or singlet).

Upon absorption of a photon, an individual atom or molecule assimilates the entire quantum of energy. As a consequence, the atom or molecule undergoes a transition from its ground state, characterized by minimal energy and maximal stability, to a higher state rich in energy.

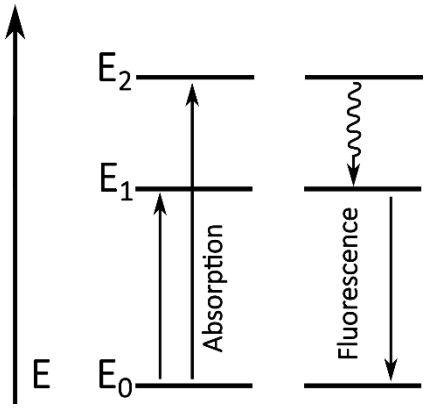

Figure 3: Diagram of Energies for ground state E_0, and excited states, E_1 and E_2 with transitions between then indicated with arrows: Absorption and fluorescence.

According to the theoretical framework proposed by Niels Bohr concerning atomic and molecular structure,[50] atoms and molecules can exist solely in a discrete series of electronic energy states, represented in Figure 3.

In spectroscopic notation, energy levels are typically denoted by horizontally arranged lines at appropriate intervals. The lowest line represents the electronic ground state, E_0, describing the atom or molecule without external excitation. Lines E_1 and E_2 denoted electronically excited states, pointing to the sole types of excited states permissible in a particular atom or molecule. Each *electronic* state may encompass one or multiple sequences of quantized *vibrational* and *rotational* states, which should be shown above each excited electronic state line. These states can be modeled as quantum harmonic oscillators in simpler molecules. Depending on the oscillation frequency, ν, and upon

solving the Schrödinger equation, distinct energy levels are obtained, valid for small vibrational quantum numbers, n, given by $E_{n(QHO)} = (n + ½)\, h\nu$. These vibrational and rotational states are often closely spaced in diatomic or polyatomic molecules, particularly those with complex structures and interactions. For these molecules, anharmonic oscillator models are more accurate, generally described by $E_{n(QAO)} = E_{n(QHO)} + x_e\, h\nu(n + ½)^2$, with x_e as the anharmonicity constant. This reflects the non-uniform energy level spacing due to the n^2 term, representing the first anharmonic correction. Higher-order corrections can be added for more accuracy, especially at higher energy levels, leading to a broader spectrum of energy levels and transitions due to complex molecular dynamics.

In diagrams like Figure 3, upward-pointing arrows depict absorption lines or bands, while downward-pointing arrows signify emission lines or bands. The quantum energy involved in either emission or absorption is directly proportional to the length of these arrows. Atoms or molecules can absorb only energy quanta that match the gaps between allowed energy states. When excited to a higher energy state, for example, to state E_1, energy can be released through a transition represented by downward arrows to a lower energy state, E_0. The wavelike arrow, from E_2 to E_1, indicates an alternative, non-radiative pathway for transition, either through energy dispersion to adjacent molecules or via conversion into vibrational energy within the excited molecule. A direct transition from E_1 to E_0 is called fluorescence, after the absorption of light, photon, or energy quantum from E_0 to E_1.

The transitions between energy levels are depicted in absorption or fluorescence **spectra**. Atomic spectra involve transitions between electronic energy levels and typically yield well-defined line spectra. The energies associated with molecular electronic spectra, usually falling within the visible or ultraviolet regions, are considerably greater than those related to vibrational spectra, commonly in the infrared range, and rotational spectra, typically in the microwave region. This adds to the complexity of electronic spectra, as transitions from many vibrational and rotational levels give rise to numerous spectral lines, forming a continuous broad *band* of frequencies that constitutes the molecular spectra.

It must be considered that upon absorbing a quantum of energy, the molecule transitions into an electronically excited state and undergoes vibrational motion. This vibration manifests itself in a change in the relative position of the atomic nuclei that constitute the molecule. However, nuclei are significantly heavier than the electrons orbiting them and move considerably slower. This implies that the impact of a photon on a molecule will almost instantaneously induce electronic excitation within a matter of femtoseconds, placing the molecule in a non-equilibrium state yet will have no immediate influence on the nuclei. The readjustment of the nuclei occurs after the electronic excitation, and this readjustment induces vibrational motion of the nuclei in the scale of picoseconds.

In 1925, in Göttingen, James Franck argued that due to the substantial mass of the atomic nuclei constituting the molecule, their relative momentum could not be affected by an electronic transition. Indeed, one year later, in the same city, Born and his pupil Oppenheimer penned the well-known approximation bearing their names, which allows, for the same reason, the consideration of processes involving electrons independently of processes involving nuclei. Hertha Sponer presented Franck's paper to her professor, Condon, in Berkeley, who shortly after that introduced a generalization of Franck's ideas, giving rise to the **Franck-Condon principle**.

This principle can be seen through an energy diagram with two potential curves in Figure 4a, which depicts the potential energy of the molecule's initial ground state, S_0, and the final excited state, S_1. The abscissa displays the distance between these two states in nuclear coordinates, r, considering a diatomic molecule in which one nucleus remains in the ground state and the other is excited, separating from the former by a non-equilibrium oscillating internuclear distance, Δr. The vibrational energy levels are labeled as v’ for the molecule in the ground state and v for the molecule in the first electronically excited state, following Franck´s paper. Unlike the quantum harmonic oscillator model where energy levels are uniformly spaced, in the anharmonic Morse potential, which better represents the molecular vibrations in the Franck-Condon principle, the spacing of energy levels, $E_{n(FC)}$, is not constant, meaning that the density of states increases as the energy increases. The energy levels become closer to each

other following: $E_{n(FC)} = E_{n(QHO)} (1- E_{n(QHO)}/4D_e)$, depending on the energy of dissociation, D_e. This results in the excited state vibrational levels being more closely spaced than those in the ground state, reflecting a more loosely bound excited state with lower energy vibrations.

Under the approximation of low temperature, the molecule initially stays at the v'= 0 vibrational level of its ground electronic state. Upon photon absorption of adequate energy, the molecule transitions to an excited electronic state, causing a shift in the equilibrium position of the molecular nuclei. In Figure 4, the dashed vertical axes represent the separation between nuclei. The vibronic transition is represented by a vertical arrow, signifying that the nuclear coordinates remain constant during this process. The probability of this transition is greater when the vibrational wave functions of the two states are more compatible with each other (e.g., having maxima at the same internuclear distance). Therefore, some vibronic transitions are more likely than others, specifically those where the internuclear distance remains unchanged. For these transitions, a vertical arrow is drawn, and they are thus referred to as *vertical transitions*, which are radiative transitions.

The scalar product gives the transition probability: $P = \langle\varphi'|\boldsymbol{\mu}|\varphi\rangle$ of the final state, $|\varphi'\rangle$, and the initial $|\varphi\rangle$. The dipole operator $\boldsymbol{\mu}$ comprises the electron charge and position, d, and the charge and position of the atomic nuclei, r. The wave function can be approximately expressed as a product of the electronic and vibrational wave functions: $\varphi = \varphi_e(d)\ \varphi_v(r)$, where ϕ_e depends only on the electron coordinates and φ_v only on the nuclear coordinates, as Born-Oppenheimer approximation dictates. This allows for deriving the Franck-Condon principle by considering each term independent from the other. The resultant simplified expression consists of a product of two terms:

$$P = \langle\varphi'|\boldsymbol{\mu}|\varphi\rangle = \langle\varphi'_v|\langle\varphi'_e|\boldsymbol{\mu}|\varphi_e\rangle|\varphi_v\rangle = \langle\varphi'_v|\varphi_v\rangle\ \langle\varphi'_e|\boldsymbol{\mu}|\langle\varphi_e\rangle \qquad [1]$$

The second one is the transition dipole moment, which is determined by the orbital angular momentum and spin selection rules for electric dipole radiation. It depends only on the electronic component, and the other is the *overlap integral*, $S = \langle\varphi'_v|\varphi_v\rangle$, which square is the **Franck-Condon factor**, F, and is solely dependent on the nuclear coordinates. It reflects the overlap between the vibrational wave functions of the

electronic states involved in the transition (ground and excited states). Consequently, vibronic transitions are more intense when the vibrational wave functions overlap to a greater extent. This is manifested in the magnitude of the Franck-Condon factor: F = 1 maximum overlap to F = 0, no overlap. The intensity of the transition is the square of the transition probability, P, which is the intensity of the absorption or emission spectra, I.

In practical terms, the Franck-Condon principle proves essential for providing insight into the similarity between an excited-state structure and a ground-state structure. Understanding the nature of the molecule in question, such as its rigidity, allows for confidence in predicting transitions from the zero vibrational level of the ground state to the zero vibrational level of the excited state, 0 – 0 transition, mainly when the molecule, like it is in the case of some chromophores, is unlikely to undergo significant structural changes upon photoexcitation. The greater the molecular flexibility, the more critical the nuclear displacement. According to the Franck-Condon principle, transitions to higher vibronic levels will be the only ones permitted, as illustrated in Figure 4b, i.e., the *selection rule* for the vibrational transition is $\Delta v = +1$.

Spin-orbit coupling, charge recombination processes, and vibronic transitions governed by the Franck-Condon principle collectively shape the molecular absorption and emission spectra, which may feature one or multiple peaks and various shoulders.[53,63,77,78]

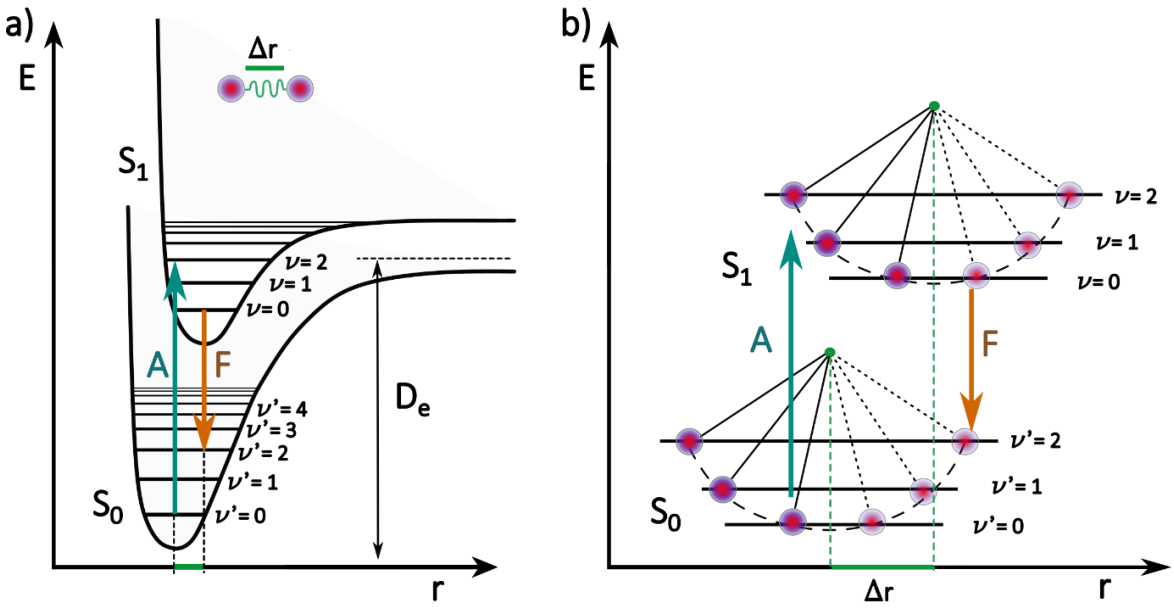

Figure 4: Energy diagram illustrating the Franck-Condon principle, in the abscissa, the internuclear distance, r. a) Two Morse potential curves depict the potential energy of a diatomic molecule, with one atom in the electronic ground state, S_0, and the other in an electronic excited state, S_1. Vibrational levels for the electronic ground state are denoted by v' for the electronic ground state and the electronically excited state by v. Upon absorption, represented by a blue arrow labeled A, the molecule transitions to the excited state, displaced by a certain intermolecular distance, Δr (green). An orange arrow signifies fluorescence. The internuclear distance changes along the potential curve due to vibrations between both nuclei (b). To clarify the concept of a vertical transition, part b) simplifies the potential curve and shows the nuclear positions: allowed vertical transitions between specific vibronic levels are those that do not necessitate a change in position.

2.3.2 Jablonski Diagram

It was in 1933 when Aleksander Jabłoński introduced a diagram that was to become a cornerstone in our understanding of molecular energy states when they interact with light alongside their associated transitions.[79] Nowadays, an improved version of the first diagram is used. As shown in Figure 5, the Jablonski diagram organizes the electronic or excitonic states of a molecule vertically based on their energy. It groups them horizontally in terms of spin multiplicity so that the left half is for the singlet manifold,

S, and the right half shows the triplet manifold, T. The horizontal thick lines denote the vibrational ground states of each electronic state, while thinner lines represent higher vibrational states. The energy gap between the horizontal lines, often referred to as a band, resembles the concept of band gaps in solid-state physics. A band gap is a range of energy levels without electron states in solid-state materials. It represents the energy difference between the valence band's top and the conduction band's bottom, effectively separating filled electron states from empty or partially filled states. This concept, named by Jabłoński as an absorption band, is analogous to these principles, reflecting similar energy transitions.

The directional notations in the diagram, including solid arrows for **radiative transitions** and dashed arrows for nonradiative transitions, further illustrate the complex interactions of energy states. These symbols represent various processes such as absorption and emission phenomena like **fluorescence**, singlet-singlet ($S_1 \rightarrow S_0$) emission and **phosphorescence**, triplet-singlet ($T_1 \rightarrow S_0$) emission, or even the forbidden transitions that include nonradiative internal conversion or intersystem crossing (sections 2.3.3.1 and 2.3.3.2). [79–86]

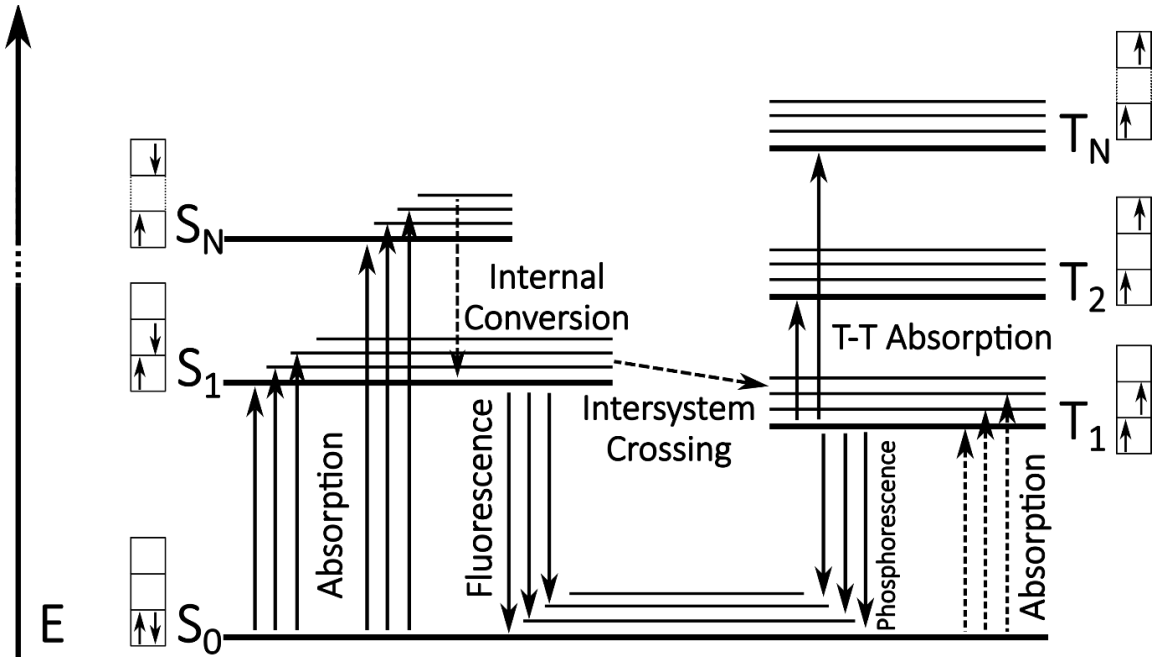

Figure 5: Jablonski diagram of the energy levels of a molecule. The left side corresponds to the singlet manifold. Light absorption will cause the excitation of an uncertain, excited

singlet state, S_N, that will relax through internal conversion to the lowest excited singlet state, S_1. From there, two types of decay can happen: following Kasha´s rule, from S_1 to ground singlet state, S_0, known as fluorescence. Second is the forbidden spin conversion from the singlet to the triplet manifold, on the right side of the diagram, that will resolve in phosphoresce, i.e., the slowest decay from the lowest excited triplet state to the singlet, T_1 to S_0. Other absorption processes in the triplet manifold are the triplet-to-triplet absorption and the absorption directly to the triplet state. The solid lines indicate radiative transitions. Dashed lines correspond to non-radiative transitions. Bold horizontal lines are the main energy levels. Thin lines point to the vibrational states of each multiplicity. The spin states direction and energy are given in the squares next to the energy states. (Adapted from [85])

The spin direction is also given in Figure 5. Since all electron spins are matched in pairs in the singlet state, the excited electron's spin is complementary to that of the ground-state electron. This phenomenon adheres to the Pauli exclusion principle, section 2.1.5. However, a triplet state involves an unpaired, excited electron whose spin parallels the ground-state electron's. Because a triplet state demands an extra prohibited spin transition, the likelihood of its formation upon radiation absorption is diminished.

2.3.3 Non-radiative Processes

A non-radiative transition requires some form of perturbation that takes the initial state and provides it with a *probability* of transitioning into the final state, p. This perturbation can be described either by a matrix, V_{fi}, wherein rows and columns represent possible wave functions for initial $|\phi\rangle$, and final states $|\phi'\rangle$. The transition rate correlates with the perturbation matrix element and the density of states in the final state. This constitutes **Fermi's Golden Rule**. This rule was enunciated in one of Fermi's Nuclear Physics classes in 1949 and is often referred to as Golden Rule number 2 of time-dependent perturbation theory; it builds upon the mathematical developments by Dirac twenty years earlier. The Fermi Golden Rule is an equation for calculating transition rates. The modified expression of the Fermi Golden Rule, here as the rate constant including a vibrational overlap or Franck-Condon factor,

$k_{i \to f} = \frac{dp(t)}{dt} = \frac{2\pi}{\hbar} V_{fi}^2 \, \rho(E_f) F$, indicates an increase in transition probability with time, reflecting the cumulative effect of the perturbation on the transition rate. The density of states, $\rho(E_f)$, accounts for the number of available final states at a given energy. Therefore, it is included because there may be more than one final state at, or in the vicinity of, the final energy, E_f. (Figure 4a).

As a result of Fermi's golden rule, rates of non-radiative transitions generally follow an *energy gap law*, where the prohibition factor follows: $F \sim e^{-\Delta E}$. Rapidly decreasing FC factors, i.e., less vibrational wavefunction overlap, with increasing ΔE between initial and final states - in particular, the ground vibrational levels of the electronic states - result in slower rates at greater ΔE.[87–89]

In 1950, Michael Kasha wrote about types of electronic transitions and emission properties in complex molecules. He then formulated that after an excitation, the state with a certain multiplicity that emits light responds to the lowest energy *excited* state of this multiplicity. This is known as the **Kasha Rule**.[90] Specifically, two non-radiative processes are derived from this rule: internal conversion and intersystem crossing.

2.3.3.1 Internal Conversion

Kasha defines internal conversion as the quick, radiation-free transition between excited electronic states with the same multiplicity. This process reduces the overall inherent photoluminescence quantum yield (PLQY) -the ratio of the number of photons emitted to the number of photons absorbed by a material. After the internal conversion, the relaxation of the lowest excited state manifests as a distinctive luminescence, lower in energy than the absorbed light. The difference between both energies is the Stokes shift,[91] enunciated in 1852 and explained by the Franck- Condon principle. The luminescence energy is irrespective of the excited state within the same multiplicity. This gives rise to the Kasha rule.[90] Following the energy gap law, IC from S_2 to the lowest excited state S_1 is a much faster process than the radiative emission from S_1 to the ground state S_0.

$\Delta E\ (S_2 - S_1) << \Delta E\ (S_1 - S_0)$.

2.3.3.2 Intersystem Crossing

The forbidden spin flip or rephase from singlet to triplet, $S_1 \rightarrow T_1$, internal conversion is called intersystem crossing (ISC). It is a nonradiative process that depends on the spin-orbit coupling. The more intense the SO coupling, the higher the transition probability. This will also be favored in the presence of external electromagnetic fields because ISC is governed by the *conservation of angular momentum*. The spin is associated with a magnetic moment; therefore, magnetic fields can influence spin. The interactions responsible for spin changes during ISC are sources or sinks of orbital or spin angular momentum. These sources can be present in another particle, a nucleus, or another set of electrons. Therefore, an external magnetic field may also play a role, as it can influence the magnetic moments associated with electron spin. However, a change in orbital configuration can also power a change in the spin state because orbital angular momentum is coupled to spin angular momentum (section 2.1.4). The SO-Hamiltonian operator, which couples a change in spin to a change in orbital configuration, depends on the atomic number as $\mathrm{H}_{SO} \sim Z^4$. A larger H facilitates faster inter-system crossing, mainly because a change in *orbital motion* at or near a heavy atom - high Z - can more readily induce spin changes, known as the *heavy atom effect*.[92] There exists another mechanism for ISC that does not necessitate the presence of a heavy atom and involves specific changes in electronic orbital configurations. **El-Sayed's rules** state that in photo-excited organic chromophores capable of forming π* excited states, ISC can be rapid and efficient. This process relies on a change in the occupancy of molecular orbitals, such as a transition from one type of orbital (e.g., p_x) to another (e.g., p_y). This orbital change is coupled with a spin flip. When there is no change in orbital configuration, singlet to triplet transitions become forbidden due to the orthogonality of the singlet and triplet wavefunctions, resulting in no overlap and, thus, weak interactions. This difference in orbital configurations is crucial in facilitating the spin-flip necessary for ISC.[93,94]

The emission and transient absorption spectra (section 3.4) hint at understanding the non-radiative relaxation processes. Phosphorescence is a slow process, in milliseconds to seconds, that identifies the lowest easily excited triplet state, T_1, favored through a high rate of internal conversion and proving the ISC. In comparison, fluorescence

happens in the scale of the nanoseconds. The PLQY can give insight into other no-radiative processes, such as internal conversion. The ratio between the phosphorescence and fluorescence lifetimes, or decay rates, shows the intersystem crossing ratio. [59,61,90,95] Aggregation can also affect intersystem crossing.[96]

2.4 Molecular Aggregation

If the beginning of the past century was particularly fruitful in Quantum Mechanics, the mid-century marked a significant era for Molecular Photochemistry. Influential figures such as Frenkel, Davydov, Kasha, McRae, and Förster, among others, contributed significantly with their theories and demonstrations, providing insight into the unique characteristics of molecular aggregates and explaining why their behavior following light absorption differs from that of individual molecules. In general, when molecules congregate through various weak intermolecular forces that are non-covalent in liquid and solid states of matter, they are called molecular aggregates. Depending on the number of molecules involved, this aggregation can occur in various forms, including dimers, oligomers, and polymers.

2.4.1 π - Stacking of molecules

In previous sections, the molecules were examined as individual units called monomers. This implies that they exist in an isolated state, as observed when they are in a solution or gas phase. In these cases, the molecular interactions are *intramolecular*. However, in organic semiconductors, the molecules are not considered in isolation but rather in crystalline form. In the crystalline form, the individual molecules do not exist independently but align in a specific pattern, often near one another. This alignment results in forming a structure referred to as a "stack." The stacking configurations of molecules lead to new properties and interactions not observed in the isolated monomers. These interactions are *intermolecular* and significantly impact their optical properties.

The systems analyzed here are in the *solid* state, called **molecular crystals**. Various forces, such as van der Waals forces, hydrogen bonding, π-π interactions, and electrostatic forces, govern the intermolecular interactions in the stacking of molecules. These forces collectively contribute to the stability and structure of the stacked arrangement.[16,17]

π- stacking interactions are a type of non-covalent interaction, weak interactions resulting from stacking a π-conjugated system (section 2.1.3). There are three types of

interactions, as shown in Figure 6, where a benzene molecule is shown as an example. Benzene has the p orbital, which is unhybridized, oriented perpendicular to the plane of the molecule, and is responsible for forming the π-conjugated system: When the plane of the molecules interacts in a parallel orientation, mediated by delocalized π-electrons, that can create a weak attractive force between the two rings. The case of a perpendicular placement of the molecular planes is the edge to face stacking. The last type of interaction is the slip stacked. This interaction occurs when the layers are not perfectly aligned and instead displaced relative to each other, creating a periodic pattern of offsets. All types of stacking are variously seen in solid-state organic electronics, such as organic photovoltaics (OPVs). Slip-stacking has been proposed to be more efficient and desirable for OPVs, but it still depends on the material.[97]

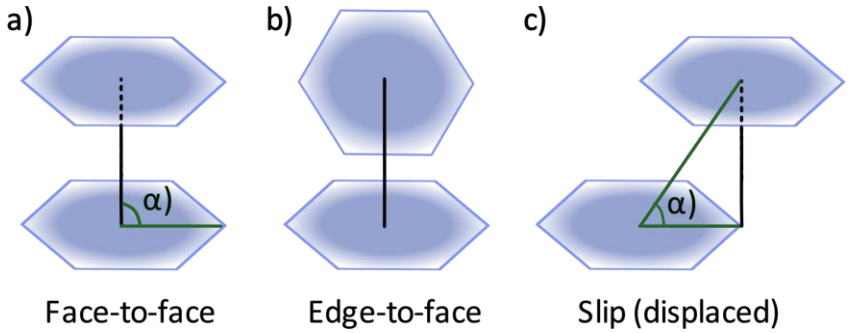

Figure 6: π-stacking types. a) represents molecules parallel to each other, face-to-face stacking. b) is the case of T-stacking or edge-to-face stacking, and c) shows molecules parallel, but the center is slightly displaced, slip-stacking.

2.4.2 Exciton Splitting

2.4.2.1 The Molecular Exciton Model of Kasha

Already in 1958, McRae, together with Michael Kasha, considered that the absorption spectra of *dye aggregates*, a group of weakly bounded molecules by non-covalent interactions like van der Waals forces, dipole-dipole interactions, and π-stacking, can exhibit significant deviation from the spectra of their corresponding monomeric pigments. Moreover, aggregation may induce notable energy level splitting, experimentally seen as shifts in the emission spectra. However, specifically, there is an amplification in the quantum yield of phosphorescence, potentially at the expense of fluorescence. Numerous demonstrations of phosphorescence enhancement have been

under conditions that promote aggregation, such as high concentrations or absorption on high polymers.[15]

Less than a decade later, in 1965, Kasha et al. presented the exciton strong-coupling model in molecular spectroscopy. This model was initially applied to aggregates of two identical molecules, known as dimers[1], and extended to polymers. It is also pertinent to what they refer to as *composite molecules*. In these systems, comprised of isolated unsaturated bonds, the molecules are connected without orbital overlap, i.e., they are not conjugated. This configuration should prevent electron migration from one molecule to another through conventional mechanisms observed in conjugated systems. Commonly, this is known as the **Exciton Model**. The model provides a quantum-mechanical description of how the excitation of a single molecule from an aggregate can be thought of as spreading throughout the aggregate, forming the exciton, or delocalized excited state. The exciton will interact and exchange energy when coupling with other excited states. The model describes the splitting of the excited state energy levels of the aggregate, those levels that in the individual molecules are non-degenerate - which in quantum mechanics means that they are well distinguishable. This coupling is similar to how atomic energy levels split due to the spin-orbit coupling, known as **exciton splitting**.

The mathematical approach of this model is also a quantum mechanical approach as it is for the Molecular Orbital theory, based on the Schrodinger Equation, in which solutions are energies and excited state wavefunctions, called *molecular exciton wavefunctions*. Those wavefunctions are distributions with the same form factor as the molecular orbital wavefunctions (section 2.1.1), but instead of describing the charge

[1] In the review of Singlet Fission by Smith and Michl, the concept of Dimer refers to isolated molecules containing two (dimer related to the quantity of two) covalently coupled chromophores. Note that covalent bounds are strong in comparison to van der Waals forces, that are considered weak forces. The confusion here is the consideration of covalent bonded chromophores as a dimer. Because, in Kasha's Exciton Model, the concept of dimer is a group of two molecules close each other forming an aggregate of two molecules, that are strongly coupled, but one could assume, that it refers to van der Waals coupling, the one intrinsic to the coupling forces between different species. Covalent bonds refer to the bond intrinsic to a molecule, the bond that put atoms together to form molecules.

distribution, they give the excitation distribution. The node in this wavefunction describes a phase relation change of transition dipoles coplanar to the molecular planes.[15] The theoretical framework presented by Kasha is based on a dimer, where one molecule is excited by a photon of light, and the other remains in the ground state. The solution for this system is the *transition energy* between the excited states of the molecules. This includes the energy difference between the individual molecule in an excited state and the ground state, but also the difference between the van der Waals interaction energy between both molecules in the ground state and the van der Waals interaction energy between one excited molecule and another molecule in the ground state, that lowers the total energy. Finally, the exciton splitting term is included, which denotes the energy interaction resulting from the exchange of excitation energy between molecules of the system. [13–18,98]

In practice, however, the Exciton Model can be considered from a *quasi-classical* point of view, centering this approach in the electrostatic interaction of the **transition dipole moments**, $\boldsymbol{\mu}$, of each molecule.[99] A transition dipole moment is the complex vector quantity associated with the transition of a particle from one energy state to another describing, in the simple case of a single molecule, how the electron cloud of a molecule changes when the molecule transitions from one electronic state to another due to the absorption or emission of light. This transition dipole moment can be understood as the product of the electron's charge and the change in the electron's position caused by the transition. The total transition dipole moment of molecular aggregates can be represented as the vector sum of the individual transition dipole moments of the component molecules that are influenced by the presence of other molecules in the aggregate due to intermolecular interactions. Therefore, this vector quantity incorporates phase factors linked to two different states. The direction of this vector illustrates the polarization of the transition, dictating how the system interacts with an electromagnetic wave of specific polarization. The intensity of the interaction is given by the square of the magnitude that arises due to the spread of charge within the system.[100] In their simplified approach, Kasha and McRae considered the Molecular Exciton Theory of Davydov. [101] They considered the direction of the transition dipole vectors of a *composite double molecule*, $\boldsymbol{\mu}_1$ and $\boldsymbol{\mu}_2$, and their in-phase or out-of-phase

arrangement, presenting four cases of their possible interactions. In the literature, *molecular transition dipole interactions* are often linked to exciton splitting, as discussed in the context of the Molecular Exciton Model of Kasha. This correlation suggests that stronger coupling between the components of the transition dipoles leads to more pronounced exciton splitting. The coupling strength is based on the **Coulomb force**, J, which in its scalar form depends on the magnitude of the involved transition dipoles and the distance between these two considered molecules, which arises from the cartesian form in Equation [2]: Coulomb coupling force between two molecules:

$$J \propto \frac{\mu_1 \mu_2}{r_{12}^3} \qquad [\ 2\ ]$$

The Coulomb interaction is precisely known for being a *long-range interaction* due to its relation: $1/r^3$.[102] The energy level shift induced by this coupling, relative to the individual excited states, is significant. The eigenvalues of the 2x2 Hamiltonian will give the energy, E_0, of each molecule. Therefore, the new possible energy levels will be defined, where the level E' is lower, and E'' is higher than the excited state of the component molecules. These shifts are displaced by the van der Waals energy, ΔE_{vdW} in Figure 7, as shown in Equation [3]: Energy level shift due to the transition dipole interaction. [103]

$$\Delta\varepsilon = E_0 \pm J = E'' - E' \qquad [\ 3\ ]$$

Considering that the two involved molecules are parallel in the same plane, the system is restricted to *two dimensions*, depending on the orientation of the transition polarization axis with respect to the long molecular axes, named *slip-angle* θ. The energy change for the new energy levels after the transition dipole interaction for a dimer is given by the Equation [4]: Exciton band splitting energy:

$$\Delta\varepsilon = \frac{2\,|\bar{M}|^2}{r_{12}^3}(1 - 3\cos^2\theta) \qquad [\ 4\ ]$$

For the case of **θ = 54.7°**, *the exciton splitting is zero*, i.e., Δε = 0, independently of the intermolecular distance, r_{12}. This is known as *magic angle*.[19] The selection rules for the allowed transitions involve taking the transition moment for the dimer, which is given by the vectorial sum: $\mathbf{M} = \boldsymbol{\mu}_1 + \boldsymbol{\mu}_2$, and gives the transition probability between the ground state and E' or E''. Therefore, only transitions with nonzero transition moments

will occur. The following sections are focused on the two frontier cases: when **θ = 0,°** called J- Aggregates, section 2.4.2.2, and when **θ = 90°**, H- aggregates, section 2.4.2.3. These cases are well defined by Equation [4] and are depicted in the schematic energy diagram from Figure 7.[15,99] The *three-dimensional* arrangement, two molecules per parallelepiped unit cell, is considered, studied by Davydov, when the transition dipoles are *oblique*, shown in the right region of the Figure 7 and developed in section 2.4.2.4. However, the newest analysis of the Molecular Exciton Theory, conducted in this century by Hestand and Spano, among others,[19,20] questions the validity of considering only long-range interactions in molecular aggregates and introduce the effects of the short-range and vibronic couplings, which will be further explained in section 2.4.2.5.

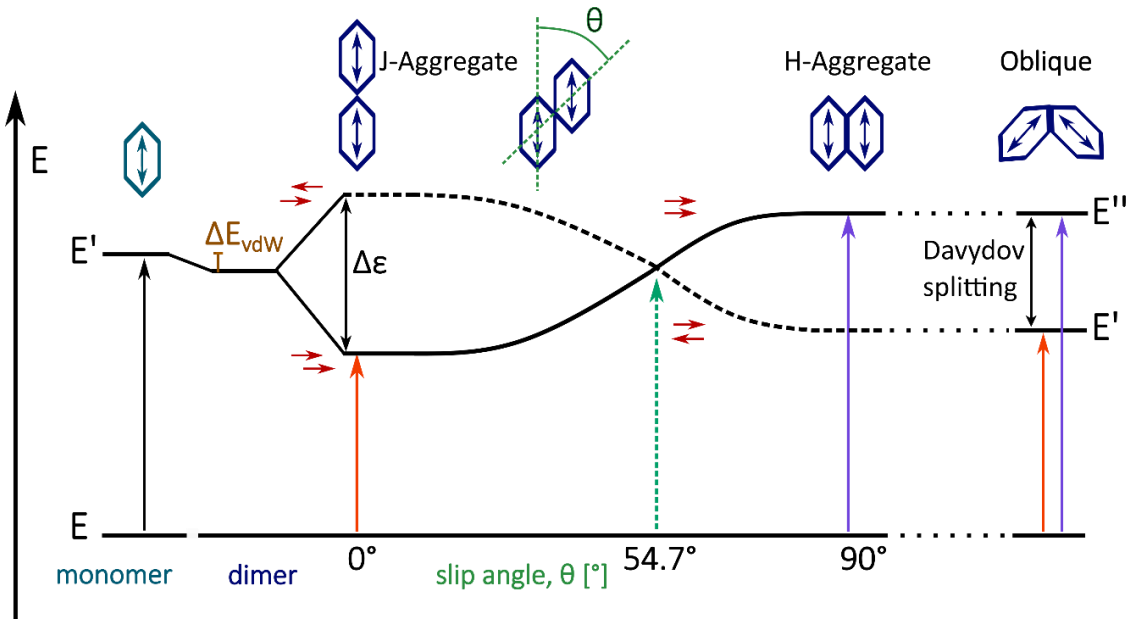

Figure 7: Energy diagram for the transition S_0 -S_1. From left to right, first, the monomer form. Middle the aggregated dimers with coplanar inclined transition dipoles, as the allowed levels depend on the angle between the transition dipoles, ϑ. The direction of the dipole is indicated by the miniature horizontal red arrows (electrostatic interaction). When the dimers are parallel aligned, the allowed excitation level is only one of the two possibilities. The magic angle, resulting from the Equation [4], is ϑ = 54.7°. If the angle is smaller than the magic angle, the lower energy level is allowed, resulting in the absorption spectra as a red-shifted J-band, section 2.4.2.2. If the angle is larger, the energy level is higher in energy, showing the allowed level in a blue-shifted H-band section 2.4.2.3. Note that in the dimer, the van der Waals forces play a role in slightly

diminishing the energy of the aggregate; ΔE_{vdW} is the difference in the interaction energies between ground and excited states. The dashed lines indicate forbidden exciton levels, and the solid lines the allowed exciton levels. On the right side, the Davydov splitting is shown in section 2.4.2.4; it appears due to the oblique arrangement of the transition dipole moments when both levels will be populated after the excitation. (Adapted from [99])

2.4.2.2 J - Aggregates

Kasha and McRae describe this case as *an in-line transition dipole: the transition polarization axis is aligned with the molecule´s long axis, commonly referred to* as head-to-tail aggregate. However, it is more common to find in-line transition dipoles when the molecule's long geometrical axes are parallel. The transition dipoles are still polarized along the unit molecule's short axis as in the in-line dimer. This is the limit case of **θ = 90°**. These structures were independently discovered by Scheibe and Jelley in the 1930s while studying solutions of pseudoisocyanine dye (PIC) and were subsequently termed **J-Aggregates**.[104–107]

As depicted with a small horizontal pair of red arrows in Figure 7, when the transition dipoles are in-phase, there is an electrostatic attraction, which is the exciton level E'; however, for out-of-phase dipoles, the repulsion leads to the forbidden state E'', due to the zero value of the transition moment for this transition. Thus, a bathochromic shift will be observed in a narrow, so-called J-band in the absorption spectrum of the dimer. According to Kasha's rule, Fluorescence is expected because it arises from the lowest excited state. [90] Extending this model to a group of N molecules in an aggregate, Kasha and McRae demonstrated that the transition dipole moment is related to the number of molecules as $\mathrm{M} \propto \sqrt{\mathrm{N}}$. [19,108]

2.4.2.3 H - Aggregates

In contrast to J-Aggregates, in this case, the transition dipoles are parallel and form a face-to-face aggregation. This leads to a hypsochromic shift (to the blue) in the energy levels, which is why these aggregates are referred to as H-aggregates. They were first found in 1936 by Scheibe, who described the formation of the case, **θ = 90°**, in a solution of PIC iodide in water.[109] When the dipoles are out-of-phase, there is an attraction that

would lower the energy, but the resulting M is zero. Therefore, this is a forbidden transition. The in-phase dipole arrangement leads to a repulsion that increases the total energy of the excited molecule, and the transition from the ground state to the exciton state E'' is allowed. Kasha reports blue shifts of about 1000 to 2500 cm^{-1} and a decrease in the fluorescence intensity. Formation of H-aggregates can also stabilize the lowest triplet state and thus may facilitate intersystem crossing.

2.4.2.4 Obliqua Aggregates: Davydov Splitting

Already in 1948, Davydov, in his Molecular Exciton theory, analyzed the particularities of the molecular aggregates.[16,17] He considered the simplification of having a molecule in a parallelepiped unit cell in which the transition dipole aligns with a certain angle to the neighboring molecule; his tedious quantum mechanical analysis of the interactions resulted in a demonstration of the resonance split, commonly known as **Davydov splitting**. As Kasha and McRae explain, in a much easier way, both arrangements of the transition dipole moments of the monomers, in-phase, attractive interaction, and out-of-phase, repulsive interaction, are allowed since the sum of them is nonzero. This means both transition from the ground state to E' and E''. Davydov cites that the energy splitting appears gradually in dependence with an increasing concentration of the molecules. The splitting is usually around 20 cm^{-1}.

Davydov also dedicated his studies to analyzing the possible ways the excited states could decay since they are in a non-equilibrium thermal state. He considered that the exciton can move through different regions of the aggregates. This phenomenon gives rise to several critical spectroscopic behaviors (section 2.3.2) that set the aggregate in a thermal equilibrium state. He pointed out that the transformation of the exciton energy into *thermal energy of emission* is just one of the few processes happening due to the energetic relaxation of the molecule, among others, like photoemission. This radiative-type emission is dependent on the structural characteristics of the aggregates. It competes with nonradiative processes, such as lattice vibrations, impurities, or the conversion of the excitation energy into *phonon* energy, quantized *modes of vibration* occurring in a rigid crystal lattice, such as the atomic lattice of a solid. The nonradiative processes are responsible for re-establishing the thermal equilibrium in an aggregate

or crystal. They depend on the coupling strength between the respective excitations and the phonon oscillations within the crystal. There is also a resonance splitting in the vibrational energy levels representing the energy levels of the *intramolecular* vibrations, the range of which is in the infrared (thermal), which is affected by the transition dipole moment interaction. Specifically, the infrared absorption bands exhibit this resonance splitting in crystals with more than one molecule per unit cell.[101] These vibrational internal relaxations in the resonance splitting are the nonradiative internal conversion described by Kasha (section 2.3.3.1).

2.4.2.5 Modern Conclusions about Molecular Aggregates

In the past decade, Hestand and Spano revisited the first Exciton Models and could extend them by applying the modern knowledge about molecular aggregates collected in the past hundred years.[19] Their model combines the long-range Coulomb coupling with the short-range Charge Transfer-mediated coupling and the vibronic coupling.

Kasha and McRae based their model on composite molecules that can be considered as aggregated of isolated molecules without orbital overlap, well defined by the Coulomb coupling, J_{Coul}:

$$J_{Coul} \approx \frac{\bar{M}^2}{r_{12}^3}(1 - 3\cos^2\theta) \qquad [\,5\,]$$

Equation [5] gives the strength of the Coulomb coupling, related to Equation [4]. However, the interest of the present work is the π-stacks of chromophores. They have a shorter intermolecular distance, ~3.5 Å, than the composite molecules, where the distance between chromophores is much larger than the size of the molecule. As explained in section 2.1.6, they are affected by the spin-orbit coupling that leads to orbital overlap: HOMO-HOMO and LUMO- LUMO, that assures the dissociation of localized excitations in a molecule into *intermolecular* **charge-transfer**, CT, states, i.e., the movement of the quantum state associated with the exciton from one molecule to another, forming the CT excitons, where the electron and hole reside on different molecules or in other parts of the same molecule.[110,111] The quantum-mechanical interaction mediates the CT process between the molecules, which leads to the short-range interactions: the so-called **superexchange CT- mediated coupling**, J_{CT}.

$$J_{CT} = -2\frac{t_e t_h}{E_{CT} - E_{S_1}} \qquad [\,6\,]$$

Equation [6] gives the strength of the short-range interaction. E_{CT} provides the energy of the CT exciton, while E_{S1} is the energy of the intramolecular Frenkel exciton from the monomer, as seen in Figure 7. The transfer integrals from the electron, t_e, and the hole, t_h, are considered here as the dissociation integrals. Those integrals depend on the orbital overlap and give the sign of the total coupling and the magnitude of the coupling. The orientation and spatial arrangement of the molecules significantly influence these integrals. As a result, the geometry of the molecular system plays a crucial role in determining the effectiveness and directionality of the charge transfer process.[112]

Depending on the sign of the coupling, it will be assigned a J- or H- aggregate character. For long intermolecular distances, the Coulomb coupling is valid for describing the interactions, and the J_{Coul} - sign only changes when trespassing the frontier case of the magic angle. However, for the shorter intermolecular distances typically observed in π-stacked systems, where not only Coulomb coupling is taking place, the J_{CT} - sign changes more often because it depends on sub- Å shifts of the packing structure. Because the superexchange interaction results from orbital overlap between adjacent molecules, 1 and 2, the strength of the interaction decreases exponentially with the interchromophore distance, r_{12}. The Coulomb coupling is not sensitive to those changes. The short-range interaction will show *vibronic spectral features* equal to the features that Kasha´s J- and H- aggregates show after the transition dipole interaction. Therefore, in CT-mediated interaction, if the E_{CT} is higher than the E_{S1}, for the case of $t_e t_h > 0$, this will lead to a J-aggregate-like behavior and H-aggregate-like if $t_e t_h < 0$. Opposite behaviors occur for E_{CT} lower than the E_{S1}. However, the geometry of those CT-mediated aggregates is different from the geometry of Kasha's aggregates.

The consideration of the short-range coupling does not exclude the effect of Coulomb coupling. Both can coexist in π-stacked chromophores if the energy of the CT exciton differs considerably from the Frenkel exciton energy: $|E_{CT} - E_{S1}| >> |t_e|, |t_h|$, the CT state is considered virtual. They form the *total coupling*, Equation [7]:

$$J_{total} = J_{Coul} + J_{CT} \quad [7]$$

that exhibits interferences between them due to their similar magnitude, leading to a new collection of aggregates, such as HH, HJ, JH, and JJ aggregates, that show new photophysical characteristics.

The vibronic coupling depends on the magnitude and sign of the Coulomb coupling. Those differ depending on the aggregation type.[20,33,113]

2.4.3 Mixed electronic states in Organic semiconductors

When two chromophores are near each other, mainly due to stacking, either as a pair in a more extensive π-conjugated system or in a dimer, their excited states interact inter and intramolecularly. Upon absorbing energy and reaching an excited state, these chromophores often transition into *intermediates*, which are temporary states that chromophores transition into following excitation before reaching a stable or final state. These intermediates are commonly characterized as **diabatic states**, energy states with well-defined electronic configurations kept approximately constant during the system's dynamics. Diabatic states are often formulated without explicitly considering the nuclear coordinates because they are typically delocalized over multiple geometric configurations, making it difficult to assign a unique set of nuclear coordinates. Diabatic states serve as a simplified framework for describing excited-state reactions and pathways, while **adiabatic states** account for electronic and nuclear configurations. In this context, the term adiabatic is employed to indicate the applicability of the Born-Oppenheimer approximation so that electronic states can be considered in isolation from nuclear movements. In some cases, the system dynamics lead to **coherent mixing** of these diabatic states. This indicates a dynamic blending of fixed states into an intermediate state, merging characteristics from each contributing state to form a new state with unique electronic or spin properties. The mixing leads to an efficient coupling of states when the adiabatic states have similar energy and geometry.

Relevant diabatic states for the present work are the localized **Frenkel exciton** $|S_1S_0\rangle$, the correlated triplet pair state $|T_1T_1\rangle$, pertinent to the process of **singlet exciton fission** (section 5.2), and **charge transfer** $|CT\rangle$ states. CT states involve electron transfer from the HOMO of the donor to the LUMO of the acceptor, leading to a polarized, charge-

separated configuration. The CT states are similar to *charge-resonance* states in that when identical chromophores are involved, the charge distribution between them is indistinguishable, making it unclear which molecule is the electron donor and which is the acceptor.

There are, however, different degrees of mixing. This can be described as a range of states that change over time, creating various end states or **mixing products**. These evolve as the coherent mixing of states is disturbed by the stabilization of molecular and electronic structures by environmental interactions with solvents or by changes in the electron spin. The end states are a **triplet pair** state $|^{M}(T_1T_1)\rangle$, which may have varying spin multiplicities, M (section 2.1.4); excimers, which are short-lived excited states formed from a combination of $|^{1}(S_1S_0)\rangle$ and $|CT\rangle$ states, referred as Frenkel- CT mixing, **F-CT**, and often serve as trap states, because they can halt or slow down energy transfer processes; and **symmetry-breaking charge transfer** (SB-CT), a condition where the initial balanced charge in the system shifts, breaking the charge-resonance, localizing the cation and anion character on separate chromophores.[10,114]

The F-CT exciton coupling is an essential process to understand the topics discussed in the present study. For example, Chapter 4 considers the intra-intermolecular coherent mixing of those *diabatic* states in periodic one-dimensional (1D) chains of metal phthalocyanines. A linear arrangement of molecules characterizes this interconnected through either covalent bonds or weak interactions such as van der Waals forces. It exhibits two isolated Frenkel exciton states in the lowest energy levels. In the diabatic framework, electronic transitions and vibrational levels 0 and 1 are considered when analyzing the spectral features. Consistent with most practical experiments under low and moderate laser excitation densities, where only two vibrational levels are considered, as higher vibronic levels are not reached, the assumption is that only one Frenkel exciton is excited in the system at any given time. It is also assumed that this exciton coherently mixes with the CT exciton, not with another Frenkel exciton.

Utilizing a Hamiltonian diagonalization method presented by Petelenz in 1979,[115] the eigen energies of each new F-CT energy level are obtained, which will give the shape of the absorption spectrum from the chromophore stacking. This mathematical approach

employs the nearest-neighbor approximation in 1D molecular stacks: the distance between molecular planes in 1D stacks is considerably smaller than in other thin-film configurations, facilitating the calculation of the vibronic overlap factor, s_ν, between the ground state and the vibrational level $\nu = 0$ and $\nu = 1$ of the molecule's first excited state in the lattice position n. The square of the overlap factor is the Franck-Condon factor, dependent on the exciton-phonon constant, g, a parameter that quantifies the interaction between electronic excitations, excitons, and lattice vibrations, phonons: $F_{0\nu} = |s_\nu|^2 = \frac{g^{2\nu} e^{-g^2}}{\nu!}$. The formulation assumes a strong exciton-phonon coupling, therefore $g \sim 1$. Such a strong coupling regime simplifies or neglects certain complexities related to the 1D lattice configurations. Precisely, scenarios where the Frenkel exciton and an intramolecular optical phonon are situated at different lattice sites are not considered. This model considers neither potential hopping between CT states nor excited CT states. This model assumes that additional molecular states in the system possess no transition moment, meaning that only the Frenkel and CT states exhibit absorption intensity.

The system total Hamiltonian is a sum of all of the following contributions in the momentum space, k:

$$\widehat{\mathbf{H}} = \sum_{k} \underbrace{\widehat{H}_k^F}_{\substack{\text{Frenkel} \\ \text{exciton}}} + \underbrace{\widehat{H}_k^{FF}}_{\substack{\text{Frenkel exciton} \\ \text{hopping}}} + \underbrace{\widehat{H}_k^{CT}}_{\substack{\text{nearest}-\text{neighbor} \\ \text{CT exciton}}} + \underbrace{\widehat{H}_k^{F-CT}}_{\substack{\text{Frenkel}-\text{CT} \\ \text{exciton}}} \qquad [8]$$

Where $\widehat{H}_k^F \sim \Delta_F^\nu$ represent the intramolecular Frenkel exciton created upon photon absorption on the molecule $\mu = 1$, depending on the energy at the vibrational level ν. The Frenkel- exciton hopping to neighboring sites from the 1D periodic molecular chain is proportional to the transfer probability between vibrational levels ν and ν': $\widehat{H}_k^{FF} \sim 2M s_\nu s_{\nu'} \cos k$, where M is the nearest-neighbor exciton transfer integral. A localized CT exciton constituted by a hole located at the lattice site n, and an electron located at n + 1 or n - 1, has the ground state energy $\widehat{H}_k^{CT} \sim \Delta_{CT}$. In the k-space, the

intermolecular CT exciton that it is formed due to a reversible quantum-mechanical-tunnel transfer[2] of the Frenkel-electron, or hole, from the excited molecule in n to its nearest neighbor is considered the diabatic mixing F-CT state. The Hamiltonian, $\widehat{H}_k^{F-CT} \sim t_k s_\nu$ is therefore dependent on the transfer integrals, t_e and t_h, as well as on the vibronic overlap factor, s_ν, and the creation and annihilation operators also presents in pure Frenkel and pure CT states, that create and annihilate the corresponding Frenkel and CT excitons.

The total Hamiltonian, $\widehat{\mathbf{H}}$, is diagonalized to give as a result the eigen energies and states of the F-CT mixing, $\mathbf{E}_{\nu\mu}^{\mathrm{F-CT}} = \hbar\omega_{\nu\mu}$, that are dependent on the above mentioned pure-states energies and transfer factors. With Frenkel terms as: $\mathrm{F}_k^{\nu\nu'} = \Delta_{\mathrm{F}}^{\nu}\delta_{\nu\nu'} + 2Ms_\nu s_{\nu'} cos\, k$ as given by:

$$\mathbf{E}_{\nu\mu}^{\mathrm{F-CT}} = \frac{1}{2}\left(\mathrm{F}_{\mathrm{k}}^{\nu\nu'} + \Delta_{\mathrm{CT}} \pm \sqrt{(\mathrm{F}_{\mathrm{k}}^{\nu\nu'} - \Delta_{\mathrm{CT}})^2 + 8(\mathrm{s}_\nu \mathrm{t}_{\mathrm{k}})^2}\right) \qquad [9]$$

From this Equation [9], four F-CT mixed states are derived, comparable to the peaks and shoulders observed in the experimentally obtained steady-state absorption spectra. This is demonstrated in Chapter 4 for the CuPc molecule.[40,116]

[2] Tunnel transfer is a movement of an electron or hole from the excited molecule at lattice site n to its nearest neighbor. The electron, or hole, should cross a potential barrier, which is impossible under classical physics due to insufficient energy to surpass the barrier, yet made possible by the probabilistic nature of quantum mechanics.

Chapter 3

Experimental Methods

A scientist in her laboratory is not only a technician: she is also a child placed before natural phenomena, which impresses her like a fairy tale.

M. Curie[47]

3.1 Spectroscopy to Understand Chromophores

The 1999 Nobel Prize in Chemistry was awarded to Ahmed Zewail for pioneering ultrafast *lasers* to investigate chemical reactions on the *femtosecond timescale*.[117] This same timescale is relevant to how organic chromophores, the light-absorbing centers in molecules (section 2.1.3), respond to light excitation in the UV-visible range. The response of these chromophores has significant implications for applications such as solar energy harvesting and biological imaging. Traditional studies, like steady-state absorption and fluorescence, often focus on ground states and cannot image excited states in absorption spectra. *Ultrafast Transient Absorption Spectroscopy* (TAS), and specifically femtosecond transient absorption spectroscopy (fs-TAS), addresses this gap by quantifying transitions from excited states to higher energy levels. By monitoring the change in absorbance as a function of time after photoexcitation - controlled by the delay between the pump and probe pulses, fs-TAS provides comprehensive insights into both the spectral characteristics and temporal kinetics of excited states. TAS accommodates challenges like high concentrations of excited states and background absorption from ground states while operating across relevant wavelengths. The dynamics of transitions between different states and subsequent *kinetics* depend heavily on highly short-lived intermediate states ranging from vibrational redistributions (section 2.3.1) to electronic transitions on *timescales from femtoseconds* to nanoseconds (section 2.3.2). Information gleaned from this non-linear optical technique proves indispensable for optimizing chromophore performance in real-world applications. In photovoltaic devices, a nuanced understanding of light energy transfer by chromophores informs the design of more efficient energy conversion systems. In the context of biological imaging, the identification of precise relaxation pathways of fluorescent chromophores contributes to tailoring properties for enhanced sensitivity or selectivity.[118–121]

3.2 Steady-state Processes

Determining the steady-state absorption and fluorescence spectra is fundamental for understanding the properties of a chromophore. Those spectra are positive functions of the intensity of absorption or fluorescence depending on wavelengths. Absorption spectra provide insights into electronic transitions between ground and excited states, delineating the energy gaps and the probability of such transitions occurring. Fluorescence spectra, however, detail radiative transitions from excited states back to ground states. They are typically characterized by parameters such as Stokes shift with respect to the absorption energies.

3.2.1 Steady-state Absorption

The Steady-state absorption measurements in this thesis were done using a Perkin Elmer Lambda900 spectrophotometer. Inside the device, a light source generates a beam that passes through a monochromator, isolating a specific wavelength from the broad spectrum of emitted light by employing optical components such as gratings and prisms to diffract and filter the incoming light beam. A Deuterium flash lamp, with a spectral range of 190 nm to 400 nm, and a Tungsten-halogen lamp, from 350 nm to 2500 nm, serve as the light source. The isolated light beam travels through the sample holder, interacting with the sample. The light absorbed by the sample is quantified by comparing the light intensity before and after it passes through the sample. A photomultiplier tube and Peltier-controlled PbS detectors capture the transmitted light and convert it into an electrical signal for precise temperature regulation. This signal is then processed and analyzed by the software UV WinLab™, transforming the raw data into an absorbance, transmittance, or reflectance spectrum.[122]

Temperature-dependent absorption measurements for collaboration publications[123] were done with a home-built setup. The light source was from a Deuterium Halogen lamp (OceanOptics) connected to an optical fiber with 600 µm diameter to a cryostat holder from a sample-in-vacuum cryostat (Optistat CF-V, Oxford) reaching up to 500 K. The transmitted light after the sample was collected by another optical fiber connected to a USB400 Miniature CCD-Array spectrometer, all devices from Ocean Optics. A spectrometer operates by capturing light through a fiber-optic input, which then passes

through an entrance slit into a collimating lens. This collimated light, which consists of parallel rays minimally divergent, allowing the light to travel in a unified direction over a significant distance, is dispersed by a diffraction grating into its component wavelengths and focused onto a Charge-Coupled Device (CCD) array. The CCD array detects light intensity at different wavelengths, and the resulting data is transferred to a computer via a USB interface for real-time analysis.[124]

In spectroscopy, transmittance, T, and absorbance, A, are related through $A = -\log_{10}(T)$, where transmittance is defined as the ratio of the intensity of light passing through the sample, I, to the intensity of the incident light, I_0, $T = I/I_0$. I_0 is obtained in the case of a liquid sample measuring the transmitted light through the cuvette containing the solvent and in the case of a thin film with the substrate. The negative logarithm of this ratio yields the absorbance, a unitless quantity. This logarithmic relation signifies that a high transmittance corresponds to a low absorbance and vice versa. Essentially, absorbance quantifies how much light a sample absorbs, whereas transmittance quantifies how much light passes through it.[125,126]

3.2.2 Steady-state Fluorescence

The fluorescence measurements done for Chapter 5 were done using a HORIBA Jobin-Yvon Fluorolog 3–22 Tau-3. This device employs a photomultiplier tube as its detector to capture and amplify the weak fluorescence signals emanating from samples. Light from an excitation source passes through a monochromator to isolate a specific wavelength and then excites the sample in a cuvette or sample holder. The emitted fluorescence from the sample is collected and passed through a second monochromator to isolate the emission wavelength of interest further. The PMT captures this isolated fluorescence signal and converts it into an electrical current, amplified for enhanced sensitivity. This amplified signal is fed into FluorEssence software (version 3.9.0.1; Origin version 8.6001) for data acquisition, analysis, and display.

Recording steady-state absorbance and emission spectra is necessary before transient absorption experiments. Absorption steady-state features identify ground-state features and provide effective *excitation wavelengths*, as significant sample absorption

at these wavelengths yields proper signals with varying TA intensities based on the excitation wavelength. Insufficient or excessive absorption levels compromise transient spectral data quality by saturating the sample or yielding an insufficient signal-to-noise ratio. Understanding the emission region is also crucial to avoiding the incorrect assignment of negative features to ground-state bleach instead of stimulated emission. Thus, knowledge of steady-state spectra is fundamental for adjusting the parameters and interpreting complex transient studies (Section 3.3.3).[127]

3.3 Transient Absorption Spectroscopy Setup

The underlying principle of TAS is the measurement of absorption spectra for excited states using an appropriately designed experimental setup, as shown in the schematic from Figure 8. A typical TAS instrument employs a high-intensity pump pulse to generate the transient species by exciting the system from its ground state to an excited state. Post-excitation, this pump pulse light encounters a beam block, ensuring its exclusion from further interaction within the setup. Various transient species may be present depending on the time after photoexcitation. This is the delay time, Δt, between the pump and probe pulse. The *probe* pulse is a white light pulse, lower in intensity than the *pump*, that traverses through the sample and passes through a diffraction grating before reaching the photodetector. It monitors the change in absorption as a function of the time delay. The pump pulse will not excite every molecule in the system but around 10^{-1} to 10^{1} %. Therefore, the resulting spectrum is obtained from the difference in absorption at different delay times:

$$\Delta A(t) = A_{excited}(t) - A_{ground}(t), .^{128,129}$$

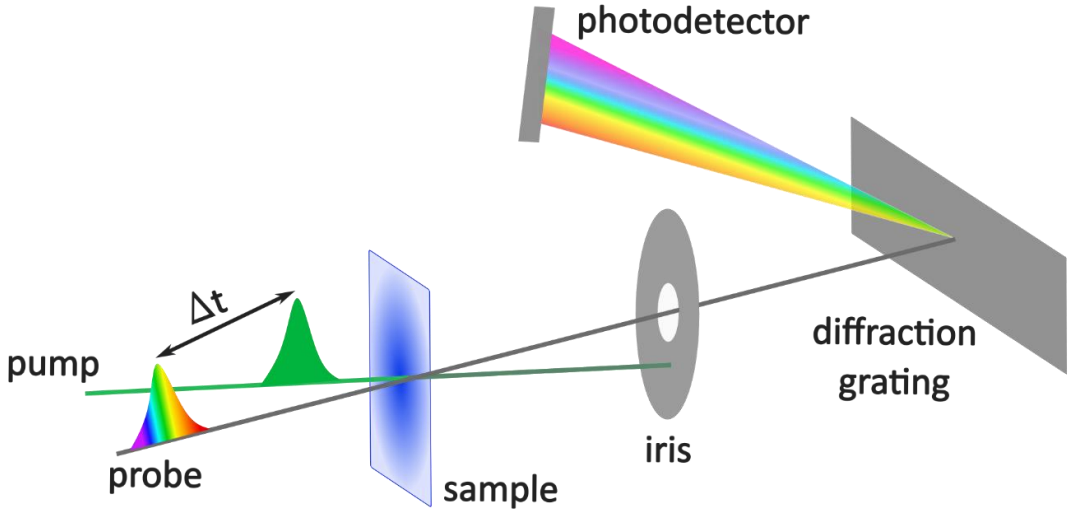

Figure 8: Schematic of a Transient Absorption spectroscopy pump-probe Setup: In this illustration, the pump pulse, represented in green and signifying a specific wavelength, intersects with the sample, depicted in blue to exemplify a typical sample used in the present work. This intersection occurs at the same spatial position where the probe, a white light continuum, also intersects the sample. After photoexcitation, the pump beam is obstructed by an iris, whereas the probe beam proceeds to pass through a

diffraction grating before reaching the photodetector. The delay time, Δt, represents the temporal difference between the pump and probe pulses.

The probe and pump beams originate from the same *laser* system light source. The following sections will discuss the details of this laser system. The complete setup is described by the schematic presented in Figure 9.

Initially, a laser (Pharos, Light Conversion) emits a pulsed beam at 1030 nm. This beam is bifurcated into two separate pathways. Approximately **20%** of the original beam is allocated for the **probe** light, represented by red lines. This light is guided through a series of mirrors to a delay stage module, where a motorized delay stage (black box of Figure 9) modulates the path length. It will induce temporal delays ranging from 200 fs to ~8 ns between the probe and the pump pulses. The probe light is then focused through an array of lenses and white-light generation media of the *motorized stage* to generate a continuum, which is adjusted to get the desired spectral range—UV for ultraviolet, NIR for near-infrared, and Vis for visible—indicated by color-coded squares. This continuum subsequently interacts with the sample in the TAS module.

The remaining **80%** of the original 1030 nm beam traverses an optical parametric amplifier (OPA), Orpheus. More details in Figure 13 (Orpheus-F, Light Conversion). The OPA yields two output signals: the idler and the signal, the use of which depends on the desired **pump** wavelength. The fundamental beam transitions to dark green upon passing through a second harmonic generator (SHG) to achieve frequency doubling. According to the OPA specifications, the *signal* spans wavelengths from 620 nm to 1010 nm and the *idler* from 1050 nm to 2500 nm. This pump beam is also routed through a series of mirrors and irises and is directed toward the TAS module. Here, it passes through a chopper and a density filter, allowing precise control over the excitation density.

The pump and probe beams intersect the *thin film sample* from opposite directions to mitigate spectral contamination from the pump signal. In the case of the *solution sample*, the pump beam comes from the same direction as the probe (as in Figure 8) to ensure that the set delay time between both is the actual delay of the pump hitting the molecules, avoiding the effect of the sample thickness (a 1-2 mm cuvette). Finally, the

ΔA signal, represented by blue lines, undergoes attenuation through a second-density filter to prevent saturation of the detector. It then enters the detection stage, where a series of mirrors focus the signal into a fiber connected to the spectrograph.

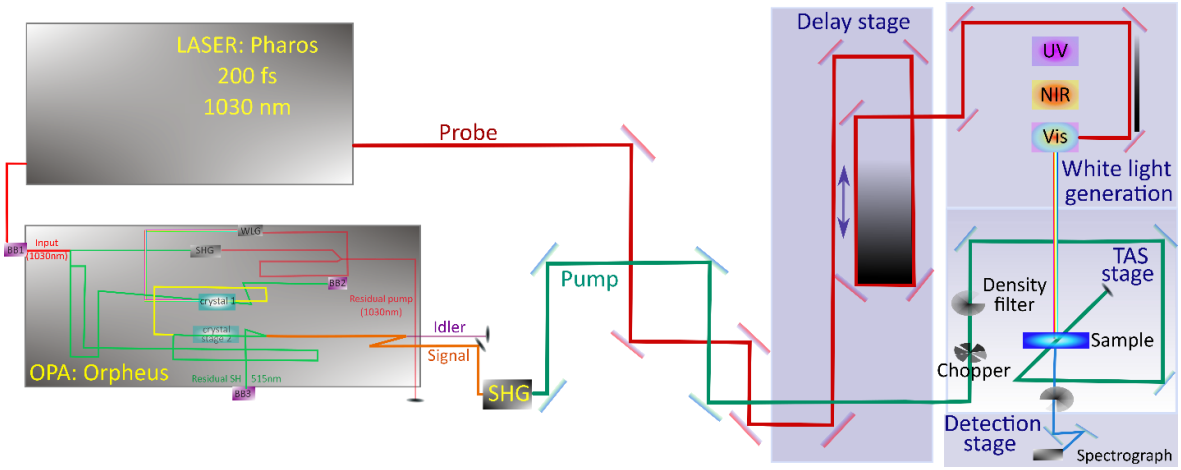

Figure 9: Transient absorption spectroscopy (TAS) laboratory set-up. The arrangement proceeds from left to right.

3.3.1 Light Source: Laser

In 1958, the same year it was reported that the absorption spectra of stacked chromophores differed from those in a liquid solution, thereby revealing the impact of aggregation on photophysical responses to light excitation (section 2.4.2.1), Charles Townes and Arthur Schawlow introduced the world a technique that would revolutionize not just the field of photochemistry but also those of communications, medicine, and engineering. Utilizing the photoelectric effect, which Einstein had postulated 50 years earlier, they presented the technology known as LASER, an acronym for Light Amplification by Stimulated Emission of Radiation.

A laser is a powerful and precise light source that amplifies and produces a highly directional, intense beam or train of intense pulses characterized by their remarkable spectral purity in frequency or wavelength. This is achieved through the synergistic interplay of *optical pumping* to excite the medium, *mode-locking* ultrafast pulse generation, *pulse stretching* through the grating, *pulse amplification* via stimulated emission of the gain medium, and *pulse compression*. All of this is done before dividing the laser beam into the mentioned two sub-beams, the **probe** beam, guided to the

sample, and the wavelength-tuned **pump** beam via optical parametric amplification. The pulsed nature of lasers enables capturing dynamic and ultrafast processes by temporally resolving phenomena on femtosecond to picosecond scales. The color purity allows for selective excitation in chromophore systems, facilitating precise control for studying molecular interactions and dynamics.

The laser used for the experiments in this work is the model PHAROS from Light Conversion Ltd, which has a gain medium featuring potassium gadolinium tungstate as the host crystal and ytterbium ions (Yb^{3+}) as the active dopant (Yb:KGW).

The inception of the laser pulse occurs within a laser cavity facilitated by a **mode-locked** oscillator. The *laser cavity* generally consists of a gain medium and a complex set of mirrors, prisms, and grating-diffraction devices that form a resonant optical loop enabling the **chirp pulse amplification** technique.

First, an external light source emits photons via optical pumping that the active medium absorbs. This photon absorption prepares the system for subsequent lasing action by creating a larger population of electrons of the dopant ions in excited states than electrons in ground energy states, known as *population inversion*.

Within the laser cavity, three fundamental radiation processes associated with the interaction of light with matter occur: absorption, spontaneous emission, and stimulated emission. In this context, the term emission refers to fluorescence, a term more commonly used in a molecular setting. However, these processes within the laser cavity operate at the atomic level. Following the enlightening explanation by Silfvast, absorption is the process wherein energy stimulates an electron, leading to its excitation. Thus, this phenomenon can be referred to as *stimulated absorption*. The **Principle of Detailed Balance** stipulates that when a system is in equilibrium, the total number of particles leaving a given quantum state per unit of time is identical to the total number of particles arriving at that same quantum state per unit of time. This principle explains that if a photon can stimulate the electron to change from a lower energy state, L, to a higher energy state, U, when absorbing it, the inverse process should also occur: a photon can stimulate the electron in the same high energy state to undergo relaxation to a lower energy state. This is the **stimulated emission** (SE), which

was introduced by Einstein in 1917. As seen in Figure 10, the photon disappears in the case of absorption, and its energy goes to the material that absorbed it. For stimulated emission, an extra photon has to be emitted to conserve energy. The SE process is needed to keep the energy levels of the two states in thermal equilibrium, which is related to the Planck law for radiation.[48] The emitted additional photon not only has exactly the same energy (ergo frequency: $\Delta E_{UL} = h\nu_{UL}$) as the energy of the incident photon but it is also emitted in exactly the same direction, being in phase with the incident photon, to conserve the momentum, which is crucial for the generation of the laser beam.

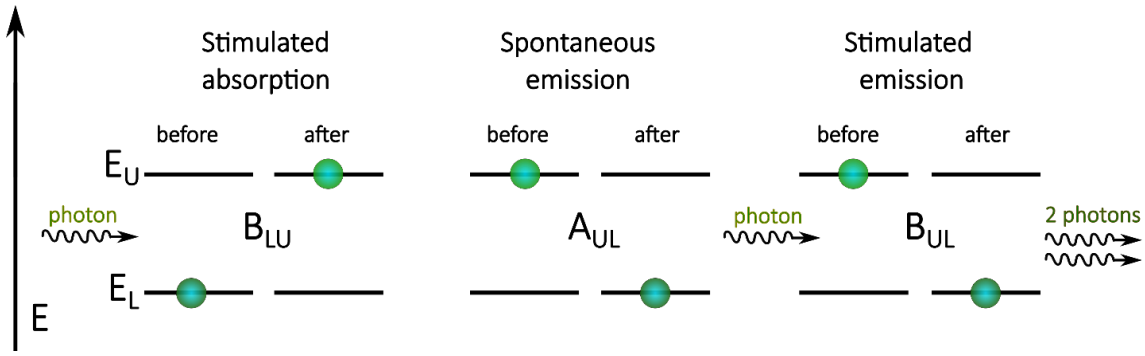

Figure 10: The three fundamental radiation processes in a laser cavity, in a two-level system of atoms with a low energy state, E_L, to an upper energy state, E_U. Einstein Coefficients for each transition are given: stimulated absorption of a photon; spontaneous emission of a photon that, due to the Principle of Detailed Balance, produces the de-excitation of other excited atoms; stimulated emission, emitting two photons with the same phase, that make the coherent beam of light. (Adapted from Silfvast Chapter 6.4 [130])

The *light generation* process then commences with a **population inversion**, during which photons from optical pumping are absorbed, thereby exciting the atoms, leaving more atoms in the excited state than in the ground state. Some atoms begin to relax, undergoing spontaneous emission that yields photons with a particular frequency and phase. These photons, referred to as *seed photons*, interact with some of the already excited atoms, forcing them into a state of de-excitation: SE. This produces two photons in phase with the seed photon, generating a coherent light beam.

The condition for population inversion and, therefore, SE are given by the **Einstein coefficients**, which allow for a quantitative understanding of the rates at which the principal radiation processes occur in a system of atoms or molecules interacting with electromagnetic radiation, considering a two-level system of atoms as depicted in Figure 10. Let A_{UL} denote the Einstein coefficient for spontaneous emission probability, B_{LU} for absorption, and B_{UL} stimulated emission. They are related as $A_{UL} \sim \nu^3 B_{UL}$ and $g_L B_{UL} = g_U B_{LU}$. Where ν is the photon frequency, and g_L and g_U are the statistical weights of the lower and upper energy states, respectively. The rate equations for the population densities N_L and N_U of the lower and upper energy states (E_L and E_U, respectively, in Figure 10) can be formulated as follows:

$$dN_L/dt = -B_{LU}N_L\,\rho(\nu) + A_{UL}N_U + B_{UL}N_U\,\rho(\nu) \qquad [10]$$

$$dN_U/dt = B_{LU}N_L\rho(\nu) - A_{UL}N_U - B_{UL}N_U\,\rho(\nu) \qquad [11]$$

Where $\rho(\nu)$ is the spectral energy density of the radiation field. SE becomes the dominant process when the medium is in a state of population inversion: $N_U > (g_U/g_L)N_L$. The term $B_{UL}N_U\,\rho(\nu)$ dominates the equations in this state. Considering Planck´s law for cavity radiation, where k is the Boltzmann constant, and T is the temperature of the cavity:

$$\frac{B_{UL}\rho(\nu)}{A_{UL}} = \frac{1}{e^{\frac{h\nu_{UL}}{kT}} - 1} \rightarrow \frac{N_U}{N_L} = \frac{1}{e^{\frac{h\nu_{UL}}{kT}} + 1} \qquad [12]$$

Stimulated emission dominates only when the temperatures result in $kT \geq h\nu_{UL}$, which occurs in lasers cavities. However, although the explanation of population inversion using Einstein coefficients has been given for a two-energy-level system, it is essential to note that population inversion cannot occur in a two-level system. This is because, considering the Fermi-Dirac distribution for electrons, the ratio N_U/N_L will not satisfy the condition for population inversion, regardless of whether the temperature is zero or infinite. In the case of a three-level system, it is challenging to reach high population inversion. A very strong pump is needed to create population inversion, as

most electrons are in the E_L state. But in a four-level system, achieving population inversion is easy and efficient, as Dr. Hai Wang explained in his notes for the Optics course at the MPIP. [130,131]

Once the gain medium is excited, it is time to *generate pulses*. The generation of ultrafast laser pulses occurs via **mode-locking**. A *cavity mode* is a time-independent standing wave that arises from the interference phenomena taking place when light interacts with two parallel reflective surfaces, such as two mirrors separated by a distance d, in the case of a simplified laser, like the Fabry-Perot resonator. Laser modes are, therefore, wavelike properties of the beam. They are the specific solutions to the wave equation. This partial differential equation governs wave propagation under the boundary conditions imposed by the cavity mirrors, such as zero electric fields at the mirror surface, serving to enhance electromagnetic waves within the cavity, and a periodic field in the rest of the cavity. Each mode corresponds to a distinct longitudinal or transverse electromagnetic radiation field configuration. Specifically, the longitudinal modes are used in the mode-locking technique. They have different frequencies, but they become synchronized by locking, i.e., fixing the phases between different modes. Constructive interference occurs at regular time intervals, producing a *train* of ultrashort coherent, phase-locked pulses.

There are several ways to synchronize the phases of different longitudinal modes. In *passive mode-locking* techniques, saturable absorbers are commonly used for generating pulses with periods in the sub-ps range, as observed in lasers like Pharos. Alternatively, nonlinear optical elements, such as Kerr media, play a crucial role. In these materials, the refractive index changes proportionally to the intensity of the incident light. This property allows for generating pulse periods of less than 10 fs by introducing intensity-dependent loss within the laser cavity. In active mode-locking schemes, external modulators like acousto-optic modulators are employed to impose a periodic modulation on the intra-cavity field, effectively gating the laser to generate pulses at specific intervals of about 1 to 10 ps. These modulators operate by inducing a periodic change in the refractive index of the medium, controlled by an external radio frequency signal.[132,133]

The frequency at which these pulses recur, termed the **repetition rate**, RR, is dictated by the dimensions of the laser cavity and in this case: $\Delta f = c/2d = 80$ MHz, where c is the speed of light. The gain medium gives the bandwidth of the laser; in the case of Pharos, Yb:KGW is about 8.2 nm, centered at 1030 nm,[134] which corresponds to a $\Delta\nu = c\,\Delta\lambda/\lambda^2 \sim c \cdot 8.2\text{ nm}/(1030\text{ nm})^2 = 2.3 \cdot 10^6$ MHz. This gives a number of modes $n = \Delta\nu/\Delta f$ of around $2.3 \cdot 10^6$ modes.

Broad bandwidth is characteristic of ultrafast pulsed lasers due to the Heisenberg **Uncertainty Principle**, which states that it is impossible to simultaneously know specific pairs of complementary properties of a system with perfect precision.[55] In the context of light pulses, this is explained by the **time-bandwidth product** (TBP): the product of the pulse duration, Δt, and the bandwidth, $\Delta\nu$. For a Gaussian-shaped pulse, the minimum TBP is: $TBP_{\text{Gaussian pulse}} = \Delta t \cdot \Delta\nu \sim 0.44$. The TBP indicates how closely a pulse approaches its transform limit, the minimum pulse duration constrained by its spectral width. This can be considered a measure of pulse quality in ultrafast optics.

Bandwidth-limited pulses possess the lowest possible TBP, typically slightly below 0.5, whereas chirped pulses exhibit higher values. The Pharos system in this work is rated at Δt = 223 fs. Thus, according to the Uncertainty Principle, a small pulse duration must be accompanied by a large bandwidth, in the Pharos case: $\Delta\nu \sim 2.3 \cdot 10^6$ MHz, as calculated above. With this, the TBP results in **TBP_{Pharos} = 0.52**. This is typical of a chirped pulse and close to the theoretical minimum probing, where the pulse is nearly transform-limited and thus optimal for ultrafast applications.[135]

In the mode-locking regime, a train of optical pulses is generated, each characterized by a specific spectral bandwidth and peak intensity, measured in units of power per unit area (W/cm²). The peak intensity corresponds to the maximum Gaussian distribution describing the pulse profile. However, this intensity is insufficient for executing transient absorption spectroscopy measurements. Therefore, increasing the output intensity via pulse amplification is necessary. Direct amplification of such pulses risks damaging the gain medium and can cause other nonlinearity-derived problems, such as self-focusing. These challenges were addressed by the groundbreaking **Chirped Pulse Amplification** (CPA) technique developed by Donna Strickland and Gerard Mourou in

1985. In the fiber-based Nd:YAG laser that they present, initially, the pulse undergoes frequency widening, referred to as frequency chirping, through self-phase modulation. Subsequently, the chirped pulse is temporally stretched to circumvent gain medium degradation, thereby reducing its peak intensity at any given time point via group velocity dispersion. This enables safe amplification. Following amplification, the pulse is temporally compressed using a double grating compressor, completing the CPA process.

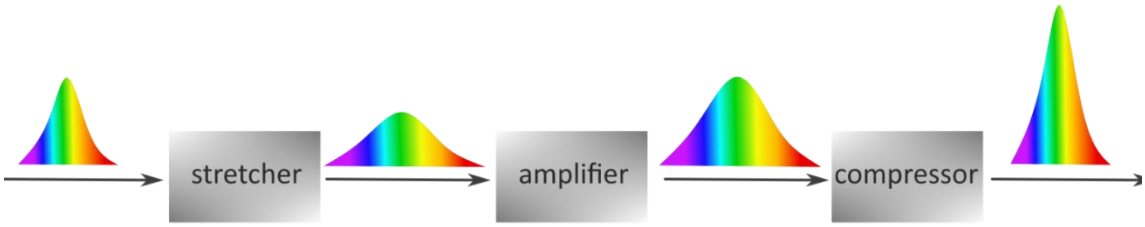

Figure 11: Chirped Pulse Amplification (CPA) concept.

In general, *self-phase modulation* is instigated through the interplay between a time-dependent laser pulse and a nonlinear change in the refractive index of an optical medium. This change is dependent on the light intensity, known as the Kerr medium. A nonlinear medium is one in which the output is not proportionally related to the input. This technique expands the pulse's bandwidth as it traverses the nonlinear medium. The alteration in refractive index is mathematically described by the equation $n(\nu) = n_0(\nu) + n_2(\nu)\, I(\nu)$, where n_0 is the frequency-dependent index of refraction, and n_2 is the intensity-dependent index. As the pulse moves through this nonlinear medium, it experiences self-phase modulation, thereby *widening its frequency spectrum*. This broadening arises because the rising part of the pulse experiences an increase in the refractive index. This results in a deceleration of the beam's velocity. The delayed arrival of this part of the electromagnetic wave at the crystal's exit effectively reduces its frequency. Conversely, the trailing portion of the pulse encounters a decrease in the refractive index, which accelerates its passage through the crystal and correspondingly leads to an elevation in frequency. In essence, the blue shift occurs on the trailing edge, opposite to the red shift on the leading edge. The net effect is that more waves arrive within the same time frame, effectively augmenting the pulse's frequency spectrum.

This widening of the spectrum, induced by the variations in the refractive index during the pulse propagation, is commonly referred to as pulse chirping.

Group velocity dispersion (GVD) is a method employed to modulate the temporal duration of mode-locked optical pulses. In a dispersive medium, where the index of refraction varies as a function of frequency, the peak of the pulse travels at a unique velocity known as the group velocity. This is distinct from the phase velocities of the individual waves within the pulse: $v_g = \frac{d\omega}{dk}$, ω is the angular frequency of the wave, and k is the wave vector, that describes the spatial variation of the wave, $k = 2\pi/\lambda$. When two light pulses travel through a medium characterized by substantial GVD, they can be considered separate wave packets, each with unique frequencies and corresponding group velocities. The GVD of the medium is defined by: $ß_g = \frac{d^2\omega}{dk^2}$. Due to the frequency-dependent nature of this dispersion, an optical pulse may either undergo temporal compression or stretching as it moves through the medium. Positive GVD implies that the group velocity decreases as the pulse frequency increases or increases equivalently as its wavelength decreases. In this scenario, the pulse components with longer wavelengths and red components will travel faster than those with shorter wavelengths and blue components. This results in a temporal elongation of the pulse, also known as pulse chirping.[130,136]

In laser systems, diffraction gratings are customarily employed to construct both the stretcher and the compressor components. In the stretcher, the separation distance between the grating and the lens is intentionally configured to be less than the lens's focal length. This specific arrangement results in a negative effective grating separation, leading to the generation of typical dispersion characteristics: the refractive index increases as the wavelength of light decreases, resulting in higher-frequency components of a light pulse traveling faster than the lower-frequency components.

On the other hand, the compressor is predominantly assembled utilizing a Treacy grating pair, in which diffraction gratings are set in a manner that causes higher frequency components of a light pulse to travel more slowly than the lower frequency components, producing an anomalous dispersion: the refractive index decreases as the

wavelength of light decreases. Implementing the Treacy grating pair in the compressor minimizes the introduction of undesirable nonlinear optical phenomena and significantly mitigates the risk of optical damage to the components. The stretcher and the compressor are typically engineered to operate in a double-pass geometric configuration. A planar mirror is incorporated to retroreflect the dispersed optical rays following their initial traversal through the grating pair, guiding them back through the original optical system. This process effectively reconverges the spatially segregated optical frequencies, initially dispersed by a single pass through the grating pair, back into a unified, overlapped beam, as seen in Figure 12.

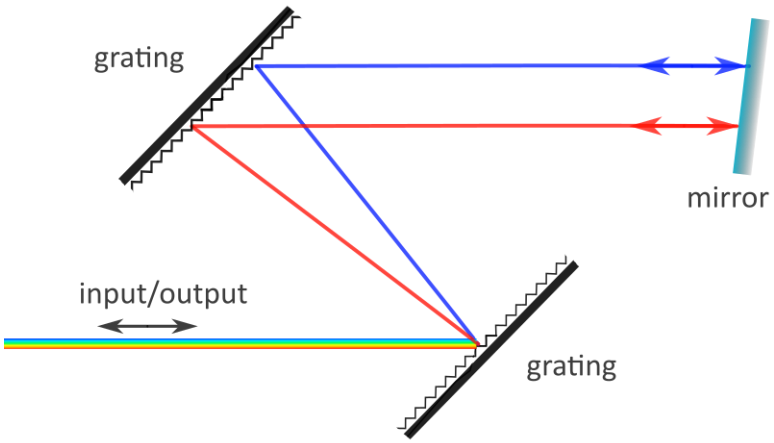

Figure 12: Geometry of a double-pass grating pair for pulse compression. The redirecting mirror can be slightly angled in the vertical plane, perpendicular to the direction in which the light spectrum is dispersed. This angling effectively segregates the incoming and outgoing light beams. (Adapted from Weiner Chapter 8 [137])

After stretching, the elongated pulse is then passed through an amplifier to significantly elevate its energy via population inversion and subsequent stimulated emission process. After that, the pulse is subjected to compression to restore its original temporal duration. This final act of recompression augments the peak intensity to extremely high levels, providing enough laser power for the experiment.[137]

3.3.2 Optical Parametric Amplifier as Pump Beam Source

When a pulsed laser beam at a fixed wavelength of 1030 nm enters the Optical Parametric Amplifier (OPA) Orpheus-F, it interacts with numerous nonlinear media,

such as a beta barium borate (BBO), that exhibits second-order nonlinearity. This property supports optical phenomena governed by the material's second-order susceptibility, $\chi^{(2)}$, in response to an applied electric field. This crystal lacks inversion symmetry, a requisite for this behavior, as centrosymmetric materials possess zero susceptibility for such phenomena. The interaction triggers a process of energy transfer that leads to the amplification of a variable frequency signal pulse ω_S, as well as the formation of an idler pulse ω_I.

First, the initial fundamental pulse from the laser source is divided into a high-intensity pulse for pumping the OPA and a lower-intensity pulse for generating a broadband seed signal. The latter is generated using a white light generation (WLG) process in a sapphire disc, third-order nonlinear medium, $\chi^{(3)}$. The high-intensity pump pulse and the broadband seed pulse are then focused onto the OPA crystal, crystal 1 in Figure 13.

Inside the crystal, electrons are excited from their ground state to higher energy levels by the pump frequency ω_P. When these excited molecules revert to their ground state, they emit two new photons with frequencies ω_S and ω_I. The signal pulse ω_S gains energy from the pump pulse ω_P, leading to its amplification. Consequently, at the output of the OPA, one finds three distinct beams: an amplified signal beam, covering the range of 620 nm to 1010 nm, a newly formed idler beam from 1050 nm to 2500 nm, and a residual fundamental beam, still at 1030 nm.

The efficiency of this energy transfer and the resulting amplification are governed by the conditions of energy conservation: $\omega_P = \omega_S + \omega_I$, and the momentum conservation via wave-vector phase matching: $\overrightarrow{k_P} = \overrightarrow{k_S} + \overrightarrow{k_I}$. The desired signal frequency ω_S can be tuned by adjusting the angle between the interacting wave vectors and the optical axis of the OPA crystal, effectively changing the ratio $\frac{\overrightarrow{k_S}}{\overrightarrow{k_I}}$, and consequently the color of the generated light.

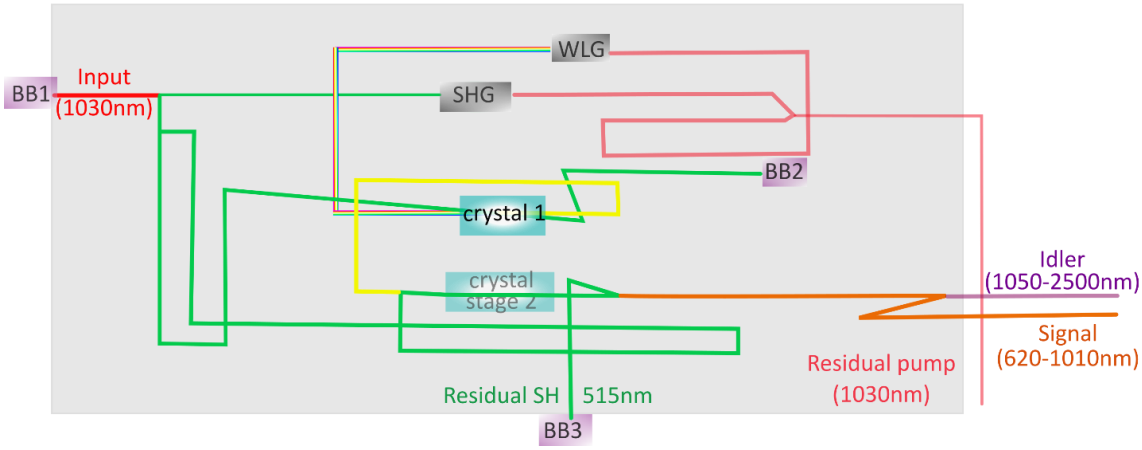

Figure 13: Schematic of the Optical Parametric Amplifier Orpheus-F: The light beam progresses from left to right. An input beam originating from the laser (see Figure 9) with a wavelength of 1030 nm traverses a Second Harmonic Generator (SHG) followed by a White Light Continuum Generator (WLG). Both beams converge at the first amplification stage, denoted as Crystal 1. After this, a second amplification stage, called Crystal Stage 2, generates two output signals: the signal beam, with a wavelength range between 620 nm and 1010 nm, and the idler, ranging from 1050 nm to 2500 nm.

To complete the range of visible light and to generate wavelengths below 620 nm, which is the lower limit for Orpheus-F, a **Second Harmonic Generation** (SHG) stage is used to perform up-conversion on the pump beam, effectively halving its wavelength and thereby doubling its frequency, 2ω, referred to as second harmonic. This process lies in the interaction of the pump beam with a nonlinear crystal. Like the one in an OPA, this crystal possesses specific properties that allow it to interact with the incoming light in a way that fundamentally changes its characteristics. When the pump beam of a specific wavelength enters this nonlinear medium, two photons from the beam combine to create a new photon with twice the energy, or equivalently, half the wavelength, filling in the gaps that the OPA could not cover. Typically, the phase mismatch Δk between the fundamental and second harmonic waves should be minimized: $\overrightarrow{\Delta k} = 2\,\overrightarrow{k_\omega} - \overrightarrow{k_{2\omega}}$. To achieve high conversion efficiency, the crystal orientation or temperature may be adjusted for optimal phase matching conditions.[130,138]

3.3.3 Transient Absorption Module

As explained in Figure 9, the two light beams, probe, and pump, are directed through a set of mirrors, with the aid of irises to align the beams, across the optical table towards the transient absorption spectroscopy setup by Ultrafast Systems Ltd., branded as Helios. The probe beam is routed into the delay stage, containing a retroreflector, sending the beam back along a horizontally parallel path, thereby modulating the optical path length of the 1030 nm beam traverses. This results in a **sequence of delays** between the pump and probe beams, which consequently yield temporally resolved spectra. By scrutinizing these spectra, various time-dependent processes can be studied. The Helios system accommodates delay times ranging from **200 fs to 8 ns**.

After the delay stage, the probe pulsed beam at 1030 nm (**probe**) proceeds to the white light generation module. Three different non-linear mirrors are utilized to create white light continua in various spectral ranges: YAG for NIR, calcium fluoride for UV, and sapphire for VIS spectrum. A motor-controlled lens routes the probe beam to the appropriate mirror. Then, the white continuum is focused on the sample located in the transient absorption module.

The **pump**-pulsed beam, which is significantly more intense than the probe, is guided directly to the transient absorption module once a desired wavelength has been selected via the OPA. Upon entering this module, the beam passes a **chopper** rotating at 500 Hz before being focused onto the sample. The chopper enables the TAS measurement technique, wherein the sample's response can be measured with and without the pump excitation. The 500 Hz pump beam is synchronized with the probe, which has a repetition rate of 1 kHz, as configured by an internal pulse picker in Pharos. This repetition rate allows for sufficient time for sample recovery, minimizing the risk of sample damage due to excessive energy deposition or thermal effects.

Blocking every second pump pulse effectively creates two alternating conditions crucial for TAS: one where the sample is exposed to both pump and probe beams (pump + probe), and another where it is exposed only to the probe (probe). Subsequently, the pump beam passes through a neutral density filter, which can be varied to adjust the excitation density. The beam is then guided into the sample chamber. For film samples,

the pump excites the sample from the opposite direction of the probe, minimizing the pump signal from entering the detection cavity due to scattering effects. Solution samples were measured in a 2 mm cuvette with stirring, and in this case, both pump and probe beams were directed onto the front face of the cuvette to minimize temporal dispersion. The relative polarization between the pump and probe beams was set to 54.7° to avoid anisotropic effects in the solution measurements. After overlapping with the probe at a designated point on the sample, the transmitted beam passes through another density filter to avert detector saturation. Finally, within the detection cavity, the beam is focused onto an optical fiber connected to the spectrograph, thereby facilitating spectral analysis.

The control over the excitation density serves to distinguish which artifacts in TA spectra are inherent to the molecules under study and which are artificial due to molecular heating.[3] The neutral density filter is employed to regulate the intensity of the pump beam, measured with a power meter. Additionally, in certain instances, a supplementary set of lenses is used to adjust the beam diameter. This was measured using a LaserCamHR-II beam profiler from Coherent, which utilizes a CCD sensor that captures the incident laser beam. With this, the **excitation density**, ρ, relevant for thin films, is calculated as follows:

$$\rho = \alpha \cdot \frac{P_{in}}{E_{\gamma}} \ [cm^{-3}] \qquad [\ 13\ ]$$

[3] The physical origin of the changes in the absorption spectra due to heating can be attributed to several factors:
Thermal Expansion: As the sample heats up, it undergoes thermal expansion, which can lead to changes in the optical path length and, consequently, the observed absorbance. Population Redistribution: Heating can cause a redistribution of molecular populations across different vibrational, rotational, or electronic states, according to the Boltzmann distribution. This redistribution can alter the ground and excited state populations, affecting the absorption cross-section and leading to changes in the TA spectrum. Non-radiative Decay Rates: Increased temperatures can enhance non-radiative decay processes, altering the lifetime of excited states and affecting the dynamics captured in TA measurements. Band Broadening: Thermal effects can lead to broadening of HOMO-LUMO gap due to increased molecular motion and collisions, affecting the shape and width of the observed ΔA features.

Where the absorption coefficient, α, depends on the measured steady-state absorption, which is wavelength dependent, Abs, in O.D., and on the thickness of the sample, l:

$$\alpha = \frac{\mathrm{Abs}(\lambda)}{\mathrm{l}} \cdot 10^{7}[\mathrm{cm}^{-1}] \qquad [\ 14\ ]$$

The incident power per pulse, $\mathrm{P_{in}}$, is calculated from the measurement of the incident pump power wavelength- dependent, $\mathrm{P_{pump}}$, the laser RR, and the measured pump-beam radius, r:

$$\mathrm{P_{in}} = \frac{\mathrm{P_{pump}}[\mu\mathrm{W}]}{\mathrm{RR} \cdot\ \pi \mathrm{r}^{2}}\ [\mathrm{J} \cdot \mathrm{cm}^{-2}\ \text{per pulse}] \qquad [\ 15\ ]$$

3.4 Transient Absorption Data Analysis

3.4.1 Data Collection

The resulting spectrum is obtained from the difference in absorption at different delay times: $\Delta A(t) = A_{pump+probe}(t) - A_{probe}(t)$, which follows the relationship of the absorption with the measured intensity of light: $A = -\log_{10}(I/I_0)$:

$$\Delta A(\lambda, t) = \log_{10} \frac{I_{pump+probe}(\lambda, t)}{I_{probe}(\lambda, t)} \qquad [16]$$

In the acquired dataset, an absorption spectrum is obtained for a specific pump excitation wavelength for each delay time between the pump and probe pulses. At each wavelength, a distinct absorption intensity is noted. This information can be graphically represented in a two-dimensional plot, where the change in absorbance, $\Delta A(\lambda)$, is plotted against the wavelength range. A spectral trace is delineated for each temporal moment, thereby offering an exhaustive depiction of the spectral characteristics over time, as seen in Figure 14. Additionally, a separate two-dimensional plot elucidates the kinetics of the underlying process. In this graphical representation, the absorption intensity, $\Delta A(t)$, which essentially serves as a data density metric, is plotted against the decay time for a specific wavelength within the experimental range. The entire dataset can also be visualized as a contour plot, wherein the time scale is displayed against the wavelength range and color-coded according to the absorption intensity.

Raw data can be processed for precise scientific interpretation using the Light Conversion-provided Surface Xplorer software. Firstly, despite efforts to deflect the pump beam from the detection module, other residual signals are present in the spectra and must be subtracted. This subtraction is feasible because some spectra are initially measured solely with the probe light, serving as the background signal for subtraction. Secondly, the effects of group velocity dispersion: the initial unprocessed data frequently display pronounced wavelength-dependent curvatures in the time-zero trace at subpicosecond scales. Specifically, blue frequencies are detected before their red counterparts. The correction process typically begins with assessing the cross-correlation instrument response function (IRF) signal. The IRF is essentially a convolution of the shape of the exciting laser pulse with the response of the detector.

The width of the IRF limits the fastest timescale that can be observed in the experiment, which becomes especially significant when investigating ultrafast phenomena on subpicosecond timescales. The software employs a chirp curve fitting algorithm to correct this dispersion, utilizing four strategically selected time-zero points.[139]

Different physical phenomena can be seen in positive or negative features in the data plots of $\Delta A(\lambda, t)$. Specifically, three main contributions represent the energy transitions upon excitation as depicted in Figure 14. Upon excitation, a subset of molecules transitions from the ground state to the excited state. Consequently, the probe beam experiences reduced absorption in the spectral range corresponding to the ground state, manifesting as a negative ΔA(λ,t). This is the **Ground State Bleach** (GSB) and should match, at least partially, the shape of the steady-state absorption spectrum. Molecules in the excited state may relax back to the ground state, accompanied by the light emission, resulting in a second negative ΔA(λ,t) peak corresponding to **Stimulated Emission** (SE). This signal, characterized by a red shift with respect to the GSB, is typically observed in the same spectral range as steady-state fluorescence, which is spontaneous emission. Notably, while spontaneous emission intensity scales with the emission frequency cube (section 3.3.1, Einstein coefficient: $A_{UL} \sim \nu^3 B_{UL}$), SE is linearly proportional to the emission frequency. This implies that SE can be detected even at wavelengths longer than those typical from spontaneous emission. Furthermore, the signal evolves due to solvation and/or geometric alterations of the excited molecule. The positive features are attributed to the **Excited State Absorption** (ESA). This is characterized by the absorption of a photon by an excited state, leading to a transition to a higher excited state. Following electronic excitation, a molecule may reside in a vibrationally excited state within the same electronic manifold. As the system loses this excess vibrational energy, often through interactions with its surroundings, the spectral features corresponding to that particular excited state can shift or broaden. This gives rise to evolving peaks or changes in the band shape in the $\Delta A(\lambda,t)$ spectrum over time.[140]

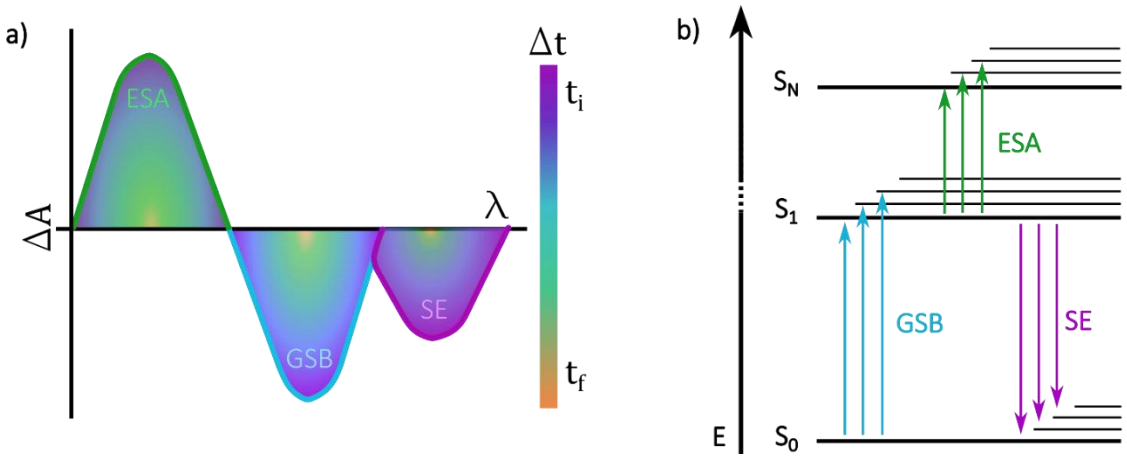

Figure 14: Principal Features of Transient Absorption Spectroscopy (TAS) data. a) Two-Dimensional Plot Illustration: The plot delineates the change in absorbance, ΔA, as a function of the wavelength range. A color scale indicates the temporal evolution of spectral features from initial delay times, t_i, to final delay times, t_f. Positive spectral features are indicative of Excited-State Absorption (ESA), while negative spectral features correspond to Ground-State Bleach and Stimulated Emission. b) The energy Diagram elucidates the type of electronic transitions occurring in a system of singlet multiplicity, correlating with the features observed in the aforementioned spectral plot. Specifically, transitions from the ground state to various excited states can be mapped to explain the observed ESA. At the same time, Ground-State Bleach and Stimulated Emission are attributed to the relaxation processes leading back to the ground state.

3.4.2 Global Analysis

Global analysis is a potent methodology for analyzing data from a TAS.[141] It serves as a comprehensive computational methodology to unravel complex reaction kinetics and spectral evolution of photophysical systems. The data in this thesis were analyzed using the R-package TIMP software with the graphical interface Glotaran 1.5.1.[142]. Unlike conventional point-by-point analysis, which examines each wavelength or time point individually, global analysis treats the entire multi-dimensional dataset, spanning both time and wavelength, as a cohesive entity. The method systematically decomposes complex TAS data into its underlying components, revealing the spectral signatures, kinetic profiles, and decay rates associated with different molecular states or transient species.

The *data matrix* $\Delta A(\lambda,t)$ is given by the superposition of the n_c components dependent on the concentration profile, c_i, and spectrum, s_i, of the component i:

$$\Delta A(\lambda, t) = \sum_{i=1}^{n_c} c_i(t)s_i(\lambda) \quad [17]$$

The initial task is to determine the number of steps in the data, which should correspond to transitions between energy levels upon excitation. This is given by the **Singular Value Decomposition** (SVD) of the dataset. SVD serves as a mathematical tool for breaking down complex matrices, facilitating the identification of independent components, or species, in both spectral and temporal dimensions. The data matrix is characterized by its SVD as follows: $\Delta A(\lambda, t) = \sum_{i=1}^{n_c} u_n(t)w_n(\lambda)SV_n$. Where n_{max} is the maximum of the number of rows and columns. If the de-excitation decay has only one step and the data ideally do not have noise contribution, n_c = 1 and SV_1. In real datasets with noise, the SV are more difficult to be defined. Since the global analysis done with Glotaran is an interactive model, the number of SV is obtained by increasing the number of vectors proposed until the vectors do not show any particular shape different to noise effects. Once the number of decay and recovery steps is known, a certain number of parameters P such as the width of the IRF, time-zero, rate constants and weights of certain regions of the data must be given. The data matrix is modeled as a sum of component matrices that describe the concentration profiles $c_{i,\lambda}(t, P)$ and the corresponding spectra of each component $s_i(\lambda)$:

$$\Delta A(\lambda, t) = \sum_{i=1}^{n_c} c_{i,\lambda}(t, P)s_i(\lambda) \quad [18]$$

In a matrix form, this is given as: $A = C \times S + E$. The residual errors or noise are represented by E. The concentration matrix is modeled as a sum of exponential representing a concentration profile as a function of time and the decay or evolution of different species:

$$C(t) = \sum_{i=1}^{n_c} A_i e^{-k_i t} \quad [19]$$

As a result of the modeling, each decay profile $e^{-k_i t}$ in C is associated with a particular spectrum in S. This spectrum is essentially the Decay-Associated Difference Spectrum (**DADS**) for that component. DADS shows how the spectral features change as the corresponding concentration profile decays over time[125], i.e., DADS tracks absorption changes with specific lifetimes. The Evolution-Associated Difference Spectra (**EADS**) are *calculated spectra* derived from the S matrix, describing the system's temporal evolution. Each column in the S matrix represents a different spectral shape associated with the system's transition between states. Progressively increasing lifetimes, τ, are assigned to each EAD-spectrum. Mathematically, EADS are derived from the SVD of the time-resolved data matrix: $\Delta A(\lambda, t) = \sum_{i=1}^{n_c} c_i^{EADS}(t, P)\ EADS_i\ (\lambda)$.[129,141,143–145] In following chapters the information provided by EADS and DADS will be explained in the context of photophysics of CuPc and Squaraines aggregates.

Chapter 4.

Symmetry - Breaking Charge Transfer and Intersystem Crossing in Copper Phthalocyanine Thin Films

Science has great beauty.

M. Curie[47]

This chapter is based on the publication: Rosendo, E. del P.; Yildiz, O.; Pisula, W.; Marszalek, T.; Blom, P. W. M.; Ramanan, C. *Symmetry-Breaking Charge Transfer and Intersystem Crossing in Copper Phthalocyanine Thin Films*. Phys. Chem. Chem. Phys. 2023, 25 (9), 6847–6856. https://doi.org/10.1039/D2CP05240G. [146]

4.1 Introduction

Phthalocyanines were discovered by accident in 1928 in Scottish Dyes Ltd. while manufacturing phthalimide, a white solid, but observing an insoluble blue material, later patented as iron phthalocyanine. Despite the advances over these hundred years in the industry, the Copper phthalocyanine, $C_{32}H_{16}CuN_8$, referred to as CuPc,[147] is the most used pigment. The derivatives of sulfonation are water soluble and are used as blue dyes for paper and textiles. Green pigments are the result of chlorination.[148–150] But the interest of this chapter resides in CuPc, a robust small molecule OSC which, as other Phthalocyanines, has 18 pi-electrons delocalized along the 16 conjugated p-orbitals forming a ring.[151] CuPc, along with other derivatives, has attracted attention for various applications. In addition to being one of the most commonly used pigments for printing blue ink, cosmetics, or plastic arts, its semiconducting properties make it attractive for optoelectronics and other light-driven applications. CuPc has been used for organic photovoltaics,[1,152–157] light-emitting diodes,[158,159] photodetectors,[160,161] non-linear optics, photocatalysis,[162,163] and photodynamic therapies.[164–166] In thin films, CuPc organizes into different crystalline morphologies depending on the processing conditions. The two most common structures are α-CuPc and β-CuPc.[167,168] Both morphologies are reported to exhibit Frenkel – Charge Transfer mixing, but they also demonstrate differing steady-state optical properties. It remains unclear how the morphology influences the photoexcited dynamics of CuPc thin films. Differences in Frenkel-CT mixing, for example, could strongly alter the potential energy landscape.

Herein, we used transient absorption (pump-probe) spectroscopy to study the photophysical dynamics of α-CuPc and β-CuPc. Due to the intermolecular coupling interactions and Frenkel-CT mixing, the Q-band absorption of the thin films is much broader than that in solution (Figure 15, vide infra). We characterized the photophysical dynamics at various excitation wavelengths across this Q-band absorption. We find that

both α- and β-CuPc thin films exhibit ultrafast intersystem crossing to form ^{3*}CuPc, as is seen in monomeric CuPc as well. However, we also find a unique excitation wavelength dependence in α-CuPc. At bluer excitation wavelengths, we observe a competitive decay pathway to a symmetry-breaking charge transfer photoproduct. We propose that the morphology dependence of our observations arise from differences in electronic and vibronic coupling in α- and β-CuPc.

4.2 Experimental

4.2.1 Sample Preparation

CuPc [(29H, 31H, phthalycaninato(2-)-N29,N30,N31,N32) copper(II)] and 1-chloronaphthalene were purchased from Sigma-Aldrich and used without further purification. The solution sample of CuPc was prepared by first heating the solvent to 60 °C and then adding the CuPc powder. This mixture was subsequently centrifuged and filtered to retrieve a homogenous solution. The final concentration gave an OD of 0.2 at 680 nm in a 2 mm cuvette.

For the thin film samples, quartz substrates (3x3 cm, 1 mm thick) were cleaned in an ultrasonic bath: 10 min. in acetone and 5 min. in isopropyl alcohol. They were then dried under N_2 gas flow. CuPc was vapor-deposited onto the quartz substrates under 10^{-6} mbar vacuum pressure, using a 0.1 Å/s deposition rate. The substrates were heated to and held at 150 °C during the deposition, and the thickness was monitored using a quartz crystal balance. This deposition resulted in α-CuPc thin films. In order to prepare β-CuPc samples, α-CuPc thin films were placed on a hot plate at 300 °C for 10 h.[123,169–172] The final CuPc layer thickness is 50.6 ± 0.8 nm, as determined by surface profilometry (Bruker, DektakXT). The assignment of α- and β-phase morphologies is consistent with the steady-state absorption from literature examples.[44,172,173]

4.2.2 Structural Characterization

Grazing incidence wide-angle X-ray scattering (GIWAXS) measurements were performed at the Dortmund Electron Accelerator (DELTA) Synchrotron Facility (Dortmund, Germany), beamline BL09. The photon energy was set to 10 keV (λ = 1.24 Å). The beam size was 1.0 × 0.2 mm2 (width × height), and the samples were irradiated just below the critical angle for total reflection with respect to the incoming X-ray beam (∼0.1°). All X-ray scattering measurements were performed under vacuum (∼1 mbar) to reduce air scattering and beam damage to the sample. All data processing and analysis were performed using the software package Datasqueeze. See Appendix 6.1. for further details.

4.2.3 Optical Spectroscopy

Steady-state absorption was done using a PerkinElmer Lambda900 spectrophotometer. Transient absorption (TA) spectroscopy was measured using a Helios-Fire pump-probe setup (Ultrafast Systems). This is paired with a regeneratively amplified 1030 nm laser (Light Conversion Pharos, 200 fs, 200 µJ), set at an effective repetition rate of 1 kHz via an internal pulse picker. A small portion (20%) of the 1030 nm fundamental is directed to an optical delay line and, subsequently, to a sapphire crystal to generate the broadband probe light. The remaining 80% of the 1030 nm fundamental is directed to an optical parametric amplifier (Light Conversion, Orpheus-F) to generate the pump pulse at various wavelengths, as detailed further in the Results section. The pump excitation density at the sample was adjusted with a neutral density filter, and the beam diameter was measured using a LaserCamHR-II beam profiler (Coherent). Excitation density calculations are done as explained in section 3.3.3. Film samples were photoexcited from the backside of the sample to minimize pump scatter light entering the detector. Solution samples for TA were measured in a 2 mm cuvette with stirring, and in this case, both pump and probe beams were directed onto the front face of the cuvette to minimize temporal dispersion. The relative polarization between the pump and probe beams was set to 54.7^{o} (magic angle, section 2.4.2.1) to avoid anisotropic effects in the solution measurements. Global analysis[141] of TA data was done using the R-package TIMP software,[174] with the graphical interface Glotaran 1.5.1.[144]

4.3 Results and Discussion

4.3.1 Frenkel Exciton and Charge Transfer Mixing in CuPc Films

Figure 15 shows the steady-state absorption spectrum of CuPc in 1-chloronaphthalene solution as well as in thin films with predominantly α- and β-type morphology. The depicted spectral range between 500-800 nm shows the Q-band absorption region (S_0 → S_1) and agrees with literature examples.[173,175,176]

The solution sample represents the absorption of monomeric CuPc, which is characterized by a primary 0-0 transition at 680 nm (section 2.3.1), and two vibronic peaks at 620 and 645 nm. A single predominant 0-0 transition is expected for metallated phthalocyanines, due to the symmetric molecular geometry.[175] The absorption spectra of both α-CuPc and β-CuPc films are broader than that in solution, and each exhibits two predominant peaks. This splitting of the absorption band is due to excitonic splitting between strongly interacting dimers in the film.[13,16,17] The relative peak ratios differ between the two morphologies, as has been previously reported, and are consistent with changes in neighbor-to-neighbor molecular orientation. The structural organization of the thin films was measured using grazing-incidence wide-angle X-ray scattering (Figure 44). These experiments show that the α-CuPc shows a characteristic herringbone structure, while the β-CuPc film is polymorphic, but with clear evidence of larger molecular displacement between neighboring molecules within the stacks in the co-existing β-phase. The predominance of the blue (higher energy) peak in α-CuPc can be attributed to a more face-to-face π-stacking arrangement (Figure 6a) and thus stronger intermolecular coupling, while β-CuPc exhibits a more slip-stacked arrangement (Figure 6c), consistent with a red (lower energy) shift.[172,177–179] More details on the GIWAXS measurements and analysis can be found in Appendix 6.1.

In addition to excitonic splitting due to interacting dimers, the steady-state absorption in the solid state represents a mixed contribution between molecular excitons and a charge-transfer state which runs parallel to the π-stacking direction. In α-CuPc, the peaks at 625 and 690 nm are assigned to the first and second π–π* transitions on the phthalocyanine macrocycle, respectively, which represent the two lowest energy Frenkel excitons (F1, F2).[180,181] The Q-band absorption in α-CuPc also exhibits two

shoulders at ~580 and 725 nm, which arise as a result of excitonic mixing with an intermolecular CT state.[39,40] The absorption spectrum is therefore comprised of four overlapping peaks, representing a mixture of the two lowest energy intramolecular Frenkel excitons in CuPc (F1, F2) with an intermolecular charge-transfer state (CT), which is oriented through the crystalline stack (Figure 15). The presence of such an intermolecular charge-transfer state coupled to the intramolecular Frenkel excitons has been identified in both α-CuPc and β-CuPc.[38,42,44,182–184] The spectral lineshape for the β-CuPc steady-state absorption can therefore be similarly explained, with the predominant peaks at 640 and 725 nm being assigned to the first and second π–π* transitions on the phthalocyanine macrocycle, and lower intensity shoulders contributing due to the four-fold (F1, F2)-CT mixing. In the following, we explore how this mixing mediates photophysical dynamics in α- and β-CuPc.

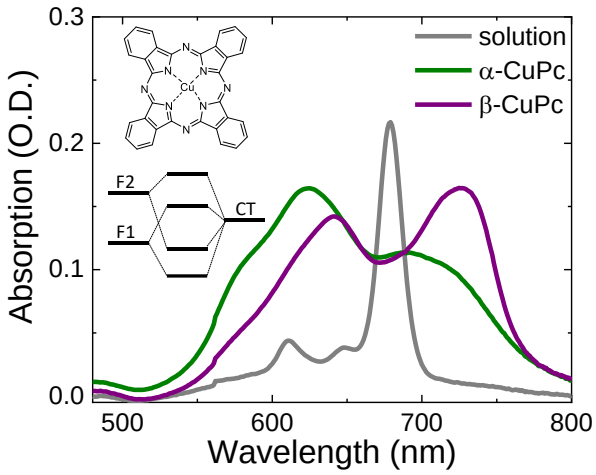

Figure 15: Steady-state absorption of CuPc in 1-chloronaphthalene solution and in thin films with α- and β-phase stacking morphologies in the spectral range of the Q-band absorption. The film samples exhibit different absorption peak positions and relative intensities due to changes in intermolecular couplings. Upper left: chemical structure of the monomer with the energy diagram of the mixed Frenkel-CT states below.

4.3.1.1 Ultrafast Intersystem Crossing in Monomeric CuPc

Figure 16a shows TA spectra (λ_{ex} = 670 nm) of monomeric CuPc, measured in 1-chloronapthalene solution. The spectra exhibit negative features at 620, 645, and 680

nm, matching the peaks from steady-state absorption (overlaid in grey), which are attributed to ground-state bleach (GSB). The CuPc solution TA spectra also exhibit broad positive features between 480-600 nm, attributed to excited state absorption (ESA). As the zoomed-in inset of Figure 16a shows, there is an increase in the ESA below 500 nm within the first 5 ps (blue to green traces). The solution TA data were fit using a two-compartment sequential global analysis model, and the resulting evolution associated difference spectra (EADS) are shown in Figure 16b. The black trace represents the first EADS and corresponds to features appearing immediately after photoexcitation. In addition to the GSB features previously noted, there is also a negative contribution to the differential absorption spectrum at ~725 nm and a broad ESA from 525-850 nm, which overlaps the negative features. This evolves in 340 fs to the second EADS (red), wherein the GSB features persist, but the negative feature at 725 nm has disappeared. Furthermore, the ESA has blue-shifted and now shows a predominant peak at 500 nm. The transient kinetics within the first 10 ps are shown in the inset of Figure 16b along with the fits from global analysis and confirm that the ESA at 590 nm disappears concomitantly with the rise of the ESA at 500 nm. This second EADS lives beyond the 8 ns measurement window of our experiment.

In order to describe the photophysics of monomeric CuPc and these EADS, we refer to earlier literature reports of intersystem crossing (ISC) in phthalocyanines.[185–190] CuPc in solution has previously been shown to exhibit no measurable fluorescence, but does exhibit phosphorescence.[191–193] The first EADS is therefore assigned to the population of the singlet excited state, S_1, and this furthermore agrees with previously reported TA of ZnPc in solution.[188,194,195] The slight negative dip in the first EADS at 725 nm is attributed to a vibronic transition of the stimulated emission, based on the agreement with previous reports of CuPc fluorescence measured via upconversion.[196,197] The singlet excited state then undergoes ISC within 340 fs to yield the triplet excited state (T_1), represented by the second EADS. This assignment is consistent with the disappearance of the SE band as well as the long lifetime (> 10 ns). The T_1 ESA lineshape also agrees with earlier flash-photolysis measurements, which furthermore show that the CuPc triplet in solution has a lifetime of 35 ns.[185]

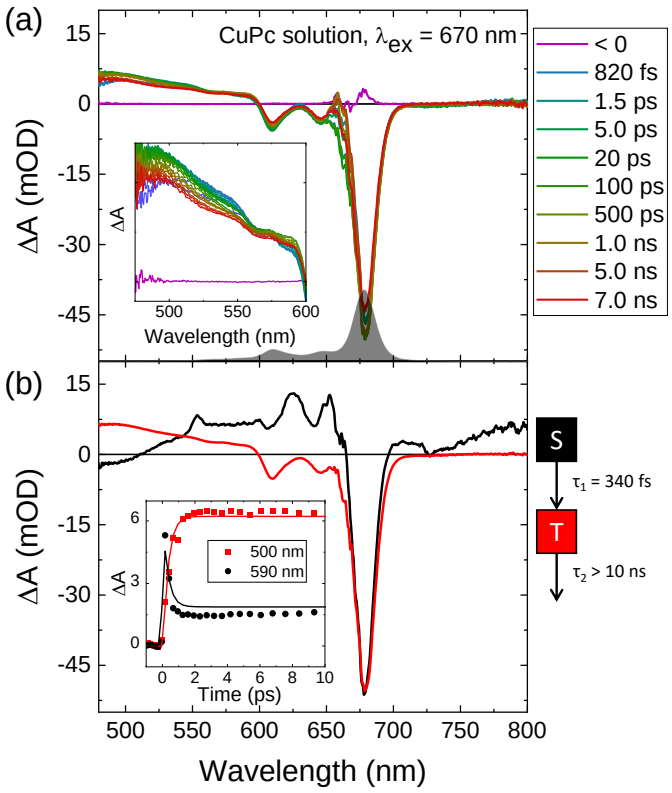

Figure 16: (a) TA spectra at selected time delays of CuPc in 1-chloronaphthalene photoexcited at λ_{ex} = 670 nm. Inset shows a zoom in of the ESA features between 480-600 nm, which blue shift in the first few traces. The steady-state absorption profile of CuPc in 1-chloronaphthalene from Figure 15 is overlaid for comparison. (b) EADS from global analysis of the TA data, fit to a sequential two compartment scheme consistent with ultrafast intersystem crossing to a long-lived triplet state. Inset shows transient kinetics and fits comparing the decay of the singlet ESA at 590 nm and growth of the triplet ESA at 500 nm.

4.3.1.2 Excitation Wavelength Dependent TA of CuPc Thin Films

TA experiments for both α-CuPc and β-CuPc thin films were carried out using various excitation wavelengths across the Q-band absorption, chosen to approximately coincide with the energies of the four-fold mixed (F1, F2)-CT states. These data are shown as contour plots in Figure 17a-d and Figure 18a-d for the full temporal measurement window, out to 7 ns. The excitation power at the sample was adjusted to maintain approximately equal excitation density at all of the pump wavelengths (Table 1 and Table 2).

Wavelength (nm)	580	620	680	720
Ex. Density (cm^{-3})	$1 \cdot 10^{18}$	$1 \cdot 10^{18}$	$8 \cdot 10^{17}$	$9 \cdot 10^{17}$

Table 1: Excitation density at each excitation wavelength for the α-CuPc thin film.

Wavelength (nm)	580	620	680	720
Ex. Density (cm^{-3})	$2 \cdot 10^{18}$	$2 \cdot 10^{18}$	$7 \cdot 10^{18}$	$4 \cdot 10^{18}$

Table 2: Excitation density at each excitation wavelength for the β-CuPc thin film.

In α-CuPc, (Figure 17) all contour plots show positive features between 480-550 nm, and negative features between 600-750 nm. There is also a strong negative contribution between 560-580 nm, which appears with highest relative intensity at λ_{ex} = 580 nm (red arrow, Figure 17**a**) and has a diminishing contribution as the excitation energy shifts to longer wavelengths. The β-CuPc contour plots (Figure 18) show positive features between 480-600 nm and at 700 nm, with negative contributions between 600-650 and 725-800 nm. In contrast to the α-CuPc sample, there are no obvious excitation wavelength dependent differences in the β-CuPc sample from the contour plots.

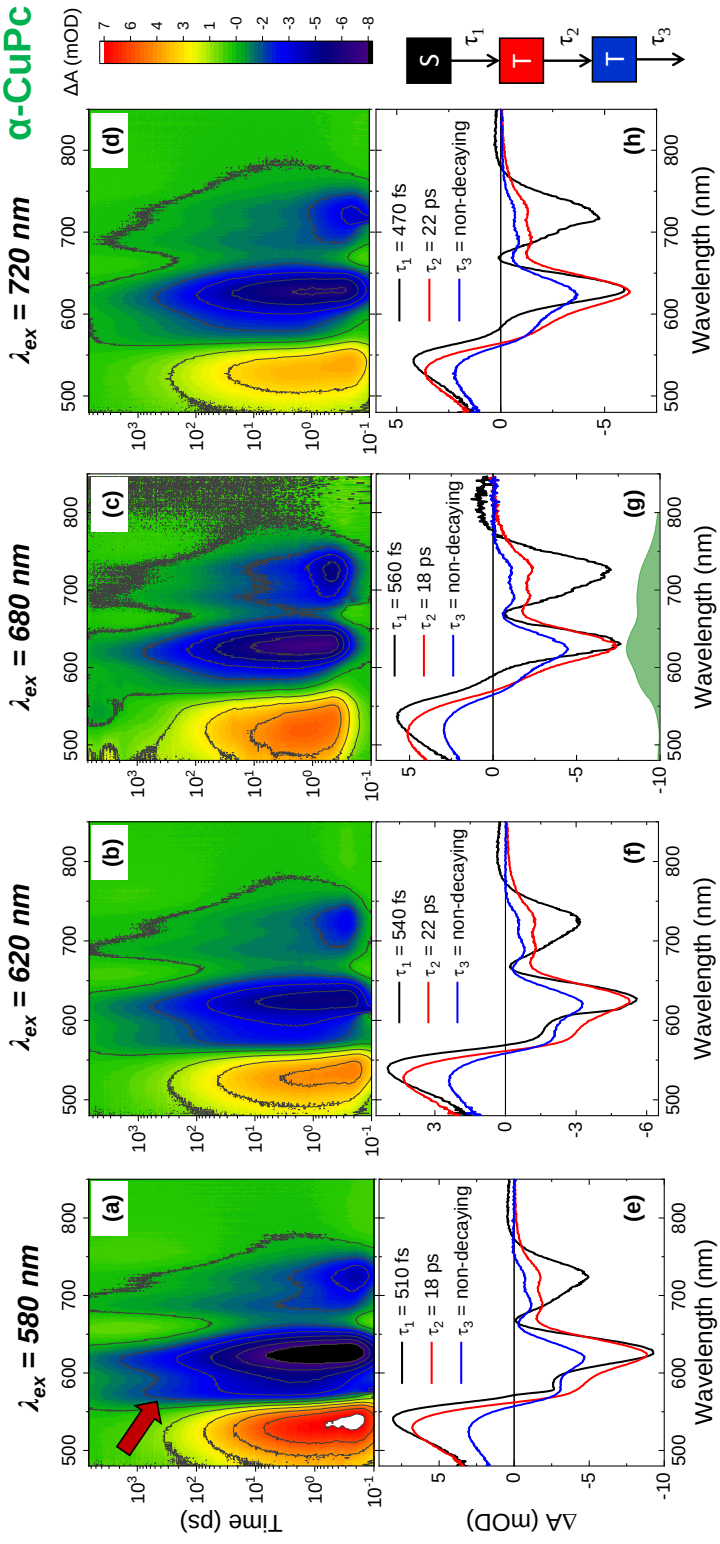

Figure 17: (a-d) Contour plots of the TA measurements carried out on α-CuPc thin films photoexcited at various wavelengths across the Q-band absorption. For each sample, the excitation density was scaled to be similar at all excitation wavelengths. Red arrow:

α-CuPc shows a negative band at 575 nm (red arrow) which is strongest at λ_{ex} = 580 nm and has a diminishing contribution as the excitation energy is red-shifted. (e-f) EADS from global analysis of the first 50 ps also shows excitation wavelength dependent differences. The steady-state spectrum of the α-CuPc thin film from Figure 1 is reproduced in (g) for lineshape comparison.

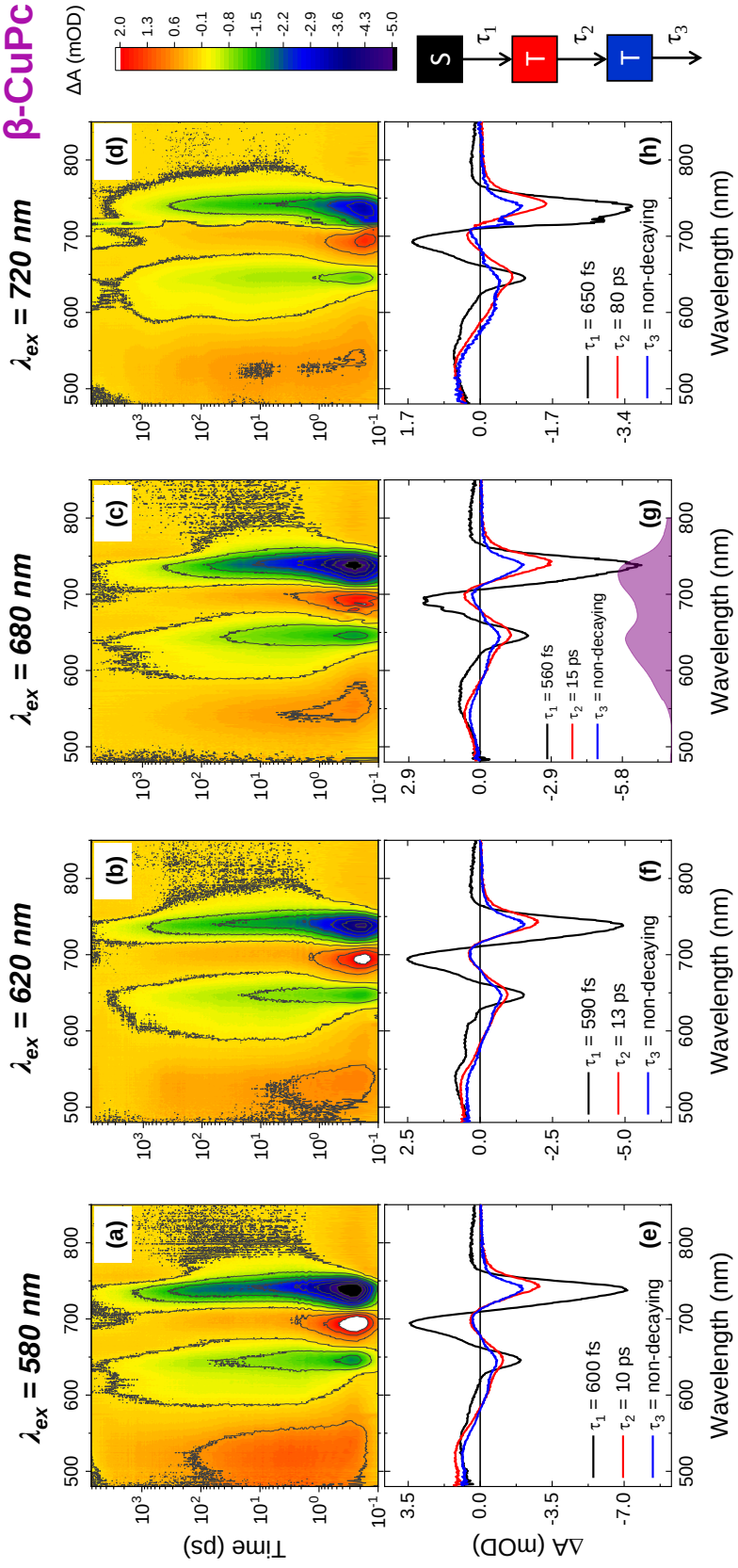
β-CuPc
λex = 580 nm
λex = 620 nm
λex = 680 nm
λex = 720 nm
ΔA (mOD)
2.0
1.3
0.6
-0.1
-0.8
-1.5
-2.2
-2.9
-3.6
-4.3
-5.0
S
T
T
τ1
τ2
τ3
(a)
(b)
(c)
(d)
(e)
(f)
(g)
(h)
Time (ps)
ΔA (mOD)
Wavelength (nm)
τ1 = 600 fs
τ2 = 10 ps
τ3 = non-decaying
τ1 = 590 fs
τ2 = 13 ps
τ3 = non-decaying
τ1 = 560 fs
τ2 = 15 ps
τ3 = non-decaying
τ1 = 650 fs
τ2 = 80 ps
τ3 = non-decaying

Figure 18: (a-d) Contour plots of the TA measurements carried out on β-CuPc thin films photoexcited at various wavelengths across the Q-band absorption. The excitation density was scaled to be similar at all excitation wavelengths. No clear differences emerge based on excitation wavelength for β-CuPc. (e-f) EADS from global analysis of the first 50 ps also shows similar spectral lineshapes at all excitation wavelengths. The steady-state spectrum of the β-CuPc thin film from Figure 1 is reproduced in (g) for lineshape comparison.

In order to elucidate excitation dynamics, we used global analysis to fit the TA data. The data was truncated to the first 50 ps to avoid heating artefacts. TA experiments on thin film samples are highly susceptible to local heating effects, and it is critical to avoid misinterpretation of a heat-induced spectral feature as a photoproduct.[198,199] Excitation density dependent measurements reveal the line shape which arises from local heating in α- and β-CuPc (Figure 19). Spectral traces of the TA data at selected pump-probe delay times indicate that the heating effects in these thin films appear only at longer timescales (Figure 20), in agreement with the literature.[186,198] We therefore limit the global analysis to the first 50 ps of the experiment window, where we are confident that heating effects are minimal. The resulting EADS from global analysis of α-CuPc and β-CuPc TA data are shown in Figure 17e-h and Figure 18e-h, respectively. Datasets for both samples are well fit with a sequential 3-compartment model, and each of these compartments will be further referred to as EADS 1, 2, 3, with specificity for the sample as EADS 1(α/β) when appropriate.

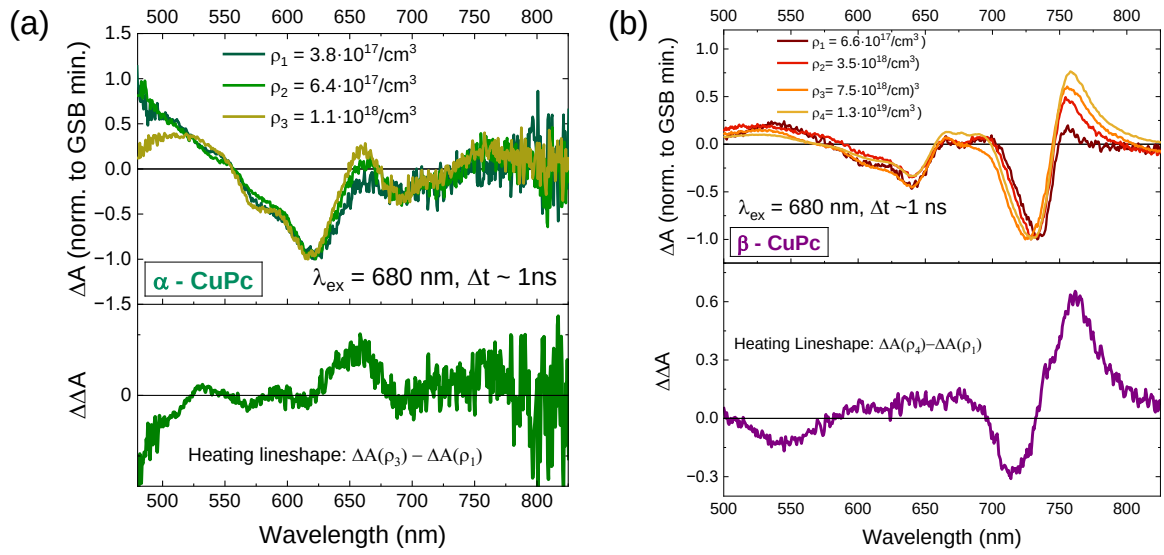

Figure 19: TA measurements with increasing excitation density are used to elucidate the ΔA signal that arises due to local heating effects for (a) α-CuPc and (b) β-CuPc thin films.

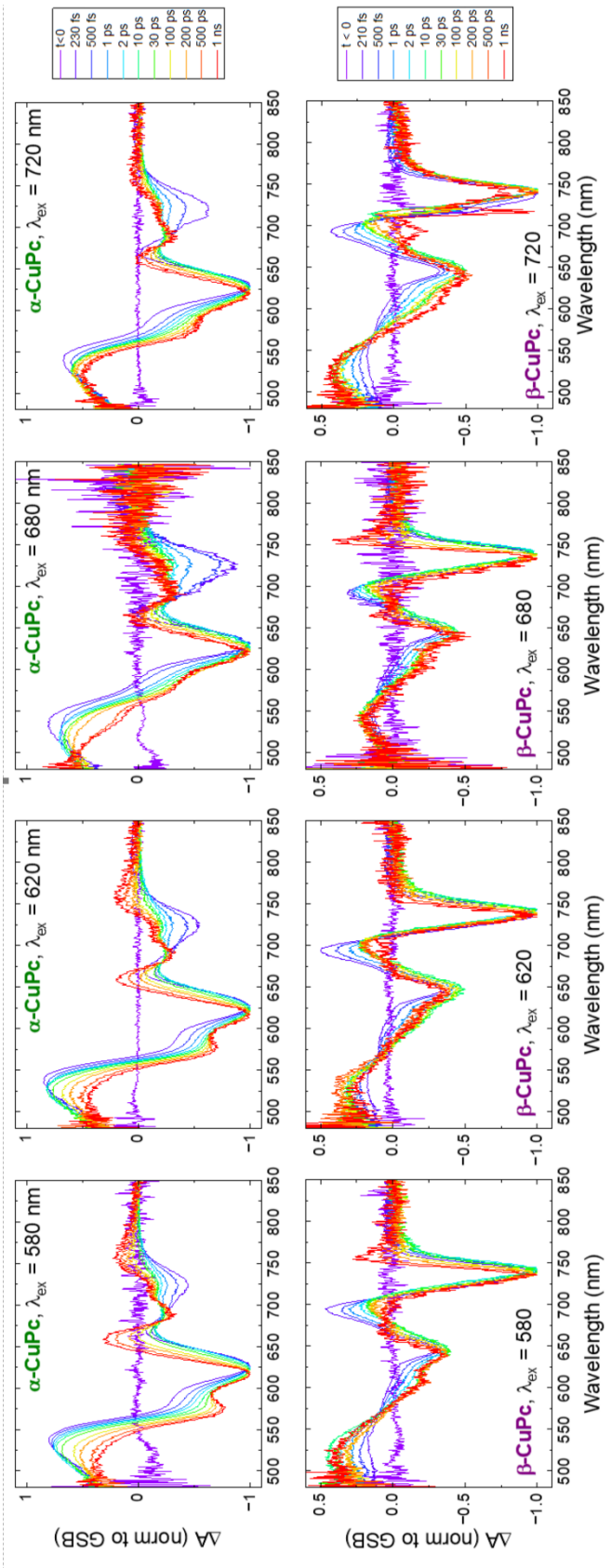
α-CuPc, λex = 580 nm
α-CuPc, λex = 620 nm
α-CuPc, λex = 680 nm
α-CuPc, λex = 720 nm
β-CuPc, λex = 580
β-CuPc, λex = 620
β-CuPc, λex = 680
β-CuPc, λex = 720
ΔA (norm to GSB)
Wavelength (nm)
t<0
230 fs
500 fs
1 ps
2 ps
10 ps
30 ps
100 ps
200 ps
500 ps
1 ns
t < 0
210 fs

Figure 20: Normalized spectral traces at selected delay times for α-CuPc and β-CuPc thin films indicate that heating artifacts, evidenced by the blue shifting of the GSB and appearance of other features shown in Figure 44, appear later delay times (> 100 ps).

At all excitation wavelengths and in both samples, EADS 1 is attributed to the population of the singlet excited state. The positive features of EADS 1 are ascribed to S_1 absorption. In EADS 1α, the S_1 ESA appears as a broad feature from 480-550 nm with a peak at 545 nm. In EADS 1β, the S_1 ESA exhibits a broad peak from 480-600 nm and a strong absorption at 690 nm. The apparent differences are due to the differing interference with the sample GSB, but the general position of the S_1 ESA is the same for both α-CuPc and β-CuPc and also agrees with the solution S_1 ESA (Figure 16b). The negative features of EADS 1 are characterized by a mix of GSB (550-750 nm) and SE (725 nm). In the case of EADS 1α, the SE exhibits a relatively larger intensity at longer excitation wavelengths, as compared with the GSB peak at 620 nm. In contrast, in EADS 1β, the relative intensity of the SE band compared to the GSB (640 nm) does not change with excitation wavelength.

EADS 1 evolves into EADS 2 with the time constant τ_1 and, at all measured excitation wavelengths, this is accompanied by quenching of the SE. This is consistent with ISC from S_1 to T_1, with τ_1 representing the ISC rate. The consistent ISC rate of ~500 fs for all samples agrees with the solution measurement. EADS 2 and EADS 3 have a similar line shape, suggesting that in the CuPc films the resulting T_1 decays biexponentially, with a faster rate on the order of ~10s of picoseconds and a slower rate on the order of nanoseconds. The faster decay is likely due to annihilation effects in the crystalline thin films.[200] The slower decay is fixed as a non-decaying feature within this time window, but based on the full time range of data (Figure 20) we can approximate that T_1 fully recovers to the ground state on the order of nanoseconds, in agreement with literature.[186] The spectral evolution from EADS 1 to EADS 2 is accompanied by a blue-shift of the ESA, yielding a T_1 ESA with peak at ~530 nm. This is in agreement with the T_1 ESA from solution (Figure 16). In EADS2α, the quenched SE also reveals underlying GSB features, and the four GSB peaks in EADS2α correspond exactly to the two peaks and two shoulders from the steady-state absorption. As described above in Figure 15,

these arise from the (F1,F2)-CT mixing in the film. However, the two lower energy peaks are much smaller in ratio to the higher energy peaks when compared to the ground-state spectrum. This suggests the presence of an additional T_1 ESA between 675-800 nm, which is destructively interfering with the GSB in this region. Such an ESA is consistent with earlier literature reports on CuPc films,[201] as well as with EADS 2β which shows a positive feature at 700 nm. Similar to the GSB of EADS2α, EADS 2β shows multiple GSB peaks, consistent with (F1, F2)-CT mixing.

EADS 1/2/3β exhibit similar line shape at all excitation wavelengths. In contrast, EADS 1/2/3α have some distinct differences based on excitation wavelength. As has been mentioned above, the SE feature exhibits a higher relative intensity compared to the GSB with longer excitation wavelength. In addition, there is a negative feature between 560-580 nm, which appears strongest at shorter excitation wavelengths, as expected from the contour plots. Furthermore, the relative intensity of the ESA in the 480-550 nm range is higher at shorter excitation wavelengths. Figure 21 compares the spectral line shapes of the decay-associated difference spectra (DADS) for the fastest decay at each excitation wavelength, which indicates the spectral changes that occur with the associated decay time.[141,144] In the β-CuPc data, the line shapes all follow the same shape independent of excitation wavelength. However, in the α-CuPc data, the line shapes strongly differ in the range of 525-625 nm. Here, the α-CuPc DADS exhibit two peaks at 560 and 600 nm, and the peak ratios depend on the excitation wavelength. At λ_{ex} = 580 nm and 620 nm, the peak at 560 nm predominates, while at λ_{ex} = 680 nm and 720 nm, the peak at 600 nm is higher.

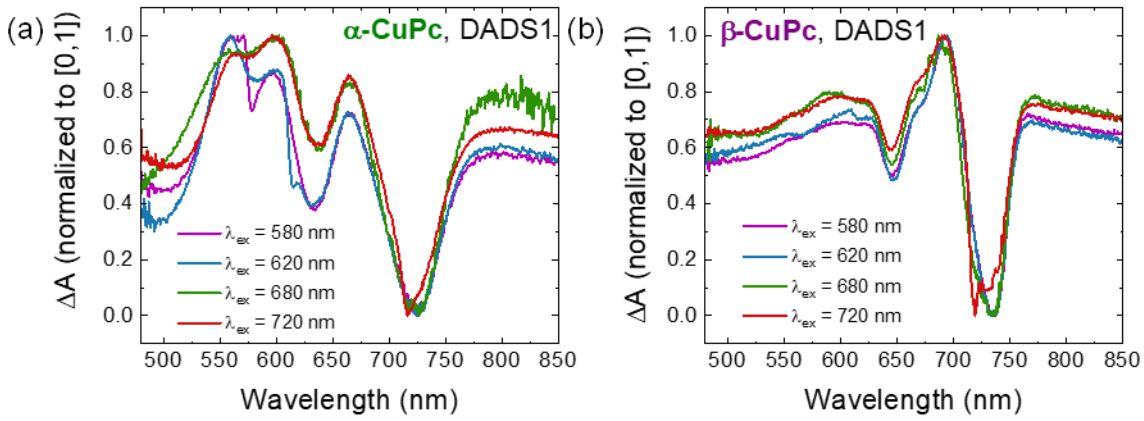

Figure 21: Comparison of Decay-Associated Difference Spectra for (a) α-CuPc and (b) β-CuPc thin films show an excitation dependent lineshape between 550-600 nm for α-CuPc that does not appear for β-CuPc.

We highlight these differences further by comparing the transient kinetics at different excitation wavelengths for both α-CuPc and β-CuPc. Figure 22 shows the transient kinetics monitored at select wavelengths. The transient kinetics at 725 nm (α-CuPc) and 740 nm (β-CuPc) depict the SE quenching followed by GSB decay, and therefore follow the ISC process. This is independent of excitation wavelength for both α-CuPc and β-CuPc, in agreement with literature.[186] As our solution measurements (Figure 16) and earlier work[185] has shown, ISC in CuPc is intrinsic to the monomer, and occurs following excitation into the intramolecular Frenkel exciton plane.

However, the transient kinetics monitored at 560 nm show a marked dependence on excitation wavelength in α-CuPc. Here, the ΔA signal begins positive and then later becomes negative. As Figure 22a shows, the rate of this change is faster for shorter excitation wavelengths. This is the same region associated with S_1 ESA decay and could point to a change in the rate of $S_1 \rightarrow T_1$. But, since the SE quenching does not exhibit the same dependence, this change is not due to the ISC. Instead, this observation suggests an additional photodynamic feature which appears differently depending on excitation wavelength.

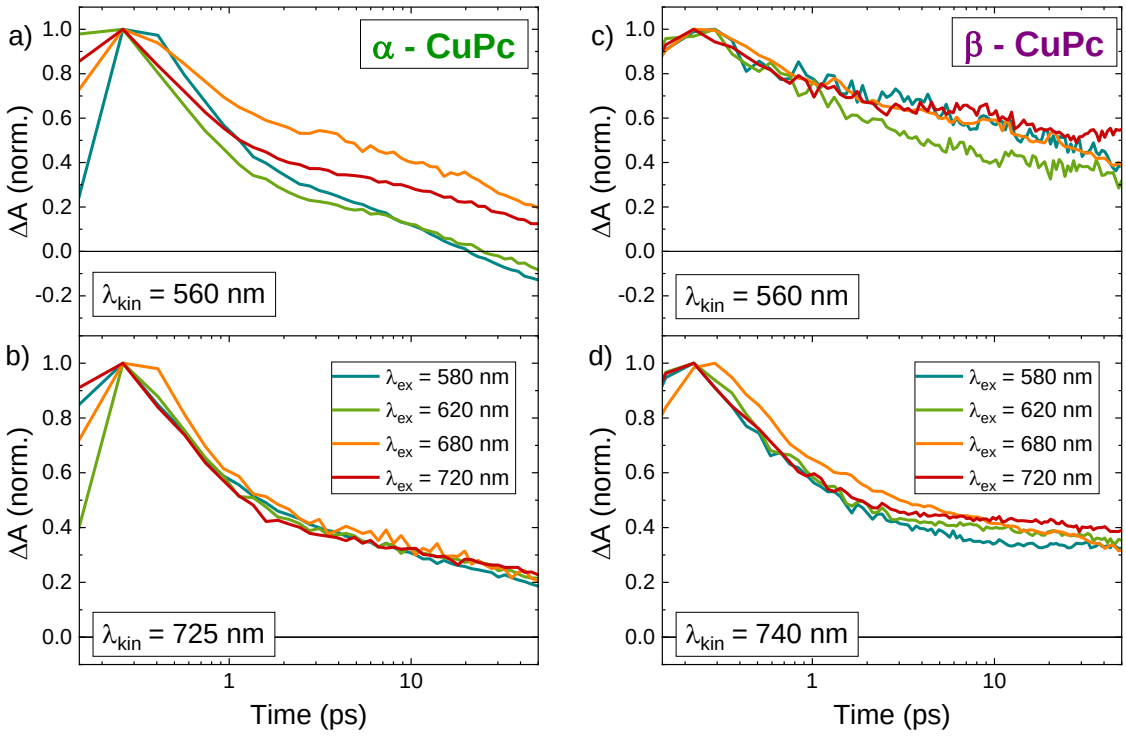

Figure 22: Transient kinetics for (a,b) α-CuPc and (c,d) β-CuPc thin films show that at 560 nm, the α-CuPc decay dynamics vary with excitation wavelength. The decay dynamics of β-CuPc at 560 nm do not exhibit any such dependence. Furthermore, the kinetics associated with the SE quenching at 725 and 740 nm do not depend on the excitation wavelength in either sample. Data truncated to the first 50 ps.

4.3.1.3 Symmetry-Breaking Charge Transfer in α-CuPc

Based on the contour plots, global analysis, and comparison of the transient kinetics, we conclude that the α-CuPc thin film exhibits a unique excitation wavelength dependence in its photophysics, described by an additional spectral feature around 560 nm. The question then remains to explain the origin of this feature in α-CuPc, and why it appears only in this morphology. Figure 23 shows the difference spectrum (ΔΔA) between λ_{ex}=580 and λ_{ex}=720, calculated for both EADS1α and EADS2α to highlight the excitation dependent changes. The ΔΔA spectra show a positive contribution between 480-550, with a peak at ~530 nm, a negative feature between 550-625 nm. ΔEADS1α also shows a positive feature at 725 nm.

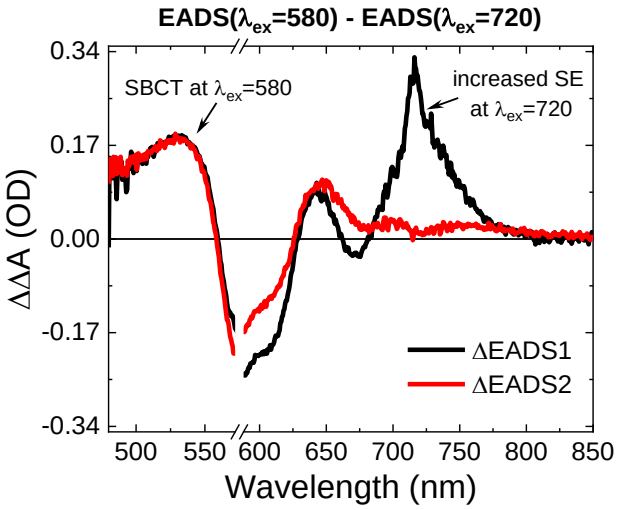

Figure 23: Calculated difference spectrum between EADS fits for α-CuPc thin film excited at λ_{ex} = 580 nm and λ_{ex} = 720 nm shows features consistent with symmetry breaking charge-transfer at λ_{ex} = 580 nm and increased relative stimulated emission at λ_{ex} = 720 nm.

We first consider if the excitation wavelength dependence could be a local heating artifact. Our own measurements and literature[186] report that local heating effects can produce a ΔA spectrum with a negative feature at 570 nm (Figure 19). However, the heating effects in these samples do not appear until after 100s of picoseconds, while the excitation wavelength dependent feature appears at very early times. In addition, the ΔΔA line shape in Figure 23 also exhibits significant differences from the heating line shape. In particular the ΔΔA exhibits a positive feature in the region of 530 nm. We further confirm that this line shape is not due to local heating by comparing the spectral line shapes at λex = 680 at different excitation densities (Figure 24). At delay times of 1 and 10 ps, the spectral line shapes match. We therefore conclude that the additional spectral feature in α-CuPc is not a heating effect.

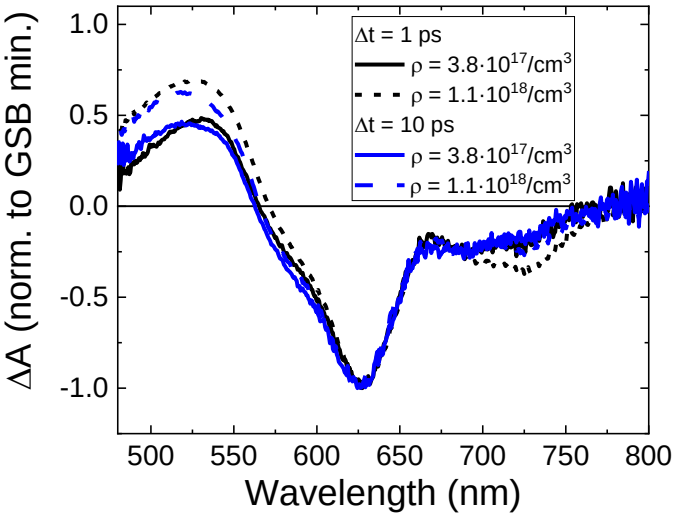

Figure 24: The spectral lineshape at Δt = 1 ps and 10 ps for α-CuPc at different excitation densities are similar, further confirming that the excitation wavelength dependent feature is not a heating artefact.

The region around 560-580 nm has also been identified as the spectral range where the intermolecular CT state exhibits a strong contribution in both α-CuPc and β-CuPc.[41,44,182–184] The excitation dependent feature identified in Figure 23 furthermore agrees well with published work reporting the cation spectrum measured for an α-CuPc thin film.[201] Recent work has also reported symmetry-breaking charge transfer and separation (SBCT) for a ZnPc dimer, and the spectral line shape of SBCT in that work matches closely with the ΔΔA spectrum in Figure 23 of this work, albeit at a shifted spectral position due to the shorter range coupling in the dimer.[202] Based on this evidence, we assign the ESA between 480-550 nm, which appears selectively at shorter-wavelength excitation, to SBCT through the α-CuPc stack. This feature is further accompanied by a GSB associated with the intermolecular CT band. In addition, the positive peak at 725 nm in ΔEADS1α is consistent with the earlier observation of a relatively higher degree of SE at longer excitation wavelengths.

4.3.1.4 Morphology Dependence of Mixed Electronic Pathways in CuPc

Our results point to the following picture for the excited state dynamics in CuPc solution and thin films (Figure 25): In solution, the lowest Frenkel excitons F1, F2 are degenerate. Following excitation into the Frenkel exciton plane, ISC proceeds via a spin-exchange

interaction between the Cu metal centre and the π-ring ligands, which forms an intramolecular CT state in the molecule.[203–205] This offers an efficient pathway to ISC, without any spin-orbit coupling required.

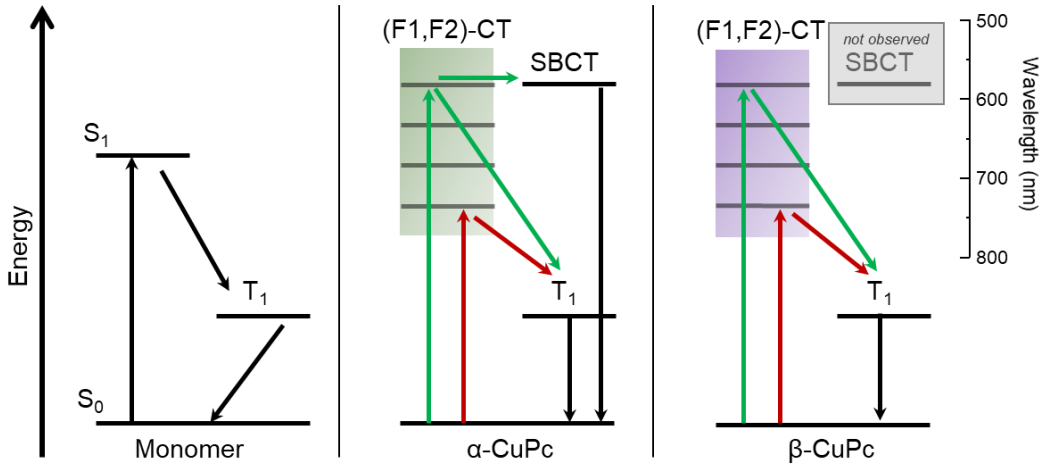

Figure 25: Summary of photoexcited pathways in CuPc. The monomer exhibits ultrafast ISC followed by decay to the ground state. In α-CuPc and β-CuPc, the lowest excited states are spread over a broad range of energies due to the (F1,F2)-CT mixing. In α-CuPc, longer wavelength excitation leads to ISC, while shorter wavelength excitation leads to a competition between ISC and SBCT. In β-CuPc, only the ISC pathway is observed, independent of excitation wavelength. (Energies not to scale.)

In crystalline thin films, the degeneracy of the F1,F2 excitons is lifted, due to reduced symmetry. Since the ISC occurs intramolecularly, it is reasonable that this still occurs in the thin films.[186,206,207] Furthermore, the formation of the intermolecular CT state can also impact the photophysical pathways. As described in the text above, the multiple peaks associated with the steady-state absorption in α-CuPc and β-CuPc thin films arises from a mixture of the two lowest energy intramolecular Frenkel excitons in CuPc with an intermolecular charge-transfer state, which is oriented through the crystalline stack. The transition dipole moment of such a CT state will typically be small, but coupling to a Frenkel exciton can facilitate intensity borrowing, and allow for direct excitation into the CT state.[28,184] Photoexcitation of these crystalline thin film samples will lead to a coherent Frenkel/CT state, with varying character depending on electronic and vibrational coupling arising from the molecular packing.[20,116,208,209]

We therefore propose that in α-CuPc, longer wavelength excitation populates states with predominantly Frenkel (F1, F2) exciton character, yielding competitive SE and ISC, followed by triplet decay. Shorter wavelength excitation, on the other hand, leads to multiple pathways in α-CuPc. Some of the excited state population still decays via SE+ISC. But another pathway also emerges, wherein excitation populates an excited state with significant CT character, resulting in formation of a symmetry-breaking charge-transfer state, through the intermolecular stack. This is consistent with photocurrent measurements, which have indicated the formation of free charges in α-CuPc thin films upon direct excitation of the CT band.[183] These results also explain the reduced SE at shorter-wavelength excitation, as the excited state with significant CT character will not exhibit SE.

Previous work has reported SBCT in π-stacked MgPc and OTiPc, and in the latter case especially this was reported in various morphologies.[210,211] The contribution of a CT state to the absorption in the region of 560-570 nm is also present in β-CuPc.[43,44,182] But the sample with predominantly β-CuPc morphology exhibits no clear evidence of any excitation wavelength dependence from these experiments. In β-CuPc, our results suggest that a single pathway for ISC dominates, wherein excitation leads to excited states with predominately Frenkel exciton character, and subsequent ISC via the same spin-exchange mechanism as in the monomer.

The reason for selective SB-CT in α- vs. β-CuPc morphologies can be attributed to both the differences in molecular packing as well as differences in vibronic coupling. The smaller Cu-Cu molecular packing distance in α-CuPc could lead to optimal electronic coupling for SBCT.[212,213] The GIWAXS measurements furthermore indicated that the β-CuPc thin film exhibits two phases, and this could have an impact on the disorder mediated photophysical decay pathways. Vibrational spectroscopy of SnPc showed that direct excitation of the CT is associated with intermolecular vibrational modes through the π-stacks.[208] Changes in vibronic coupling between the two morphologies can also be responsible for the observed photophysical differences. Previous work has shown that the CT state in α-CuPc is resonant with intramolecular vibrational energies in CuPc, but that this does not hold for β-CuPc.[44,182] Vibronic coupling has been purported to

facilitate and possibly accelerate SB-CT processes.[209] On the other hand, the vibronic spacing of the CT band in β-CuPc has also been shown to correlate with a vibrational mode associated with a pair of ionized CuPc molecules.[44] Therefore, another possibility is that the SBCT is occurring in β-CuPc, but remains more localized and recombines quickly. From the present experiments, it is not possible to distinguish between these two possibilities. However, the essential finding remains that α-CuPc and β-CuPc exhibit distinct photophysical behavior arising from the changes in vibronic as well as electronic coupling, which emerge due to the changes in morphology.

4.3.2 Conclusions

In this work, we have characterized the photophysical dynamics of the organic chromophore CuPc in solution and in two different solid-state morphologies, α-CuPc and β-CuPc. Transient absorption spectroscopy characterizes intramolecular ultrafast intersystem crossing (ISC) in CuPc in solution, which also occurs in the thin film. Our results further show an additional photodynamic feature in the transient spectra of α-CuPc, the appearance of which is furthermore excitation wavelength dependent. We identify this additional photoproduct as a symmetry-breaking charge transfer through the α-CuPc stack, which appears selectively upon excitation into the intermolecular CT band. Direct excitation of this intermolecular CT band is made possible by the strong mixing and resultant intensity borrowing to the Frenkel exciton manifold. The differences in molecular packing and spacing in α-CuPc and β-CuPc lead to differences in electronic and vibrational coupling, and this is why the SBCT state is only observed in the α-CuPc thin film.

These results suggest how intermolecular coupling and morphology mediate competitive photophysical pathways in organic chromophore systems and could be used to design organic materials with selective pathways along mixed electronic states.

Chapter 5.

Stacking Mediated Photophysics in Squaraine Thin Films

One never notices what has been done; one can only see what remains to be done.

M. Curie[47]

5.1 Introduction

The goals of the experiments described in this chapter, which include steady-state absorption, fluorescence, transient absorption spectroscopy, and time-resolved photoluminescence, are to analyze stacking-mediated photophysics and explore possible *singlet fission* (SF) in aggregates of squaraines (SQ). These aggregates are compared and categorized into amorphous and slip-stacked n-alkyl squaraines.

Michl and Smith have shown that slip-stacked aggregates, which are predisposed to strong charge transfer (CT) interactions, as seen in Chapter 2, offer a promising arrangement for SF.[214–216] SF efficiency is expected to be highly dependent on the vibrational coupling.[217–219] Squaraine solar cell performance suffers from low and/or unbalanced mobility and, consequently, a low fill factor. Typical power conversion efficiencies are ~2.5%. If SQ undergo SF, then light absorption could result in exciton trapping in low energy triplet states that either do not undergo efficient charge separation with acceptor molecules, and/or do so, but at the result of significant current and voltage losses. If SQ undergo SF, this significant new finding would therefore impact the design of solar cells incorporating these materials.

5.2 Singlet Fission

Singlet fission is a spin-allowed internal-conversion process that occurs as a result of the spin dipole-dipole interaction in groups of chromophores from the same molecule or between neighboring molecules of an aggregate, by which one chromophore, excited in the singlet manifold, interacts with a neighboring chromophore, by sharing its *delocalized* excitation energy with the neighbor, to result in the creation of a *localized* triplet exciton on each constituent chromophore. This can happen only if the following condition is fulfilled: $E_{S_n} \geq NE_{T_1}, \forall N \geq 2$. *Ideally*, this condition should apply to N neighboring chromophores, implying that the excitation energy, E, can be distributed across the entire system of N chromophores. However, experimental observations have only shown this effect occurring between two chromophores.[214,215]

The process is typically a two-step procedure: $S_0 + S_1 \rightarrow {}^1(TT) \rightarrow T_1 + T_1$.[4] The initially excited chromophore in singlet state, S_1, whose neighboring molecule is in S_0, changes to a correlated triplet-pair state of local triplet states coherently paired into an overarching *singlet*, $^1(TT)$. Therefore, this transition is spin-permitted and characterizes the internal conversion dimension of SF. This singlet state, $^1(TT)$, will dissociate and localize into two independent triplets: T_1T_1. The energy conservation requirement of the whole process is given as:

$\boldsymbol{E_{S_0S_1} \geq 2E_{T_1T_1}}$, which is an exoenergetic process, Figure 26.

The difficulty of this process lies in the necessity of having at least two excitation sites to house the two triplet excitations. In many organic molecules, the energy of the triplet is significantly higher than half the energy of the singlet state. To fulfill this condition, thermal activation of the S_1 state is necessary. Singlet fission also competes with fluorescence and other internal conversion processes, which exhibit decay rates on the order of a few picoseconds to femtoseconds.[215] Furthermore, triplet state detection is usually first attributed to intersystem crossing. However, a crucial distinction exists: ISC involves transitioning from one singlet to one triplet state, whereas SF involves converting one singlet state into two triplet states (section 2.3.3.2). Both triplets can undergo triplet-triplet annihilation, usually known as triplet fusion, by producing an excited state singlet, a ground state singlet, or even a triplet with higher energy.[214,221] These complicating factors make it challenging to identify and characterize SF.

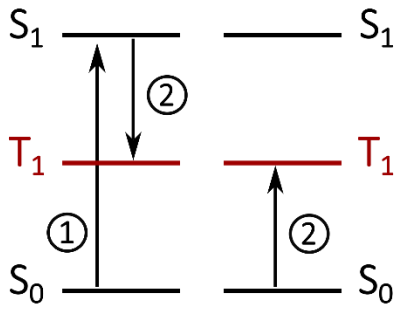

Figure 26: The process of singlet fission, SF, begins upon exciting the chromophore into its singlet state (1). Subsequently, SF produces a triplet on the excited molecule and another triplet on a neighboring molecule initially in the ground state (2). The process can be very fast because it is spin-allowed. The two triplets are initially coupled into an overall singlet, $^1(TT)$. This can be competitive with

[4] In the present work, it is proposed that the SF occurs from the excited state in singlet state S_1; however, some proposals in the literature suggest that in rubrene, SF can occur directly from S_2.[220]

all other deactivation processes that can occur in that excited singlet state. This is why the triplet yield can be up to 200%. (Adapted from [214])

Using SF in photovoltaic applications offers a method to surpass the Schockley-Queisser limit (SQL) for solar cell efficiency.[222,223] By converting triplet excitations into electron-hole pairs, SF materials can capture higher-energy photons to generate two electron-hole pairs per photon, enhancing cell efficiency. This process is combined with conventional photovoltaic materials that absorb lower-energy photons. The efficiency gain from SF depends on effectively harvesting charges from the triplet excitations to form charge carriers. Yet, challenges remain due to the potential of triplet excitons to act as traps, hindering charge separation. The theoretical model proposed by Hana and Nozick suggests that introducing a layer of SF material in front of a conventional material can significantly exceed the SQL, achieving an efficiency of approximately one-half compared to the traditional one-third limit. [224] However, the practical efficiency of SF-enhanced solar cells is contingent upon overcoming the limitations of charge harvesting from triplet excitons.[225–235]

5.2.1 Singlet Fission - Charge Transfer mediated

Charge transfer is a crucial mechanism that facilitates singlet fission in some materials. In this mechanism, the initial excited singlet state evolves through a charge-separated state before culminating in the formation of two triplet excitons. This intermediate charge-separated state can be understood as an electron being transferred from one part of a molecule or molecular system to another, creating a temporary positive and negative charge on different regions. Chapter 4, section 4.3.1.3, shows that when the system is formed from identical molecules, this charge separation breaks the orbital symmetry (SBCT) by disproportioning the electron distribution. As explained, tight molecular packing, as the slip-stacked n-alkyl SQ presented in this chapter, favors the CT. Such CT states can reduce the overall energy barrier for singlet fission, making the process more thermodynamically favorable and potentially faster. Moreover, the spatial separation of charges can also play a role in the directionality and dynamics of the triplet exciton formation. [216,217,236,237]

5.2.2 Detecting Singlet Fission

Considering the techniques used for this work, steady-state and transient absorption spectroscopy (Section 3.3), several experimental characteristics may need to be considered when detecting SF and differentiating the features from the above-mentioned competitive processes.

A good hint is the similarity of the recovery time of ground-state bleaching (GSB) to the decay time of the excited singlet state (SE) and triplet state formation. Frequently, the ascription of triplet formation to SF relies solely on its rapid rate, inferred from femtosecond transient absorption measurements. In the sub-100 fs scale, there is no time for ISC or fluorescence to happen.[231] This approach remains relatively unambiguous in the absence of heavy atoms, such as Cu, the case studied in Chapter 4, that, in contrast to the atoms constituting the molecules of this chapter, has a larger number of electrons leading to a stronger SOC, that allows for more efficient ISC with faster rates. It is important to consider that the time required for triplet state formation from typical intersystem crossing (ISC) seldom falls below approximately 10 ps and can often extend much further. Nonetheless, the duration for the formation of triplet states stemming from SF can extend up to 25 ps.[238]

Assigning transient absorption peaks accurately can be challenging. Employing excessive excitation density levels can lead to anomalies, manifesting as variations in fluorescence decay times. As reported in the case of tetracene, when the SF process is the preferred decay path for singlets, high concentrations of triplet excitons may be generated due to the longer lifetimes of triplet excitons compared to the singlet exciton lifetimes. Particularly at very intense illumination, the density of exciton in triplet states is considerably high and causes triplet-triplet annihilation.[239] Also, for example, an absorption previously believed to be T-T in pentacene was later identified as an artifact caused by heating.[240] Moreover, a former inconsistency, noting a 100 ps decay time for fluorescence compared to 10 ps for stimulated emission, was resolved when excitation densities were reduced below 2×10^{17} cm^{-3}. At this threshold, the interference from exciton-exciton annihilation was mitigated.

In transient absorption spectra, SF can be identified by correlating the rise of the triplet ESA with the decay of the singlet ESA, a technique also employed for ISC detection in CuPc. However, this chapter focuses on molecules with light atoms, characterized by weaker SOC than heavy atoms such as Cu. This reduced SOC means that in light-atom systems, ISC is generally less efficient and slower due to diminished interaction between singlet and triplet spin states. In contrast, heavy-atom systems like CuPc benefit from stronger SOC, which facilitates faster and more efficient transitions between singlet and triplet states. Therefore, the correlation observed here is more indicative of SF, given the inherently slower and less efficient ISC in the present light-atom-based systems of squaraines. A GSB that lives longer than nanoseconds with an ESA and phosphorescence in the range of µseconds has shown SF in olygoenes.[214,215,240–245]

5.3 Experimental: Anilino Squaraines

Anilino squaraines (SQ) are small molecule chromophores characterized by a rigid, linear, symmetrical donor-acceptor-donor molecular backbone. The structure comprises two anilino rings connected to a central squarylium ring by π-conjugated bridges. This arrangement gives rise to two degenerate, resonant zwitterionic configurations. In these configurations, an anilino nitrogen atom donates an electron pair to an oxygen atom of the squaric acid moiety, thereby generating an asymmetric charge distribution across the molecule. Consequently, the molecule exhibits a non-zero quadrupolar moment, enabling it to interact with electric fields despite being overall charge-neutral. [246,247] This quadrupolar character produces interesting photophysical responses, such as the non-Kasha behavior with a red-shifted absorption in the H-aggregate type.[248]

In 1965, the group of Treibs reported the first synthesis of squaraine dyes.[249] They are particularly intriguing dyes due to their panchromatic absorption range, which extends from the green to the near-infrared spectrum. This extensive absorption profile renders them an ideal material for applications in organic photovoltaics, but also for fluorescence bioimaging and photopolymerization applications.[250,251]

The SQ examined in this chapter are anilino squaraines in the solid state deposited as thin films on quartz substrates (Figure 27). First, SQIB is a model anilino SQ with branched alkyl side chains suitable for solution processing that, as well as iPSQ (Figure 27, nr.2), is not annealed and is in an **amorphous** state, i.e., unoriented molecules with different dipole-dipole interactions. While these SQs with branched alkyl chains are predominantly amorphous, indicating a lack of overall molecular orientation, they exhibit a tendency to partially organize their molecules under certain conditions. This partial organization can lead to the formation of localized regions with a distinct birefringent texture, as observed by the collaborator Prof. Manuela Schiek, who prepared the samples for this study. Such regions display a degree of localized molecular ordering that does not alter the general amorphous state of the material.

Four additional derivatives are shown in Figure 27, which are n-alkyl anilino SQ derivatives with variable alkyl chain: C_nH_{2n+1}. These are nBSQ,[5] nPSQ, nOSQ and nDSQ with four, five, eight and ten carbon length chains, respectively. They are annealed at 120 °C to yield 25 nm thin films of **slip-stacked** crystals with short intermolecular distances in the range of ~3.5 Å, the exact distance varying with respect to the alkyl chain.[252–260]

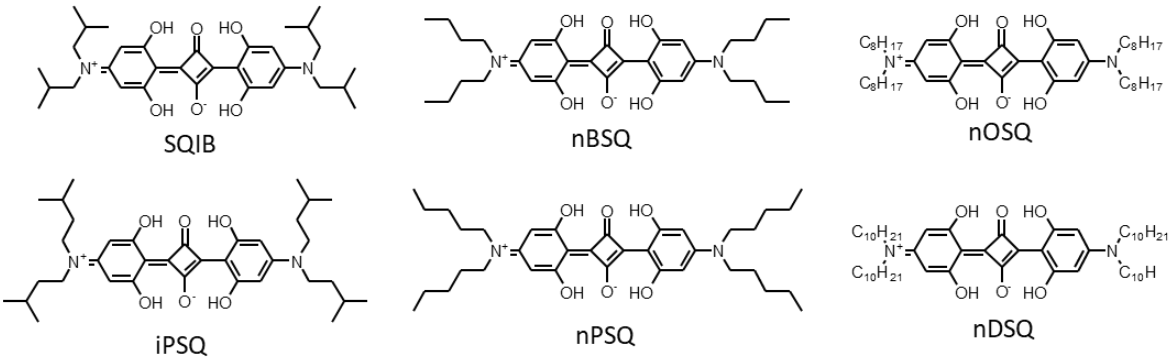

Figure 27: Squaraines under study. Amorphous: SQIB and iPSQ. Slip-stacked crystals of n-alkyl SQ with various intermolecular distances with respect to the variable alkyl chain.

[5] SQIB: (2,4-bis[4-(N,N-diisobutylamino)-2,6-dihydroxyphenyl]squaraine)
nBSQ: (2,4-bis[4-(N,N-dibutylamino)-2,6-dihydroxyphenyl] squaraine)

5.4 Results and Discussion

5.4.1 Squaraines in Solution: Photophysics of the Monomeric Form

To understand the ultrafast processes occurring in the monomer form of SQIB and nBSQ (in chloroform solution), transient absorption spectra at an excitation wavelength of λex = 650 nm have been measured.

TA with short-range delay times have been conducted using Helios (section 3.3.3). Figure 28 shows TA spectra at selected time fs to ns-scale delays for two different excitation fluences, 50 nJ and 100 nJ per pulse, covering the spectral range of 480-900nm.

TA spectra in the nanosecond timescale, measured using a long-range delay set-up, are shown in Figure 29 a-b, covering the spectral range of 380-880 nm. The **steady-state absorption** of SQIB and nBSQ in chloroform shows the typical profile of squaraine monomers (Figure 29 a-b, shaded orange for SQIB and blue for nBSQ). These spectra show an intense sharp absorption peak at 650nm, attributed to a 0-0 transition, and a weak shoulder at 600 nm, attributed to vibrational fine structures, the 0-1 transition (Frank-Condon Principle 2.3.1),[261] as well as a broad band of considerably low absorption from 400 to 500 nm. Literature reports the same absorption profile for other derivatives in various solvents.[262,263] Specifically, Hestand et al. report these absorption features in simulation and measurement of $DBSQ(OH)_2$ in 50:50 $DMSO/H_2O$,[35] as well as Zablocki with Schiek for nOSQ-and nDSQ- stock solutions in chloroform and diluted with $MeCN/ H_2O$.[260]

In both ranges and for both molecules, the **ground state bleach** (GSB) can be seen in the negative features at 600 nm and 650 nm, which match the peaks from the steady-state absorption spectrum. A deeper look at the recovery of the GSB shows that it is slightly red-shifted with respect to the steady-state absorption peak. As seen in the ultrafast range (Figure 28) this shift occurs progressively between the time constants of ~ 500 fs, ~ 1 ps, and ~ 10 ps. In the literature, this shift is attributed to rapid solvent and internal reorganization.[264]

This is further elucidated by the enhancement of the **stimulated emission** (SE) between 690 and 730 nm within the 0.1-10 ps timeframe, stemming from the dynamic Stokes shift. The designation of SE is grounded in the observed fluorescence spectrum from the literature, which substantially overlaps with the absorption spectrum, a typical characteristic of all dilute solution samples of squaraines. Fluorescence measurements in several solvents at room temperature show a band around 700 nm, which is most likely attributed to the emission from S_1 due to Kasha's rule. Therefore, the negative contribution between 700 nm and 720 nm is assigned to a vibronic band in the SE.[261,265]

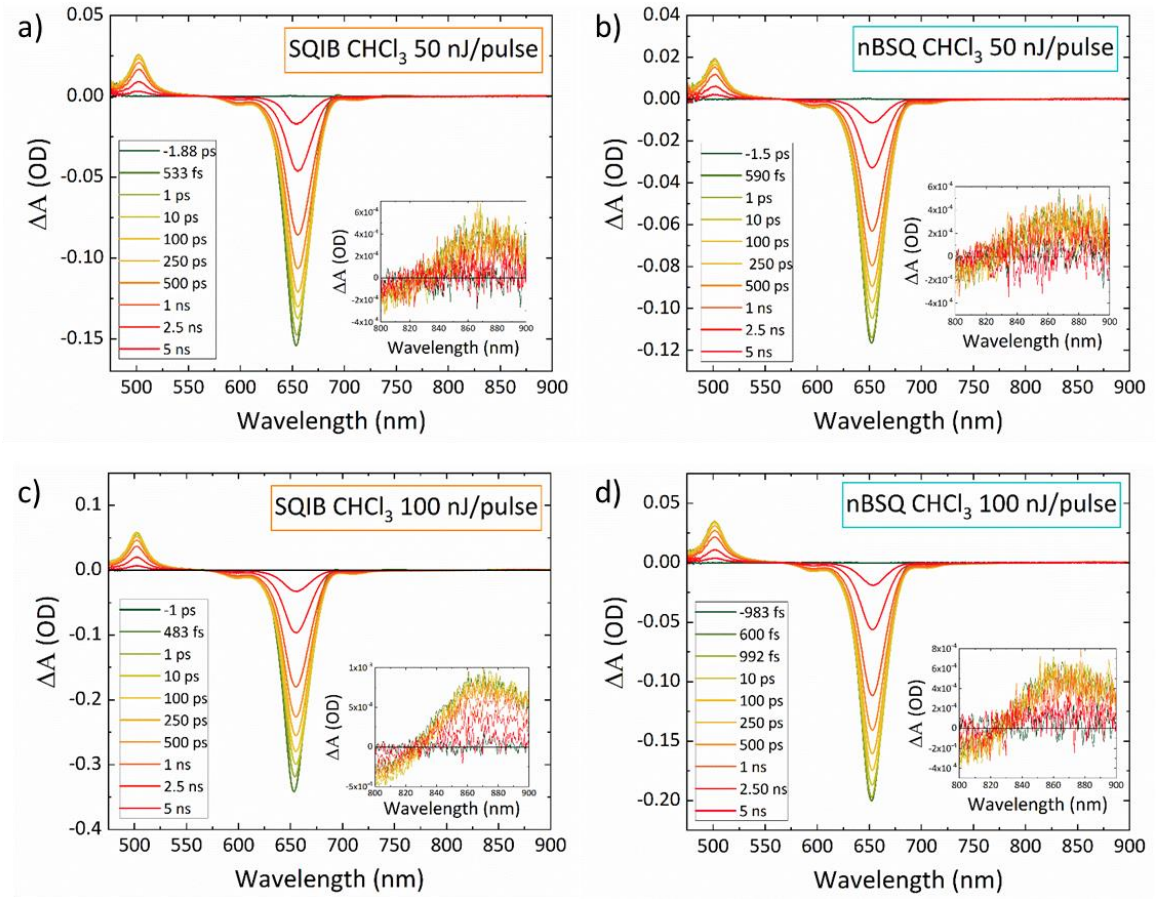

Figure 28: Transient absorption spectra at selected time fs to ns-scale delays of SQIB (a and c) and nBSQ (b and d) in chloroform for two different excitation fluences: a-b at 50 nJ/pulse and c-d at 100 nJ/pulse. Insets show the detail of TAS at 875 nm.

The positive contributions show the **excited state absorption** (ESA). Three prominent ESA peaks between short and long ranges can be seen: 440 nm, 500 nm (Figure 29), and 875 nm (Figure 28). The ESA at 440 and 500 nm arises from an excited singlet state.

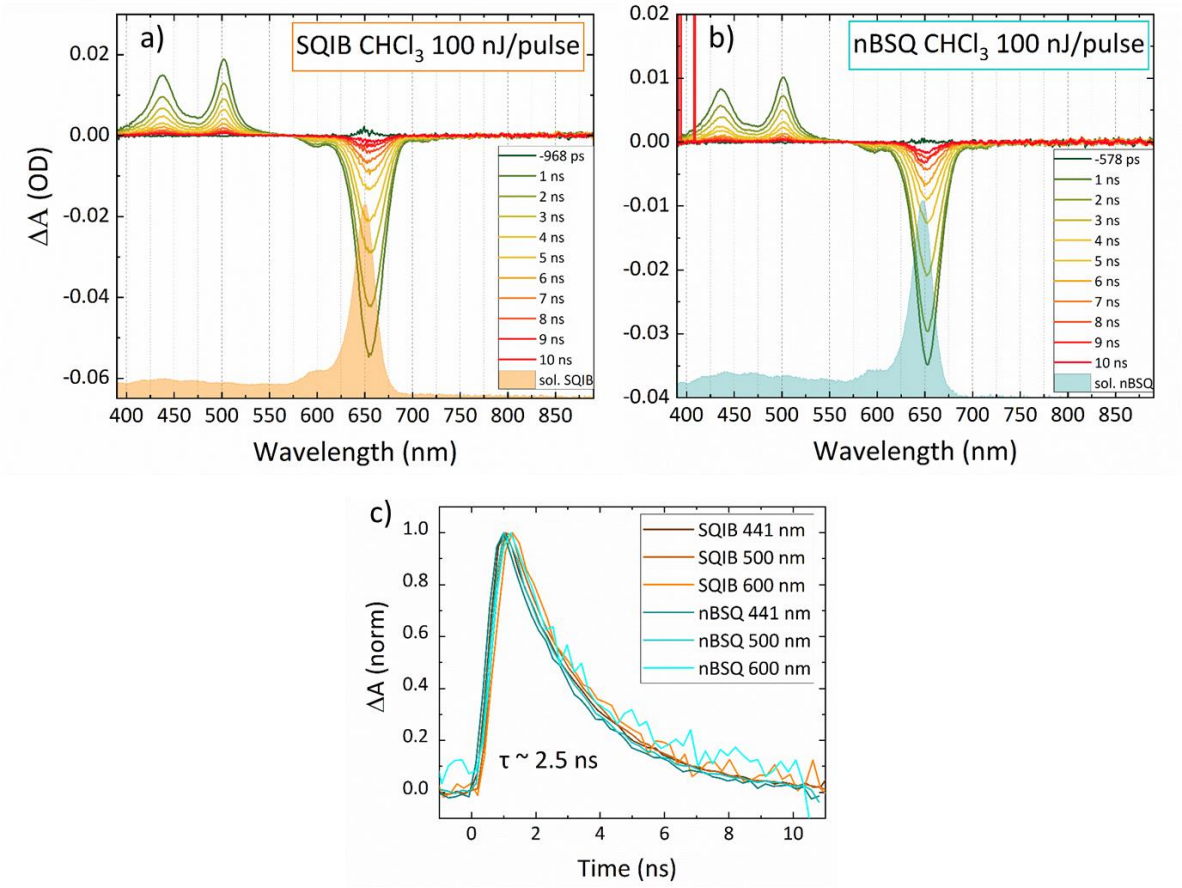

Figure 29: a-b) Transient absorption spectra at selected time ns-scale delays of SQIB and nBSQ in chloroform solution photoexcited at λ_{ex} = 650 nm. The steady-state absorption profile of SQIB (orange) and nBSQ (blue) in chloroform is overlaid for comparison. Its position in the graphic has been appropriately rearranged for comparison purposes. c) The kinetics of relevant features ESA and GSB and decay time are the same for all.

Figure 29c shows the **ESA and GSB decay dynamics** for SQIB and nBSQ. For both samples, the rate of the monoexponential decay for both ESA peaks matches the recovery of the GSB. This fits to a monoexponential decay time of **τ**= 2.5 ns. This is consistent with these spectra demonstrating excitation to and decay from S_1, in agreement with the literature.[264] Figure 30 shows kinetics on a linear time scale of ps for the relevant features: ESA at 500 nm, GSB at 600 nm, SE at 715 nm and ESA at 875 nm. In this time scale, the dynamics show a similar decay time, τ ~ 2.2 ns, further supporting excitation to and decay from S_1. As Figure 30 shows, at 875nm, the spectra are noisy, but the ESA there has dynamics that fit to **τ** ~3 ns.

In conclusion, the monoexponential decays for both SQIB and nBSQ, their similar decay rates, and, generally, their same transient absorption features indicate that in the monomeric form, the alkyl chain does not have any effect on the electronic and vibronic transitions. In contrast with what has been presented in the previous chapter, there is no intramolecular intersystem crossing in the SQ monomers.

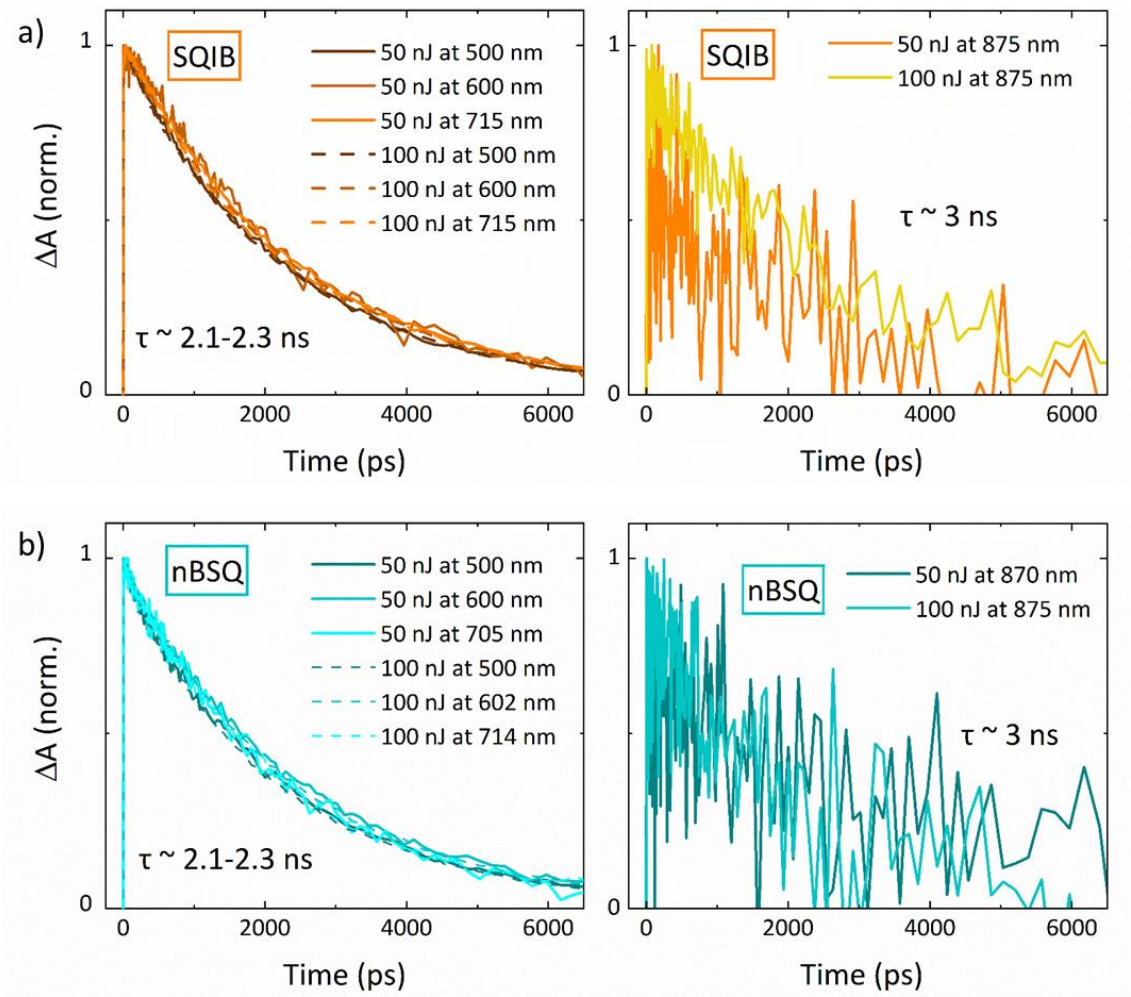

Figure 30: Normalized kinetics at ESA, GSB, and SE features for two different excitation fluences. a) for SQIB in chloroform, b) for nBSQ in chloroform.

5.4.2 Squaraines in Films: Photophysics of the Aggregated Form

5.4.2.1 Steady-state Absorption of Aggregates

The steady-state absorption spectra in solution are consistent for each species in both the literature and our data. However, the absorption spectra of thin films differ for each species, as Figure 31 shows. This supports the hypothesis that the length of the alkyl chain affects the aggregate properties and, consequently, the photophysical response to excitation.

Squaraines with Amorphous Morphology on Thin Films:

Figure 31a shows normalized steady-state absorption spectra of the SQ thin films and evidences the aggregation effect. The solid form of SQIB, which is amorphously distributed on the substrate, shows a broad, blue-shifted single peak. For comparison, iPSQ, also amorphous, presents peak splitting. Such peak splitting is also observed in the crystalline slip-stacked form of nBSQ. Figure 31b compares the two peaks-profile of all four slip-stacked anilino SQ to evaluate the effect of the chain length. The monomeric absorption of SQIB and nBSQ is given as a reference.

In the spectrum represented in orange, **SQIB** exhibits a single broad absorption band with a maximum of around 630 nm and an accompanying shoulder at approximately 530 nm. Both features are blue-shifted relative to the monomer absorption. The shoulder at 660 nm is attributed to the amorphous arrangement of the molecules within the film.

However, the spectrum colored in yellow of **iPSQ** shows a splitting of absorption bands. A blue-shifted, broad band centered at 570 nm, with a shoulder approximately at 520 nm, can be ascribed to an H-like aggregate behavior, the absorption increment in the peak assigned to the vibronic transition 0-1 with respect to the absorption of the electronic transition 0-0 indicates the formation of H-aggregates (section 2.4.2.3). The most pronounced absorption appears at 775 nm, significantly red-shifted (~100 nm) from the monomer absorption. This pronounced shift suggests an intermolecular charge transfer state (CT).[264] Also, in iPSQ, a shoulder at 660 nm can be seen.

The random orientation of the amorphous films results in variable intermolecular distances, seen as an irregular absorption peak distribution. It can be inferred that the close proximity of individual molecules in the solid state facilitates diverse intermolecular interactions, resulting in a split of energy levels, more evident in iPSQ than in SQIB, when compared to the energy levels of the isolated molecules in solution.

In the existing literature, various approaches have been adopted to elucidate the energy level splitting and shift observed in squaraines with branched alkyl chains, predominantly focusing on SQIB with no mention of iPSQ. These explanations often invoke long-range Coulomb interactions, which can lead to exciton splitting and delocalized excitons along the aggregate. Depending on the orientation of the transition dipole moments, i.e., the angle between molecular planes, as detailed in section 2.4.2.2, a Davydov splitting may manifest (section 2.4.2.4),[266] or a mix of states with brand new peaks, section 2.4.3, due to a concurrent presence of both H- and J-aggregates, typical from herringbone packing geometry.[267] Some research groups have also considered the short-range intermolecular charge transfer interaction delocalized along the slip-stacked structure when the molecules are closely packed. In a slip-stacked packing scheme, the CT is facilitated by the short distance between the donor group of one molecule and the acceptor group of its neighbor. This occurs when an electron is transferred from the donor of one molecule to the acceptor of the adjacent one. This is frequently ascribed as the lowest energy band in the spectra, coincident with the J-aggregate band.[35,37,263,252,268,253] Sections 2.4.2.5 and 2.4.3. These interactions are further explored in slip-stacked n-alkyl SQ presented in Figure 31b. To simplify, the signature at the shorter wavelength is labeled H-band, and the signature at the longer wavelength is labeled CT-band.

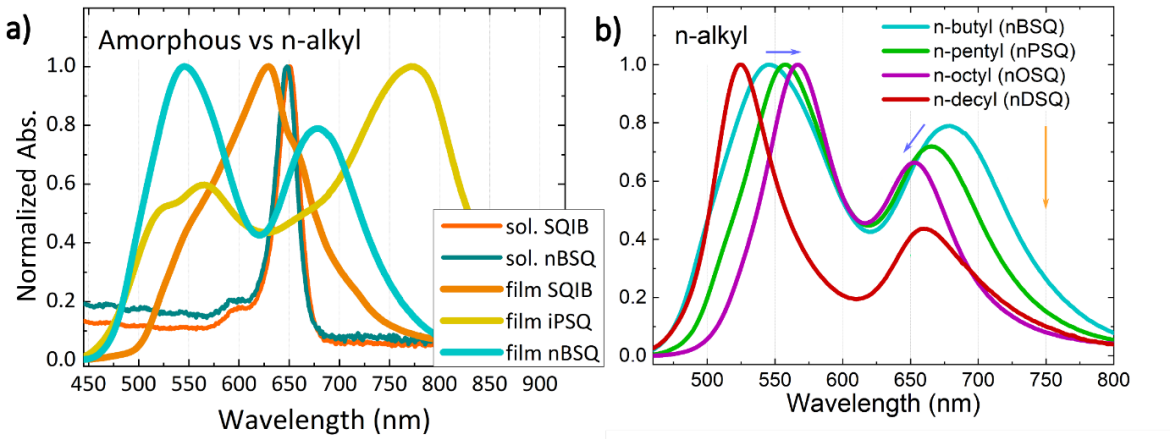

Figure 31: Normalized steady-state absorption spectra of all the species of this study. a) Amorphous SQIB (orange) and iPSQ (yellow) in a thin film in comparison with the absorption of n-butyl SQ (cyan) together with the absorption of the monomers SQIB (dark orange) and nBSQ (dark cyan). b) n-alkyl squaraines: nBSQ (cyan), n-pentyl (green), n-octyl (magenta), and n-decyl (red). The orange arrow indicates the trend ratio of the two maxima. Green arrows show the trend of the full width at half maximum (FWHM) for each maximum. Blue arrows indicate the position trend of each maximum.

Squaraines in Slip-Stacked Crystallization:

Figure 31b shows the steady-state absorption spectrum measured for all n-alkyl squaraines slip-stacked aggregates used in this study: n-butyl (cyan), n-pentyl (green), n-octyl (magenta) and n-decyl (red). These exhibit the distinct two-peaks character, typically observed in such systems:[260] One peak is blue-shifted with a pronounced absorption, usually assigned to an H-like aggregate, while the second peak shows a minor red shift compared to the monomeric SQ absorbance in solution. Notably, this broad, red-shifted peak does not align with SQ monomers or the classical sharp and well-defined J-aggregate signature. Thus, the spectral characteristics of these aniline-derived SQ aggregates cannot be solely attributed to H- or J-aggregate behavior. Instead, the absorption peak splitting shows an H aggregate behavior with significant CT character due to short-range interactions.[35] Note that the division of the excited state is not consistent with Davydov splitting, a conclusion supported by the fact that only one molecule with identical properties at each lattice point exists in the crystallographic unit cell.[19,260]

The characteristic peak splitting is strongly dependent on the stacking distance:

In both Figure 31 a) and b), the spectrum of nBSQ serves as a reference due to its well-characterized stacking and its possession of the shortest alkyl chain among the studied compounds. It exhibits two distinct maxima at 550 and 660 nm, with an accompanying shoulder approximately at 500 nm. Contrasting with the band splitting observed in iPSQ, the H- band in nBSQ is significantly blue-shifted by roughly 100 nm. Meanwhile, the CT-band displays a modest redshift of 10 nm with respect to the monomer absorption. In Figure 31b, the orange arrow highlights the trend in the ratio of the two maxima. Relative to the H-band, the ratio of H/CT absorption increases as the alkyl chain lengthens, which aligns with simulations conducted by other research groups.[255] Blue arrows pinpoint the positional trend of each maximum. For the samples examined, the two bands converge as the chains elongate. However, consistent with the simulations above, the dominant peak of nDSQ exhibits an even more significant blue shift. Regarding the trend of each band: As the chain length increases, the H-band narrows for all the n-alkyl molecules, correlating with increasing oscillator strength.[99] The same trend is observed for the CT- band, though the nDSQ band is broader than that of the nPSQ.

In conclusion, the packing motif is the same, but the intermolecular distance increases with a longer alkyl chain, affecting the interactions within the aggregate. Specifically, as the chain lengthens, there is an enhanced H-aggregate character, a diminished CT strength, and a reduced energy difference between the CT state and the monomer's excited state energy. This can be attributed to the increased distance between the nitrogen (donor) and squarylium (acceptor) moieties on adjacent molecules. These findings align with the literature.[36,260,263,269] For CT-band characterization, the amorphous SQIB (no CT) and iPSQ (strongest CT) will be used as reference. The fluorescence shape and intensity under excitation in 550 nm (possibly H-band) and 650 nm (possibly CT-band) should corroborate the assignment to an H and CT–-band.

5.4.2.2 Fluorescence of Thin Films

Squaraine dyes typically exhibit pronounced fluorescence characterized by a high quantum yield, enhancing their potential for applications in biomedicine and

optoelectronic devices.[270] However, if singlet fission were occurring, fluorescence quenching would occur because the process shifts the excited state population from one molecule in the singlet state to two molecules in the triplet state. As mentioned and used to interpret the measurements in the earlier discussion regarding the monomer photophysics, literature shows that the monomers display fluorescence with a Stokes shift of a few nanometers. [267,271–273] The present section explores the fluorescence of all molecules in thin films to find if there is any quenching due to the stacking.

Figure 32 shows the steady-state fluorescence of **n-alkyl derivatives** in thin films under excitation of λ_{ex} = 550 nm and λ_{ex} = 650 nm (dashed lines) using the technique explained in section 3.2.2. The highest fluorescence intensity is carried by n-octyl (magenta). Regarding the excitation to the H- band, λ_{ex} = 550 nm is 3.5 times brighter than n-pentyl (green) and 2.6 times brighter than n-butyl (cyan). However, n-decyl (red) has almost no fluorescence. All derivatives have a maximum of around 832 nm. There is no shift when the excitation is to the CT- band, λ_{ex} = 650 nm. However, there is a fluorescence quenching of about 80% for nBSQ, 47% for nPSQ, 66% for nOSQ, and 45% for nDSQ.

The fluorescence originating from the aggregates, which emerges from an energy state lower than that of individual molecules, confirms the impact of aggregation. The characteristics of the fluorescence depend on the alkyl chain length. For nBSQ, nPSQ, and nOSQ, the intensity increases with the length, and the CT-band fluorescence-quenching decreases with the length. The particular case of nDSQ does not fully fulfil this trend but is also singular in its steady-state absorption.

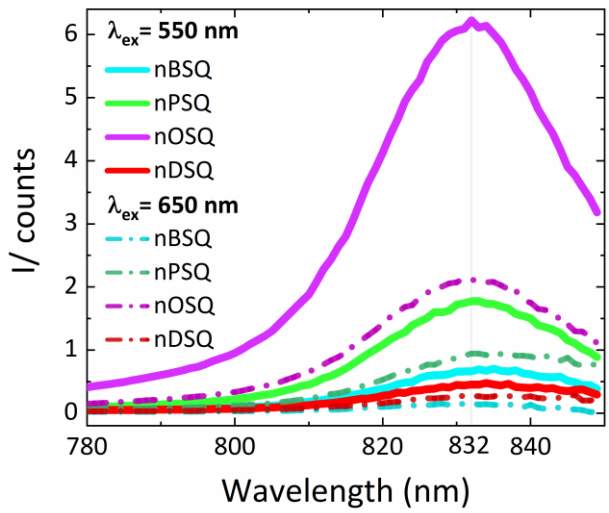

Figure 32: Steady-state fluorescence of n-alkyl derivatives under excitation of λ_{ex}= 550nm. Inset: normalized fluorescence spectra compared with the normalized fluorescence spectrum from nOSQ at λ_{ex}= 650nm (dark magenta).

Figure 33 shows normalized steady-state fluorescence spectra for SQIB (a) and iPSQ (b) in the amorphous state under excitation wavelengths λ_{ex}= 550 nm (high intensities) and 650 nm. Kasha´s rule is corroborated by all emission maxima occurring at 825 nm, irrespective of the excitation wavelength. When exciting in the CT band, there is no considerable fluorescence quenching for SQIB but about 70% for **iPSQ**. The fluorescence spectrum of **SQIB** features additional peaks at 740 nm and 760 nm, exhibiting notably lower intensities than the main peak. These peaks also observed in fluorescence measurements conducted by Prof. Schiek, are absent in other molecules recorded under identical conditions. Therefore, the possibility of these peaks resulting from scattered light from the excitation signal is ruled out. However, low annealing temperature-dependent photoluminescence experiments from Schieck´s group show a very similar peak distribution to the one in the present chapter. They measured a fluorescence peak at 800 nm assigned to a 0-1 transition within H-type aggregates because transitions to the electronic ground state can occur when vibrational quanta provide the necessary momentum, resulting in a red shift of the band relative to transitions without vibrational involvement. In their study, a shoulder at 725 nm emerges with increasing annealing temperature. It is assigned to the dipole-forbidden 0–0 transitions in H-aggregates, which is possible due to the thermal fluctuations that

disrupt the structural order of the aggregates, slightly loosening the dipole selection rules.[253]

In conclusion, the minor red-shift in the fluorescence maxima of n-alkyl relative to the amorphous SQ can be attributed to the reduction in the energy of the lowest excited state due to slip-stacked aggregation.[13,108,274] The energy level splitting observed in the absorption profile of iPSQ and the n-alkyl compounds (Figure 31), as well as the general fluorescence quenching when exciting in the CT band probes that in slip stacked SQ some processes are happening, and that the similar behavior of amorphous iPSQ is showing an aggregation effect, even when the iPSQ molecules stack in an unknown form on the substrate. This is in contrast with the case of SQIB, which is without energy levels split, and its fluorescence is less quenched than the others due simply to random aggregation leading to annihilation.

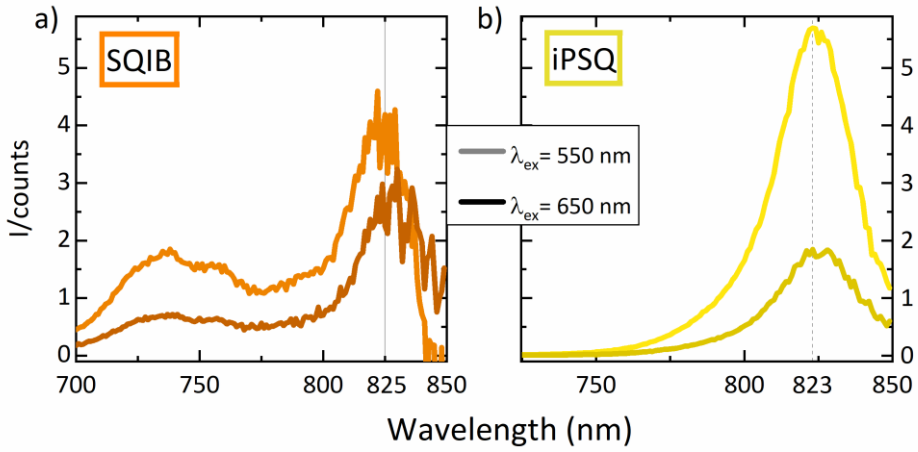

Figure 33: Normalized steady-state fluorescence for a) SQIB (orange) and b) iPSQ (yellow) under excitation wavelengths of λ_{ex}= 550 nm (bright colors) and 650 nm (dark colors). In c) raw data of nOSQ (magenta) and nPSQ (green) in comparison with amorphous SQIB and iPSQ under λ_{ex}= 550 nm.

If these processes (that suppress fluorescence) are stacking-dependent, are a mere intermolecular charge shift from one molecule to a neighbor, breaking the overall symmetric distribution of charges within the chromophore (SBCT, as explained in section 4.3.1.3), or are an excited state shift from one molecule to a neighbor (SF) is something that will be better elucidated using TA spectroscopy in the next section.

5.4.2.3 Transient Absorption Spectroscopy

This section details the ultrafast dynamics of squaraines in amorphous state and slip-stacking in thin films, representing measurements not previously reported. The six SQ have been probed with a white-light continuum in the uv-vis range and excited with a pump beam at λ_{ex}= 550 nm and 650 nm.

5.4.2.3.1 Effect of intermolecular interactions in the photophysics of SQ

To understand the effect of the intermolecular interactions on the photophysics of the n-SQ series, first, a study of the photophysics in both extreme examples (SQIB: No split and iPSQ: strong interactions) is shown. Figure 34 presents contour plots illustrating transient absorption spectra for amorphous squaraines. The plots integrate three variables: decay time in ps across the full range of the setup versus wavelength, with colors corresponding to differences in absorption intensity of features (ΔA). Yellow-to-blue hues represent negative features (GSB and SE), while red shades denote positive ones (ESA). The evolution-associated decay spectra (EADS), derived from a tri-compartmental global analysis (section 3.4.2), are beneath each contour plot.

SQIB in amorphous form: example of no intermolecular interactions

The transient absorption spectra of amorphous **SQIB** with λ_{ex} = 550 nm, as seen in Figure 34b, show a broad negative signal between 500-800 nm, coincident with the steady-state absorption signal overlapped with the steady-state fluorescence (marked in orange on the contour plots). This feature, assigned to a mixture of GSB and SE, predominantly decays within ~30 ps. This recovery time aligns with that of the ESA, seen between 450-550 nm, which becomes more discernible in the UV-vis spectrum region (Figure 34a and the overlap of uv with the visible area in Appendix 6.2.1, Figure 45). The 420 and 470 nm ESA peaks are blue-shifted (~30 nm) relative to the solution ESA (Figure 29). The third decay rate is labeled as non-decaying (nd) because it exceeds the system's resolution threshold (7.5 ns). Similar overlapping features with comparable decay rates are evident for SQIB under λ_{ex} = 650 nm, Figure 34c, suggesting

the photophysics of SQIB remains unaffected by changes in excitation wavelength. The data were cropped until 650 to avoid the excitation signal scatter contribution.

iPSQ: strong intermolecular interactions

Figure 34d displays the contour plot for **iPSQ** under λ_{ex} = 550 nm, steady-state absorption, and fluorescence highlighted by yellow lines. The respective EADS from the global analysis are in the graphic below. The ESA starts below 500 nm and lasts until 650 nm, overlapping with the GSB contribution. The complete GSB recovery coincides with that of the ESA, occurring within 33 ps. However, this recovery process experiences significant interference due to the subsequent emergence of a non-decaying ESA at 675 nm. This positive signal pointed with a blue arrow, appears after 100 ps, does not decay within the temporal measurement window of the setup, and blends with the also persistent SE at 800 nm, consistent with the pronounced fluorescence signal of this molecule. This could be the ESA of a newly developed photoproduct, such as a triplet state from SF. But it could also be due to local heating on the film. Further measurements, such as the excitation dependence done on CuPc (Figure 24), are needed to elucidate this further.[275]

The oscillation pattern seen in this molecule does not appear in SQIB; however, it is seen in n-alkyl SQ (next section), as well as a similar red shift in the ESA, which is alkyl chain length-dependent. All of this demonstrates the effect of the intermolecular interactions.

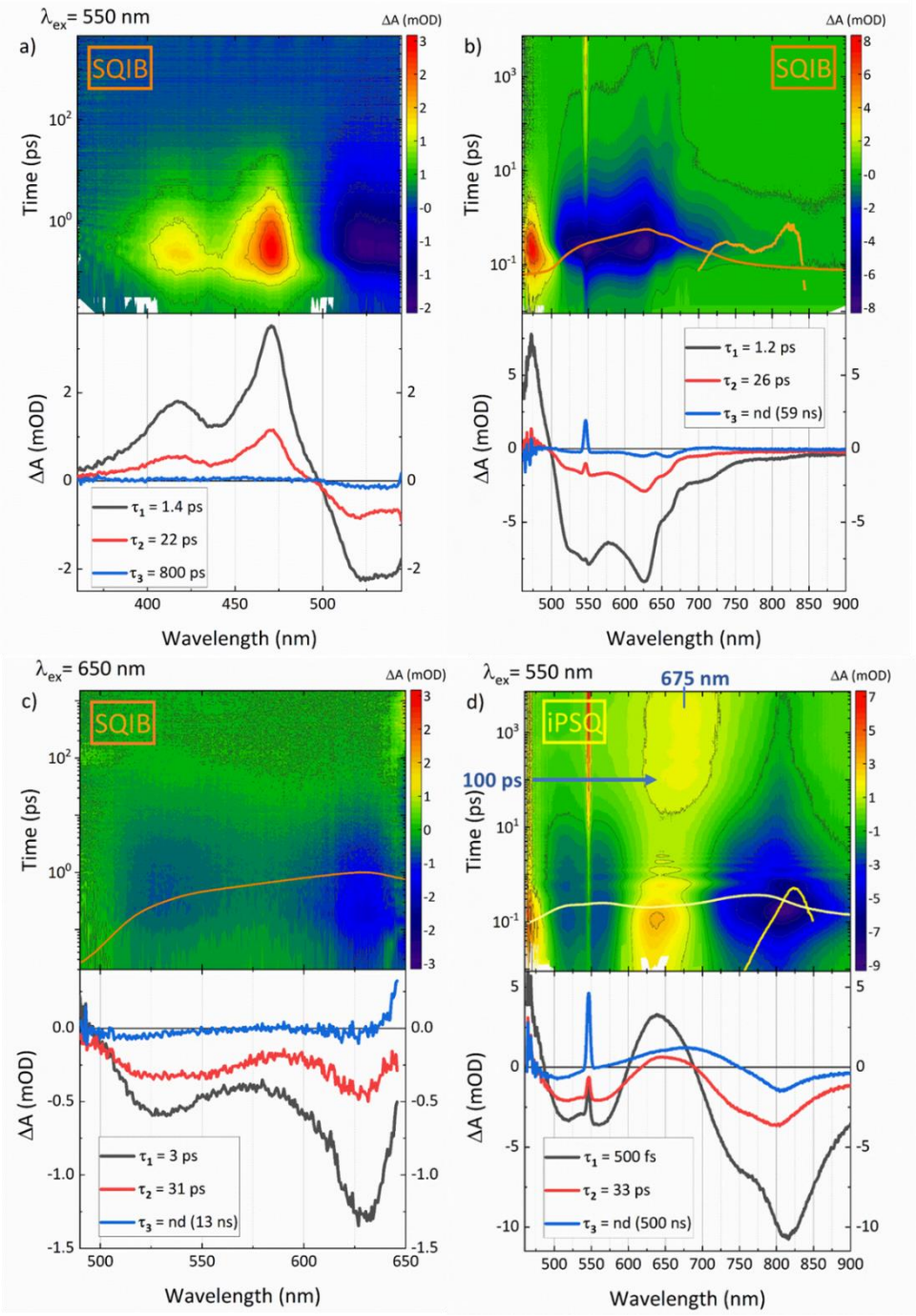

Figure 34: TAS of amorphous SQIB under λ_{ex}= 550 nm in a) UV-vis and b) vis range. In c) SQIB under λ_{ex}= 650 nm, cropped to avoid excitation signal scatter. In d) iPSQ under λ_{ex}= 550 nm. ESA features are in a reddish color scale, GSB in blue. Solid lines represent steady-state spectra, appropriately scaled for comparison purposes. Below, evolution-associated decay spectra in three compartmental global analyses with decay rates are shown.

5.4.2.3.2 TAS in n-alkyl Squaraines

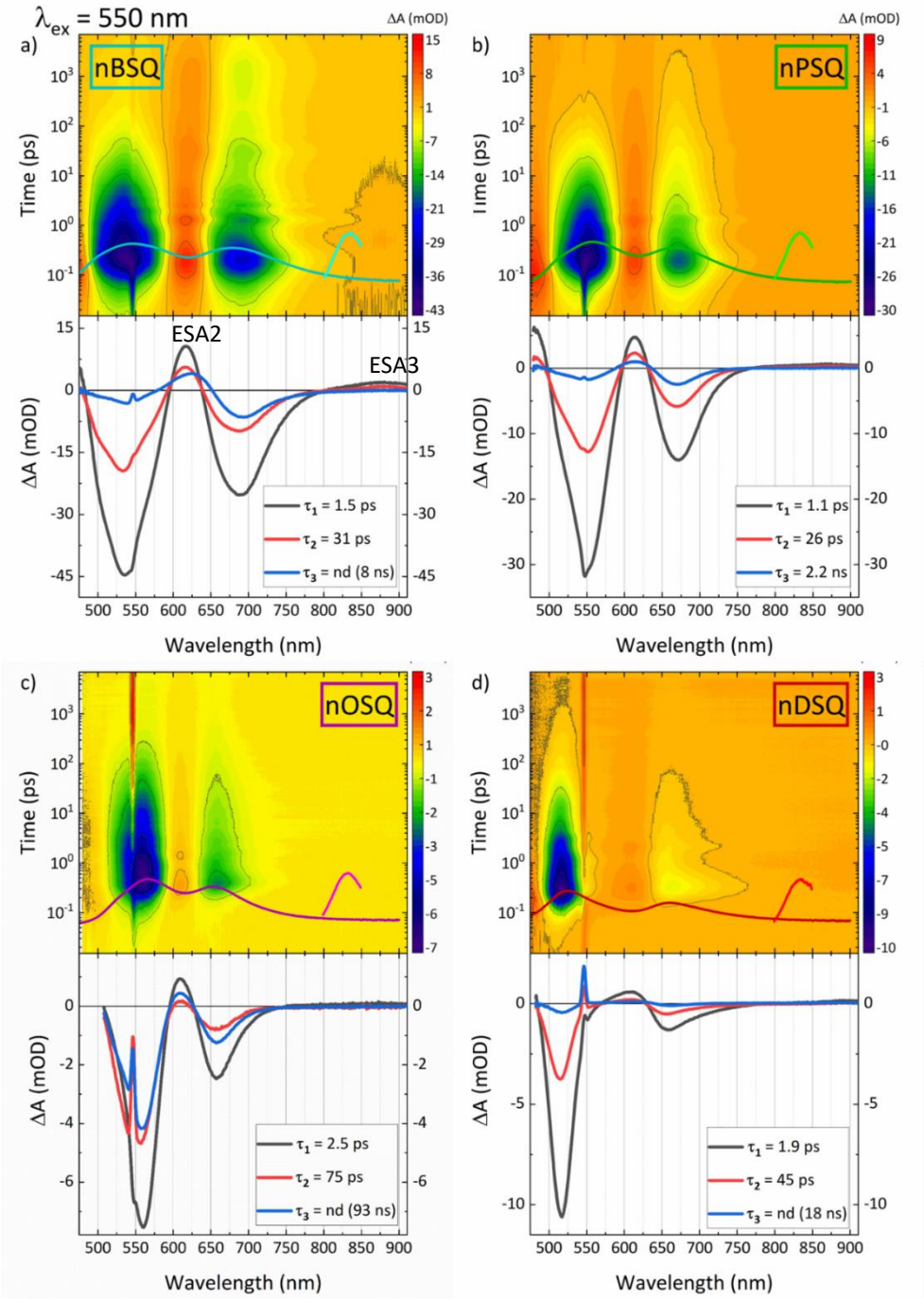

Figure 35: TAS of n-alkyl SQ: a) n-butyl SQ, b) n-pentyl SQ, c) n-octyl SQ, d) n-decyl SQ. ESA features are on a reddish scale, and GSB is on a blue scale. Steady-state absorption and fluorescence as solid lines, appropriately scaled for comparison purposes. Below, EADs spectra in three compartmental global analysis with decay rates.

Figure 35 depicts contour plots representing transient absorption spectra for **n-alkyl** derivatives following excitation at λ_{ex}= 550 nm. The color scale demonstrates the signal intensity. The excitation density is constant for all samples (~ $5 \cdot 10^{18}$/cm³, see Table 3). Overlaying the contour plots are the steady-state absorption (as in Figure 31b) and the fluorescence (as in Figure 32) spectral lines. The relative EADS resulting from a three-compartmental global analysis are shown below.

Ground State Bleach (**GSB**):

For all squaraine variants, the traces from steady-state absorption closely align with the relative minima, represented in blue shades, on the TA contour plots assigned to the GSB. Here, the trends observed in the steady-state absorption (Figure 31b) become more pronounced. The GSB assigned to the H-band at 550 nm narrows for longer chains. Furthermore, the intensity of the GSB assigned to the CT-band decreases with increasing alkyl chain length, and its position blue shifts. This can also be seen here in both EADS1 and EADS2.

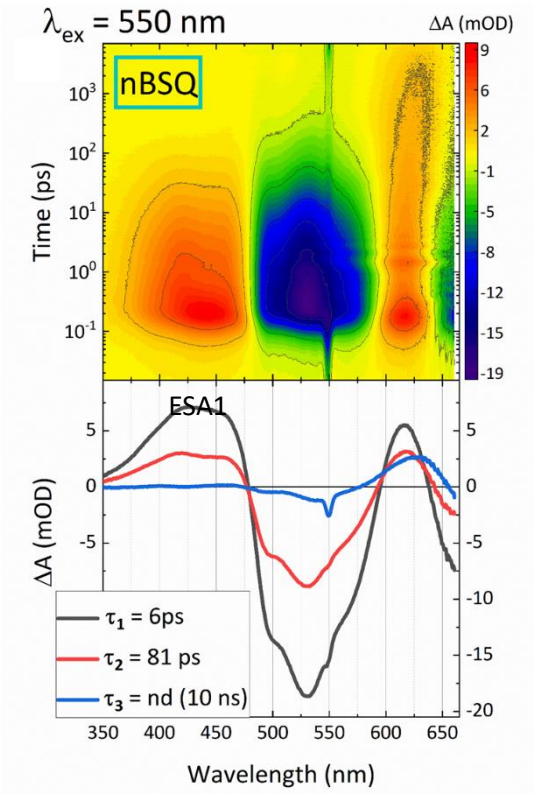

However, the two peaks also exhibit differential behaviors: the H-GSB decays more rapidly than the CT-GSB independently of the chain length. The nOSQ analysis is significantly influenced by the excitation scatter; thus, the behavior of its GSB around 550 nm is excluded from consideration. TA was also done in the UV range only for nBSQ, Figure 36.

Figure 36: Contour plot of TAS for nBSQ under λ_{ex}= 550 nm in uv-vis range. ESA features in reddish shades, GSB in blue. Below, EADs spectra in three compartmental global analysis with decay rates.

Excited state absorption (**ESA**):

There are three distinct ESA features: ESA1 around 450 nm, ESA2 near 620 nm, and ESA3 approximately at 875 nm.

ESA1 is observable in the uv-range measurements of Figure 36. As observed in the decay profile of the ESA of amorphous SQIB, it presents a broad feature with two peaks around 415 nm and 460 nm. Both peaks are blue-shifted relative to the ESA in a solution setting. This specific ESA1 completely decays within 80 ps, aligning with the GSB's recovery duration. This phenomenon is ascribed to excitation to and subsequent decay from states S_0 and S_1.

ESA2, which appears around 620 nm (at λ_{ex} = 550 nm), does not decay, irrespective of alkyl chain length, excitation wavelength, or density. As the EADS 3 shows, the ESA2 demonstrates a redshift, which is especially pronounced in nBSQ, but nPSQ and nOSQ do not present any visible shift, and the case of nDSQ is challenging to appreciate. This shift, albeit attenuated, parallels the behavior observed in iPSQ (easily seen in both yellow regions from Figure 34d). Such behavior could potentially be attributed to a SF, wherein T_1T_1 triplet states emerge around the 50 ps mark. However, this positive feature at 640 nm could also be attributed to a heating effect, and more experiments are needed for this evaluation.

ESA3, depicted in detail in Figure 37, although of low intensity, is observed in both nBSQ and nPSQ, with maxima starting at 0.5 ps, centered at 875 nm, similar to the solution phase (Figure 28). It remains undetected in nOSQ (not shown). Despite the low CT-band character of nDSQ, it shows an ESA3 red-shifted, at ~900 nm, slightly delayed, ~0.9 ps. Given the faintness of the signal, pursuing an analysis of ESA3 for nDSQ proves inconclusive.

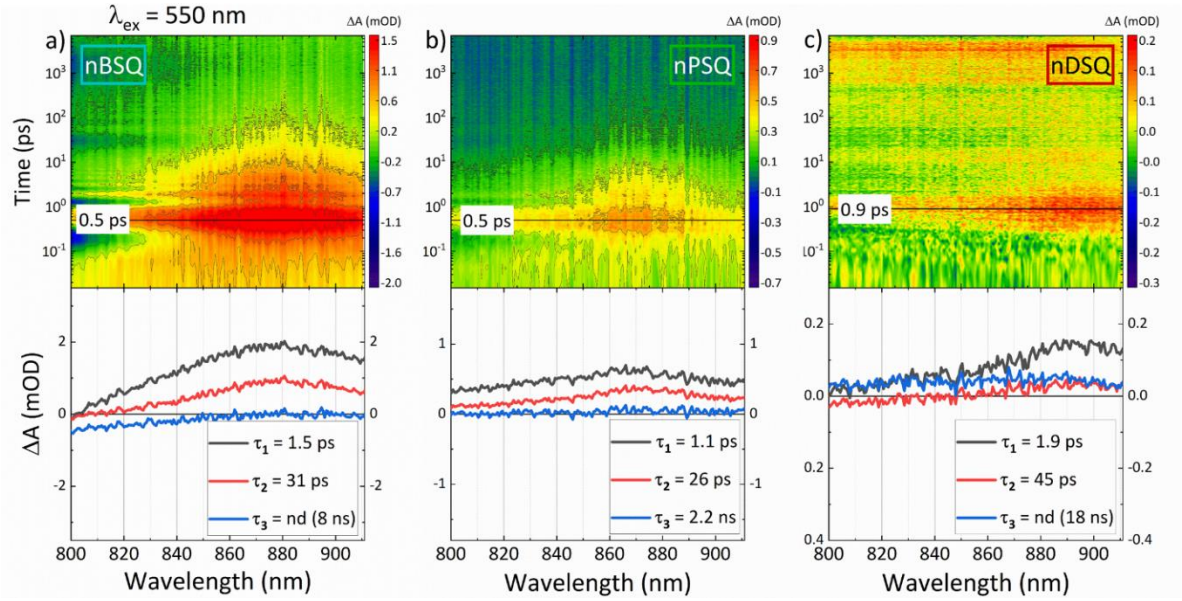

*Figure 37: Zoomed-in scale contour plots and EADS for a) nBSQ, b)nPSQ, and c) nDSQ under λex= 550 nm. The maximum intensity appears in 0.5 ps for nBSQ and nPSQ and 0.9 ps for nDSQ. This signal is the **ESA3**.*

Nonetheless, all instances of ESA3 share the following characteristics: they emerge approximately 400 fs delayed with respect to the singlet ESA1 and ESA2, evident in Figure 38 for nBSQ and consistent for both nPSQ and nDSQ. Also, all ESA3 invariably decay within ~100 ps. This aligns with findings from previously mentioned literature, where they assign a fs-delayed ESA and ps-decay rate to an excitation of the T_1 and transition to an unknown state T_N, suggesting its association with a SF process (Section 5.2.2). However, to fully assign this ESA to any triplet transition, it is necessary to know the triplet energy, for example, using Density Functional Theory calculations. At the present moment, this data is unknown; therefore, the interpretation of this feature remains as a delayed-fast decaying ESA with unknown multiplicity. It is also important to note that this process is CT mediated and exhibits dependency on alkyl chain length, with longer chains weakening CT processes.[263]

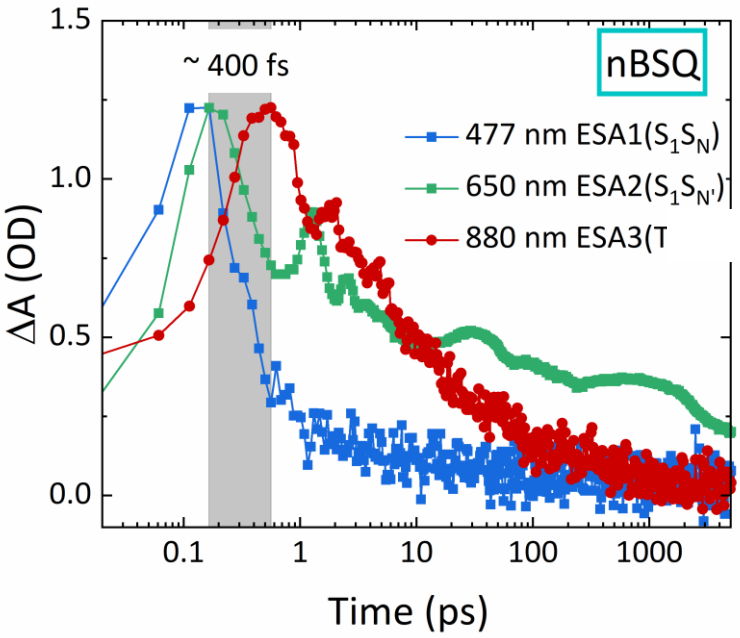

Figure 38: Kinetics of the ESA for nBSQ TA spectra under λ_{ex}= 550 nm. Both the excited state absorption to the singlet state, ESA1, transition S_1S_N, at 477 nm (blue), and ESA2, $S_1S_{N'}$ at 650 nm (green), reach their peak at ~165 fs. The ESA3 (red) emerges 400 fs later (indicated by the grey region) and decays at a rate slower than ESA1. As illustrated in the contour of Figure 35a, the ESA2 does not decay within the range of the Helios setup. The scatter plot reveals that all ESAs exhibit consistent data density within the grey region, thus eliminating the possibility that the delay observed in ESA3 is attributable to chirp correction.

Ground-State Bleach – Stimulated Emission (**SE**) overlap:

As illustrated in the blue region of Figure 35 and Figure 36, the second negative peak, centered around 680 nm, represents a **GSB**, coinciding with **SE**, leading to a red shift relative to steady-state absorption. Figure 39 presents the decay-associated difference spectra (DADS 3), normalized to the minimum of each GSB, for nBSQ under varied excitation conditions. For reference, the absorption profile of nBSQ is overlaid. Notably, the GSB does not fully decay to zero within 8 ns across any of the excitation wavelengths or densities. More importantly, the peak ratios (H-band/CT-band) in the GSB are opposite to the expectation from the steady-state absorption. This is because the GSB-SE overlap at 690 nm experiences a more prolonged decay or because another ESA

destructively interferes with the H-GSB. Considering that the fluorescence from the CT band is quenched, as seen in the previous section, this negative feature is still a GSB, which is a singlet state or CT state with a singlet nature. This ground state may be depopulated due to the population of a triplet excited state. The hypothesis for this slow decay is that If the negative GSB feature correlates with a triplet-excited state population, this would correspond with a slower recovery of the GSB, depending on the triplet-excited state lifetime.

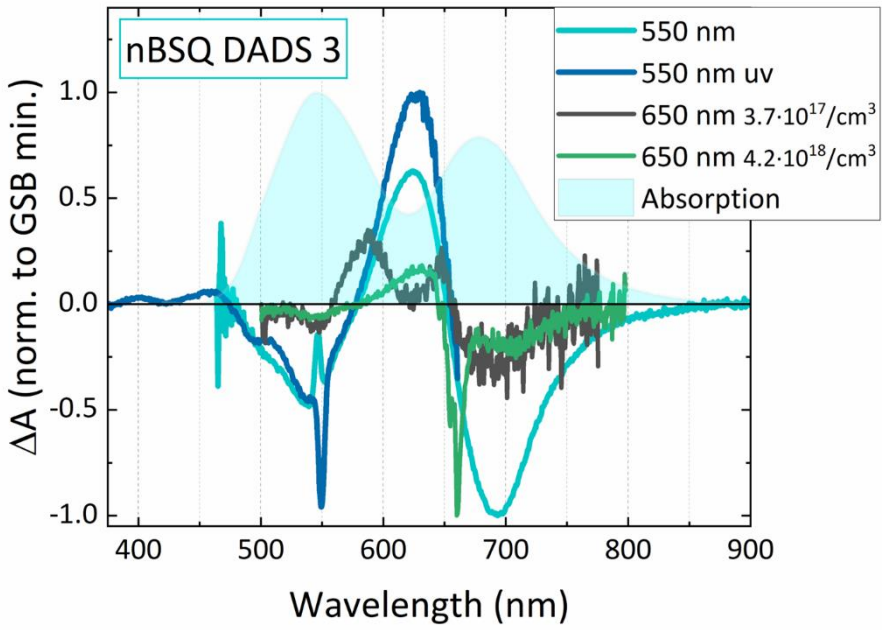

Figure 39: Normalized decay associated difference spectra for the last decay, DADS 3, of nBSQ at different excitations: cyan λ_{ex} = 550 nm, blue λ_{ex} = 550 nm (data in uv-vis region), black λ_{ex} = 650 nm with excitation density ρ_{ex}= 3.7·10^{17}/cm^3 and green λ_{ex} = 650 nm with excitation density ρ_{ex}= 4.2·10^{18}/cm^3. The light-overlapping shadow shows the steady-state absorption profile.

Power study λ_{ex}= 650 nm:

A **power study** was conducted with an excitation of 650 nm, adjusting the excitation density by controlling the pump beam size. The most notable results are displayed in Figure 40. The decay rates align with those observed during excitation at 550 nm. As illustrated in Figure 39, the trend for DADS 3 during excitation at 550 nm in the visible

(cyan) and UV (blue) regions, as well as during λ_{ex}= 650 nm (green) with a similar excitation density of the order of $\rho = 10^{18}/cm^3$, remains consistent: an incompletely recovered GSB at 550 nm and 680 nm and a pronounced ESA at 620 nm, showing a slight red shift.

At a lower excitation density, as seen in Figure 40b, the GSB at 550 nm appears to decay more rapidly, yet the peak at 500 nm persists. The EADS3 (blue) seems to show recovery, albeit not within the time frame of the employed setup. Of note in the EASD3 are two peaks that appear below and above the customary ESA2 at 620 nm. The sharp peak at ~650 nm is attributed to excitation scatter and is irrelevant. Having seen that with low excitation density, some features are more evident. The following section analyses this spectral region between 500 and 650 nm.

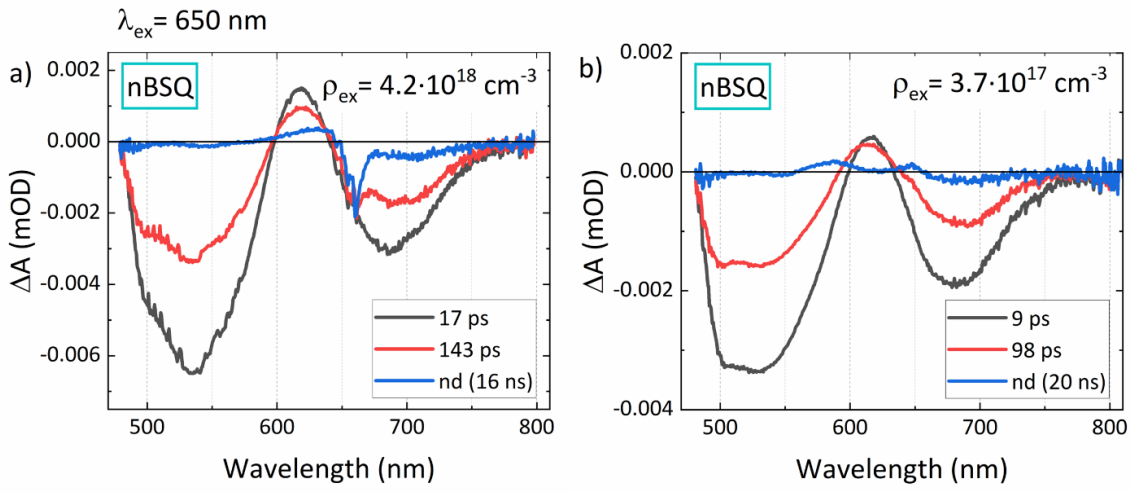

Figure 40: Evolution-associated decay spectra in three compartmental global analyses with decay rates for nBSQ under λ_{ex}= 650 nm with two different excitation densities.

Positive feature in ns-scale at 530 nm and blue-shifted ESA2 under λ_{ex} = 650 nm:

These peaks from ESA2 in nBSQ under λ_{ex} = 650 nm can be observed in the zoomed-in contour plot from Figure 41. The logarithmic time scale begins at 30 ps. As the selected spectra in Figure 41 below indicate, the ESA2, initially located at 620 nm, undergoes a blue shift, reaching its maximum at 575 nm once the GSB at 550 nm has recovered within 200 ps. However, starting from 2 ns and centered at 525 nm, a positive feature appears, as indicated by the blue arrow on the selected spectrum in red. This could be

assigned to an excitation of the triplet state T1 that does not decay within the limitations of the system and comes from the excited singlet state at 550 nm. [25,276–278]

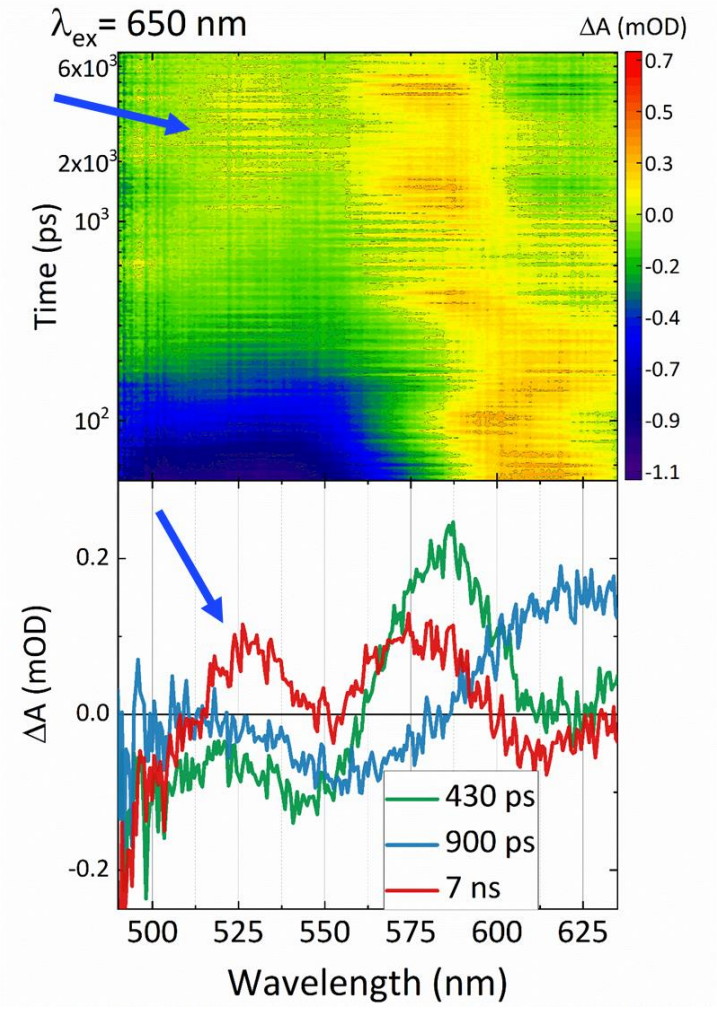

Figure 41: Zoomed-in contour plot of nBSQ ***λ_{ex}= 650 nm*** *with a density of 3.7·10^{17}/cm^3. Adapted color scale: blue negative features, green zero level, positive features range from yellow to red. The logarithmic time scale begins at 30 ps. Below are the selected spectra. The blue arrows point to the additional positive feature centered in 525 nm, which appears in 2 ns and does not decay within 7 ns.*

Oscillation Pattern

As illustrated in Figure 35 and Figure 36, oscillatory contributions are evident in the TA kinetics of n-alkyl SQ and iPSQ. These contributions emerge in regions where $\lambda_{spectrum}$ > 550nm, regardless of the excitation density or wavelength, i.e., they are not observed in the spectral region of the H-band. The cyan-shaded traces in Figure 42a show the

kinetics of 5 ps-damped coherent oscillations. A Fast Fourier Transform from peaks in Figure 42b reveals a periodicity of approximately 1.2 ps, here nBSQ as an example of all n-alkyl. For iPSQ, as shown in Figure 34d, these oscillations become noticeable for $\lambda_{spectrum}$ > 500nm and display a more rapid emergence than that observed for n-alkyl SQ, presenting a periodicity of roughly 600 fs. A direct correlation exists between the intensity of absorption in the CT-band and the periodicity of the oscillations. iPSQ exhibits its maximum absorption in the CT-band and oscillates more rapidly than the n-alkyl SQ, which possess a CT-band but are predominantly characterized by the H-band. In contrast, SQIB exhibits no discernible oscillation pattern, as expected, because it lacks a CT-band.

Previous literature has documented similar patterns in TA spectra of other organic molecules, particularly those that exhibit molecular vibrations with a periodicity of about 100 fs. [279,280] Various studies suggest that oscillations in the pump-probe spectra are vibronic couplings, attributable to the interference of two modes corresponding to single, double, and triple bonds stretching, with periods of ∼20 fs.[272, 281–283] Much longer oscillations of the order of ns were seen in the ESA region of TA spectra related to triplet transitions, but without any explanation.[284] Also, coherent oscillations of the same order as the oscillations in this chapter, also in the ESA region of TA measurements, were assigned to the presence of coordinated, low-energy movements in additional molecular segments that occur concurrently with the principal photochemical alteration of ring-opening reaction in fulgides.[285,286] This may imply that the fluctuations in the TA SQ could be attributable to some degree of aggregate degradation.

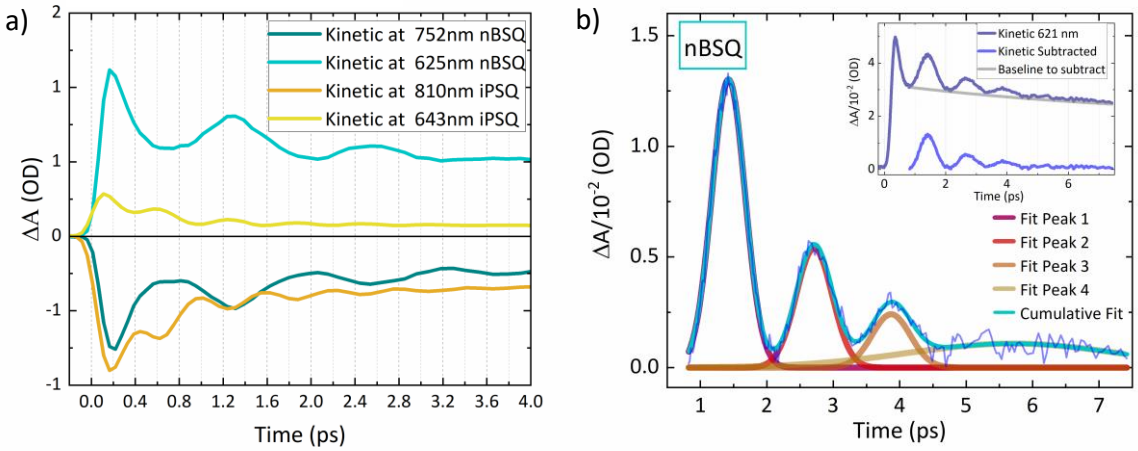

Figure 42: Vibration contribution kinetics for nBSQ (in cyan), with a period of ~ 1.2 ps compared to iPSQ (in yellow) with a period of ~ 0.6 ps. b) Cumulative fit of first oscillations in kinetic at 621 nm of nBSQ under excitation 550 nm.

5.4.3 Conclusions

This chapter studies the photophysical properties of aggregates of squaraines and planar molecules with D – A – D structures. The slip-stacked with various alkyl-chain lengths (nBSQ, nPSQ, nOSQ, nDSQ) forms on thin films compared with the amorphous forms of SQIB and iPSQ.

Both monomers of SQIB and nBSQ show the same single electronic 0-0 transition in 650 nm and vibronic 0-1 in 600 nm with excitation to and decay from S1 within ~2.5 ns. This indicates that the type of alkyl chain does not affect the intramolecular processes. There is no evidence of intramolecular intersystem crossing, which is consistent with the expected weak SOC in SQ.

The effect of the slip-stacking aggregation is seen in the peak splitting of the steady-state absorption profile of the n-alkyl SQ. This spectrum results from mixing the H-aggregate exciton state with a CT state, as assigned by comparison with SQIB, with H-aggregate characteristics proved in literature, and iPSQ, with a strong CT band. When exciting in the CT band, the absorption profile and fluorescence quenching corroborate the assignment to a CT band from 650 nm.

The intensity of fluorescence and the absorption properties of the CT state depend on the length of the alkyl chain. The length of the alkyl chain negatively affects the electronic interactions between molecules. Consequently, SF is not anticipated from SQ with long (more than 4 Carbons) alkyl chains. However, it might be feasible in a shorter molecule like nBSQ.

Generally, interactions between excited and ground-state chromophores within aggregates can catalyze a singlet fission transition from $S_n + S_0$ to T_1T_1. This may occur from an H band or CT band fulfilling the mentioned energy condition. This can be seen in the ESA of the triplet, which appears delayed relative to the ESA of the singlet state.

In the present TA data, when exciting n-alkyl with $\lambda_{ex} = 550$ nm, the concurrent increase in the relative amplitude of the ESA3, observed in the region of 880 nm at 400 fs with respect to the ESA1, which is assigned to a singlet state, is a feature of unknown origin. Further DFT calculations could elucidate if it is indeed related to a delayed triplet state

to this ESA3. The energy level of this triplet remains unknown; therefore, the assignment of this to a triplet resulting from a SF process is now a mere assumption.

Two similar uncertain cases are observed in TAS of nBSQ under λ_{ex} = 650 nm at low excitation density. First, the spectral region around 575 nm shows a non-decaying positive feature at 430 ps once the GSB has recovered within 200 ps. Secondly, in the spectral region around 525 nm, another non-decaying positive feature appears at 2 ns. These two late-appearing ESAs undergo relaxation to the S_0 ground state on timescales exceeding 7 ns. Since they appear when excitation densities are lower than $1 \cdot 10^{18}/cm^3$, it is less likely that this is a heating artifact. They are observed when exciting on the CT-band maximum at 650 nm. This could indicate that a possible SF mechanism would be CT-mediated.

In steady-state absorption, it was observed that the CT band vanishes with the length of the alkyl chain, as well as the strength of the ESA3 of the triplet manifold, a relation that could indicate that the SF process is also CT mediated.[269]

Additionally, an oscillatory pattern is observed in slip-stacked aggregates with a period of 1.2 ps and in amorphous iPSQ with a period of 600 fs. This is intrinsically dependent on the energy splitting levels after aggregation so that in pure H-band aggregation as SQIB, it does not appear, and in strong CT character molecules as iPSQ, the oscillations are faster than in n-alkyl, where CT is not predominantly present.

For slip-stacked n-alkyl SQ, the relative intensity of the CT-band with respect to the H-band decreases when the alkyl chain length is increased. In the case of steady-state absorption, it goes from 80% to 45% CT/H-band oscillator strength. However, in TAS measurements, it goes from 70% to 15%. This quenching in the CT intensity demonstrates the contribution of ESAs to the spectra. The fluorescence is quenched in dependence with the even-numbered alkyl chain. The trend in ESA features that correlates with the trend in CT character may indicate some photophysical process that is CT mediated, possibly SF.

The effect of n-alkyl SQ aggregation can be seen upon photoexcitation SQ relax through a complex pathway that involves triplet states. Those triplets are not expected to be

from ISC due to the weak SOC in SQ but eventually from spin-allowed SF. This study has also demonstrated the effect of the alkyl chain length in aggregates by diminishing the transfer of charge necessary for a successful SF. [244,287,288]

5.5 Further Steps

The findings of Collison's group on SQ aggregates showed that the annealing process reduces the efficiency of SQ-based solar cells due to phase separation between the SQ and acceptor molecules. New n-alkyl aggregates annealed at various temperatures will have different slip angles and, therefore, a variable CT character. This could influence the previously observed oscillations typically attributed to vibronic transitions in the CT-excited state. [268,269]

While the energy of the S_1 state can be inferred from the steady-state absorption maxima, the energy of the T_1 state ($T_1 \leftarrow S_0$) remains elusive. Theoretical calculations employing Density Functional Theory (DFT) to solve the Schrödinger equation for the high atomic-SQ molecule can yield precise energies for both the S_1 and T_1 states, allowing insight into the energetic conditions required for SF. Coinciding with the latest revision of this manuscript (in preparation), preliminary calculations by coworker N. Ugur have indicated that for nDSQ $E(S_1)$ = 2.46 eV (~ 504 nm), and $E(T_1)$ = 1.35 eV (~ 918 nm). A discrepancy of 25 nm exists between these calculations and the maximum of the steady-state absorption in nDSQ, which could be interpreted as a systematic error. The energy of the T_1 state constitutes 55% of the S_1 state, marginally exceeding the SF energy condition that requires $E(T_1)$ to be at most 50% of $E(S_1)$. However, these calculations should be viewed as illustrative. First, the molecule nDSQ possesses the weakest CT character owing to its long alkyl chain length. Given that the expected SF in SQ is CT-facilitated, nDSQ may not be the most suitable candidate for SF discovery in SQ. Second, the chosen intermolecular distance for the slip-stacked aggregate used in these calculations has not been specified, which is relevant as both CT and the aggregate type are influenced by slip-stacking distances. Therefore, future DFT calculations on nBSQ could reveal SF-friendly energy levels for singlet and triplets.

Measurements under low temperatures could see the effect of the temperature on the coherent oscillation pattern.

Further, TA measurements with different excitation densities will provide information about possible heating effects, as measurements seen in section 4.3.1.2. Coinciding with the revision of the latest version of this manuscript, N. Ugur conducted measurements of exciting nBSQ with a very high density (power of 200 µW), comparing it with the usual excitation (power of 15 µW) as the grey trace in Figure 43 indicates. In this figure, selected spectra of the data presented in this chapter have been normalized to the minimum of the GSB in the CT band. Together with the density-dependent measurements of N. Ugur, it can be preliminarily concluded that the delay-dependent red-shift in the spectral region of 600 - 675 nm is not due to heating effects, then those would have created a blue-shift, due to the negative contribution of ΔA (200µW) - ΔA (15µW).

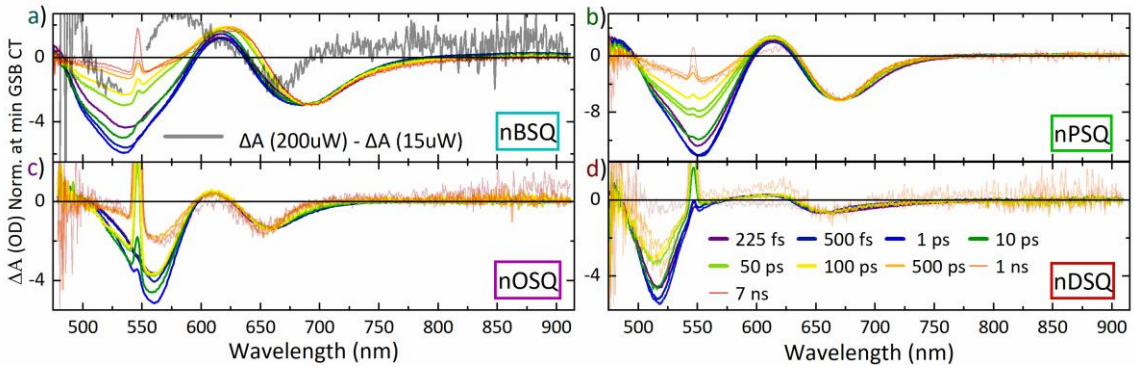

Figure 43: Normalized to the minimum GSB at CT TA spectra for n-alkyl SQ (own data) and overlayed in grey the heating effects contribution (by N.Ugur). It shows that the redshift effect in the CT is not due to heating effects.

Concerning the molecular structure of SQ, a promising next step would involve introducing nitrogen atoms into the aromatic core, as this has been shown to increase the diradical character, which subsequently lowers the energy of the lowest triplet state, favoring the SF energy condition fulfillment.[289]

Appendix

6.1 α and β-CuPc

6.1.1 GIWAXS Measurements

Utilizing the Grazing-Incidence Wide-Angle X-ray Scattering (GIWAXS) technique, colleagues led by Dr. Marszalek conducted the following measurements needed for the publication of Chapter 4.[146]

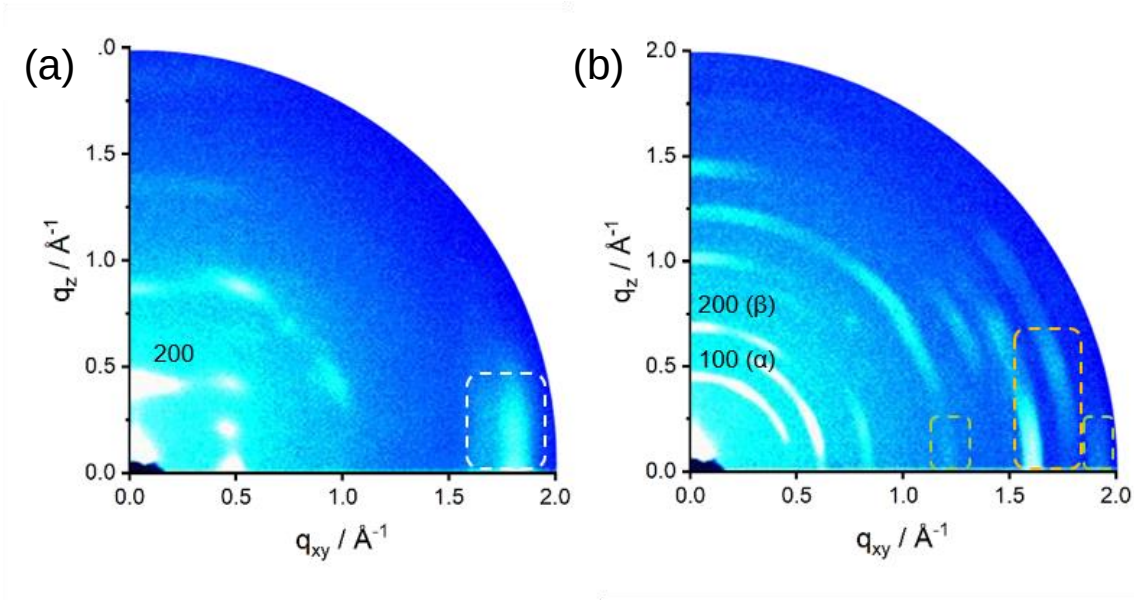

Figure 44: GIWAXS patterns of (a) α-CuPc (as-deposited) and (b) β-CuPc (annealed) thin films. Only the major reflection of the phases are assigned by the Miller index, while dashed boxes indicate reflections related to intracolumnar CuPc packing (white – α-herringbone, orange – α-brickstone, green – β-phase).

The as-deposited film reveals a characteristic α-herringbone structure[167] with CuPc molecules arranged perpendicular to the substrate (Figure 44a). As indicated by the wide-angle reflections (white dashed box in Figure 44a), the molecules are in-plane shifted towards each other, resulting in an interplanar distance of 3.45 Å and Cu-Cu distance of 3.75 Å. After annealing, the scattering intensities form arcs due to a broader orientation of the crystallites towards the surface (Figure 44b). Furthermore, the coexistence of two phases is identified based on the assignment of the reflections. New wide-angle reflections (orange dashed box in Figure 44b) are characteristic of the α-brickstone structure with interplanar and Cu-Cu distances of 3.49 Å and 3.85 Å, respectively, as well as a CuPc tilt angle of 75° with respect to the surface. Additionally,

reflections for the β-phase are found in which the CuPc adapt a larger molecular displacement in the stacks resulting in Cu-Cu distance of 4.95 Å and interplanar distance 3.30 Å (green boxes in Figure 44b).

6.2 Squaraines

6.2.1 TAS in SQIB UV-Vis Range

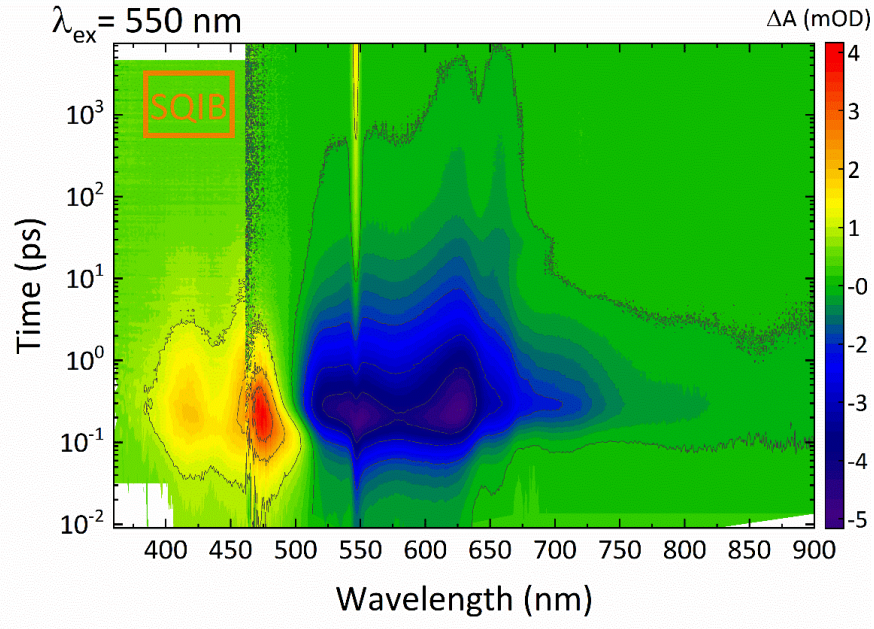

Figure 45: Artificially colored contour plot of SQIB under ex= 550 nm in combined uv to visible spectral range.

6.2.2 Excitation Density and Decay Rates

Compound	λ_{ex} (nm)	ρ_{ex} ($10^{18}cm^{-3}$)	τ_1	τ_2	τ_3
SQIB	550	4.7	1.2 ps	26 ps	59 ns
SQIB uv	550	8	1.2 ps	22 ps	0.8 ns
SQIB crop	650	1.8	3 ps	31 ps	13 ns
iPSQ	550	4	0.6 ps	33 ps	500 ns
nBSQ	550	7	1.5 ps	31 ps	8 ns
nBSQ uv	550	12	5.7 ps	81 ps	10 ns
nBSQ	650	3.7	9 ps	98 ps	20 ns
nBSQ	650	4.3	17 ps	143 ps	16 ns
nPSQ	550	7.4	1.1 ps	26 ps	2 ns
nOSQ	550	6.2	2.5 ps	75 ps	93 ns
nDSQ	550	3.2	2 ps	45 ps	18 ns

Table 3: Decay rates of TA spectra samples under study excited at 550 nm and 650 nm with given excitation densities.

6.2.3 Relative CT- band Intensity

Compound	Chain Length	Absorption	Fluorescence	CT -TAS (220 fs)
nBSQ	4	80 %	20 %	67 %
nPSQ	5	72 %	53 %	48 %
nOSQ	8	66 %	34 %	38 %
nDSQ	10	43 %	55 %	15 %

Table 4: Relative CT-band intensity to the H-band intensity for n-alkyl SQ.

Table of Figures

Bibliography

(1) Tang, C. W. Two-Layer Organic Photovoltaic Cell. *Appl. Phys. Lett.* **1986**, *48* (2), 183–185. https://doi.org/10.1063/1.96937.

(2) Kippelen, B.; Bredas, J.-L. Organic Photovoltaics. *Energy Env. Sci* **2009**, *2*, 251–261. https://doi.org/10.1039/b812502n.

(3) Wasielewski, M. R. Self-Assembly Strategies for Integrating Light Harvesting and Charge Separation in Artificial Photosynthetic Systems. *Acc. Chem. Res.* **2009**, *42* (12), 1910–1921. https://doi.org/10.1021/ar9001735.

(4) Gust, D. An Illustrative History of Artificial Photosynthesis. *Adv. Bot. Res.* **2016**, *79*, 1–42. https://doi.org/10.1016/bs.abr.2016.02.004.

(5) Goushi, K.; Yoshida, K.; Sato, K.; Adachi, C. Organic Light-Emitting Diodes Employing Efficient Reverse Intersystem Crossing for Triplet-to-Singlet State Conversion. *Nat. Photonics* **2012**, *6* (4), 253–258. https://doi.org/10.1038/nphoton.2012.31.

(6) Andersson, M. R.; Yu, G.; Heeger, A. J. Photoluminescence and Electroluminescence of Films from Soluble PPV-Polymers. *Synth. Met.* **1997**, *85* (1–3), 1275–1276. https://doi.org/10.1016/s0379-6779(97)80238-x.

(7) Burroughes, J. H.; Bradley, D. D. C.; Brown, A. R.; Marks, R. N.; Mackay, K.; Friend, R. H.; Burns, P. L.; Holmes, A. B. Light-Emitting Diodes Based on Conjugated Polymers. *Nature* **1990**, *347* (6293), 539–541. https://doi.org/10.1038/347539a0.

(8) Chesterfield, R. J.; McKeen, J. C.; Newman, C. R.; Ewbank, P. C.; Da Silva Filho, D. A.; Brédas, J. L.; Miller, L. L.; Mann, K. R.; Frisbie, C. D. Organic Thin Film Transistors Based on N-Alkyl Perylene Diimides: Charge Transport Kinetics as a Function of Gate Voltage and Temperature. *J. Phys. Chem. B* **2004**, *108* (50), 19281–19292. https://doi.org/10.1021/jp046246y.

(9) Oh, J. H.; Liu, S.; Bao, Z.; Schmidt, R.; Würthner, F. Air-Stable n -Channel Organic Thin-Film Transistors with High Field-Effect Mobility Based on N, N' -Bis(Heptafluorobutyl)-3,4:9,10-Perylene Diimide. *Appl. Phys. Lett.* **2007**, *91* (21). https://doi.org/10.1063/1.2803073.

(10) Bardeen, C. J. Excitonic Processes in Molecular Crystalline Materials. *MRS Bull.* **2013**, *38* (1), 65–71. https://doi.org/10.1557/mrs.2012.312.

(11) Bialas, D.; Kirchner, E.; Röhr, M. I. S.; Würthner, F. Perspectives in Dye Chemistry: A Rational Approach toward Functional Materials by Understanding the Aggregate State. *J. Am. Chem. Soc.* **2021**, *143* (12), 4500–4518. https://doi.org/10.1021/jacs.0c13245.

(12) Köhler, A.; Bässler, H. *Electronic Processes in Organic Semiconductors: An Introduction*; Wiley-VCH Verlag GmbH & Co. KGaA: Weinheim, Germany, 2015.

(13) Kasha, M.; Rawls, H. R.; El-Bayoumi, M. A. The exciton model in molecular spectroscopy. *Pure Appl. Chem.* **1965**, *11* (3–4), 371–392. https://doi.org/10.1351/pac196511030371.

(14) Hochstrasser, R. M.; Kasha, M. Application of the Exciton Model to Mono-Molecular Lamellar Systems*. *Photochem. Photobiol.* **1964**, *3* (4), 317–331. https://doi.org/10.1111/j.1751-1097.1964.tb08155.x.

(15) McRae, E. G.; Kasha, M. Enhancement of Phosphorescence Ability upon Aggregation of Dye Molecules. *J. Chem. Phys.* **1958**, *28*, 721–722. https://doi.org/10.1063/1.1744225.

(16) Davydov, A. S. The Theory of Molecular Excitons. *Sov. Phys. Uspekhi* **1964**, *7* (2), 145–178. https://doi.org/10.1070/pu1964v007n02abeh003659.

(17) Davydov, A. S. The Theory of Molecular Excitons. *Uspekhi Fiz. Nauk* **1964**, *82* (3), 393–448. https://doi.org/10.3367/ufnr.0082.196403a.0393.

(18) Sheka, E. F. Davydov Splitting in the Absorption Spectra of Molecular Crystals. *Mol. Cryst. Liq. Cryst.* **1975**, *29* (2), 323–343. https://doi.org/10.1080/15421407508083209.

(19) Hestand, N. J.; Spano, F. C. Expanded Theory of H- and J-Molecular Aggregates: The Effects of Vibronic Coupling and Intermolecular Charge Transfer. *Chem. Rev.* **2018**, *118* (15), 7069–7163. https://doi.org/10.1021/acs.chemrev.7b00581.

(20) Hestand, N. J.; Spano, F. C. Molecular Aggregate Photophysics beyond the Kasha Model: Novel Design Principles for Organic Materials. *Acc. Chem. Res.* **2017**, *50* (2), 341–350. https://doi.org/10.1021/acs.accounts.6b00576.

(21) Oleson, A.; Zhu, T.; Dunn, I. S.; Bialas, D.; Bai, Y.; Zhang, W.; Dai, M.; Reichman, D. R.; Tempelaar, R.; Huang, L.; Spano, F. C. Perylene Diimide-Based Hj- And hJ-Aggregates- And Prospect of Exciton Band Shape Engineering in Organic Materials. *J. Phys. Chem. C* **2019**, *123* (33), 20567–20578. https://doi.org/10.1021/acs.jpcc.9b04429.

(22) Beljonne, D.; Yamagata, H.; Brédas, J.-L.; Spano, F. C.; Olivier, Y. Charge-Transfer Excitations Steer the Davydov Splitting and Mediate Singlet Exciton Fission in Pentacene. *Phys. Rev. Lett.* **2013**, *110* (22), 226402. https://doi.org/10.1103/PhysRevLett.110.226402.

(23) Hoffmann, M.; Soos, Z. G.; Leo, K. Absorption Spectra and Band Structure of Mixed Frenkel-Charge-Transfer Vibronic States in One-Dimensional Molecular Crystals. *Nonlinear Opt.* **2006**, *29*, 227–237.

(24) Schmidt, K. Quantum Confinement in Linear Molecular Chains with Strong Mixing of Frenkel and Charge-Transfer Excitons. *Phys. Lett. A* **2002**, *293* (1), 83–92. https://doi.org/10.1016/S0375-9601(01)00841-6.

(25) Basel, B. S.; Zirzlmeier, J.; Hetzer, C.; Reddy, S. R.; Phelan, B. T.; Krzyaniak, M. D.; Volland, M. K.; Coto, P. B.; Young, R. M.; Clark, T.; Thoss, M.; Tykwinski, R. R.; Wasielewski, M. R.; Guldi, D. M. Evidence for Charge-Transfer Mediation in the Primary Events of Singlet Fission in a Weakly Coupled Pentacene Dimer. *Chem* **2018**, *4* (5), 1092–1111. https://doi.org/10.1016/j.chempr.2018.04.006.

(26) Hestand, N. J.; Yamagata, H.; Xu, B.; Sun, D.; Zhong, Y.; Harutyunyan, A. R.; Chen, G.; Dai, H. L.; Rao, Y.; Spano, F. C. Polarized Absorption in Crystalline Pentacene: Theory vs Experiment. *J. Phys. Chem. C* **2015**, *119* (38), 22137–22147. https://doi.org/10.1021/acs.jpcc.5b07163.

(27) Qi, D.; Su, H.; Bastjan, M.; Jurchescu, O. D.; Palstra, T. M.; Wee, A. T. S.; Rübhausen, M.; Rusydi, A. Observation of Frenkel and Charge Transfer Excitons in Pentacene Single Crystals Using Spectroscopic Generalized Ellipsometry. *Appl. Phys. Lett.* **2013**, *103* (11), 113303. https://doi.org/10.1063/1.4811758.

(28) Sebastian, L.; Weiser, G.; Bassler, H. CHARGE TRANSFER TRANSITIONS IN SOLID TETRACENE AND PENTACENE STUDIED BY ELECTROABSORPTION. *Chem. Phys.* **1981**, *61* (1–2), 125–135.

(29) Hennessy, M. H.; Soos, Z. G.; Pascal, R. A.; Girlando, A. Vibronic Structure of PTCDA Stacks: The Exciton-Phonon-Charge-Transfer Dimer. *Chem. Phys.* **1999**, *245* (1–3), 199–212. https://doi.org/10.1016/S0301-0104(99)00082-8.

(30) Hoffmann, M.; Schmidt, K.; Fritz, T.; Hasche, T.; Agranovich, V. M.; Leo, K. The Lowest Energy Frenkel and Charge-Transfer Excitons in Quasi-One-Dimensional Structures: Application to MePTCDI and PTCDA Crystals. *Chem. Phys.* **2000**, *258* (1), 73–96. https://doi.org/10.1016/S0301-0104(00)00157-9.

(31) Hong, Y.; Kim, J.; Kim, W.; Kaufmann, C.; Kim, H.; Würthner, F.; Kim, D. Efficient Multiexciton State Generation in Charge-Transfer-Coupled Perylene Bisimide Dimers via Structural Control. *J. Am. Chem. Soc.* **2020**, *142* (17), 7845–7857. https://doi.org/10.1021/jacs.0c00870.

(32) Austin, A.; Hestand, N. J.; McKendry, I. G.; Zhong, C.; Zhu, X.; Zdilla, M. J.; Spano, F. C.; Szarko, J. M. Enhanced Davydov Splitting in Crystals of a Perylene Diimide Derivative. *J. Phys. Chem. Lett.* **2017**, *8* (6), 1118–1123. https://doi.org/10.1021/acs.jpclett.7b00283.

(33) Hestand, N. J.; Spano, F. C. Interference between Coulombic and CT-Mediated Couplings in Molecular Aggregates: H- to J-Aggregate Transformation in Perylene-Based π-Stacks. *J. Chem. Phys.* **2015**, *143* (24), 244707. https://doi.org/10.1063/1.4938012.

(34) Gisslén, L.; Scholz, R. Crystallochromy of Perylene Pigments: Interference between Frenkel Excitons and Charge-Transfer States. *Phys. Rev. B* **2009**, *80* (11), 115309. https://doi.org/10.1103/PhysRevB.80.115309.

(35) Hestand, N. J.; Zheng, C.; Penmetcha, A. R.; Cona, B.; Cody, J. A.; Spano, F. C.; Collison, C. J. Confirmation of the Origins of Panchromatic Spectra in Squaraine Thin Films Targeted for Organic Photovoltaic Devices. *J. Phys. Chem. C* **2015**, *119* (33), 18964–18974. https://doi.org/10.1021/acs.jpcc.5b05095.

(36) Balzer, F.; Hestand, N. J.; Zablocki, J.; Schnakenburg, G.; Lützen, A.; Schiek, M. Spotlight on Charge-Transfer Excitons in Crystalline Textured n-Alkyl Anilino Squaraine Thin Films. *J. Phys. Chem. C* **2022**. https://doi.org/10.1021/acs.jpcc.2c03665.

(37) Zheng, C.; Penmetcha, A. R.; Cona, B.; Spencer, S. D.; Zhu, B.; Heaphy, P.; Cody, J. A.; Collison, C. J. Contribution of Aggregate States and Energetic Disorder to a Squaraine System Targeted for Organic Photovoltaic Devices. *Langmuir* **2015**, *31* (28), 7717–7726. https://doi.org/10.1021/acs.langmuir.5b01045.

(38) Doctor, L. P.; Naumann, M.; Ziegs, F.; Büchner, B.; Popov, A.; Knupfer, M. Strong Photophysical Diversity and the Role of Charge Transfer Excitons in Transition Metal

Phthalocyanine β-Phases. *J. Phys. Chem. C* **2021**, *125* (22), 12398–12404. https://doi.org/10.1021/acs.jpcc.1c02654.

(39) Popescu, A.; Younts, R. A.; Hoffman, B.; McAfee, T.; Dougherty, D. B.; Ade, H. W.; Gundogdu, K.; Bondarev, I. V. Monitoring Charge Separation Processes in Quasi-One-Dimensional Organic Crystalline Structures. *Nano Lett.* **2017**, *17* (10), 6056–6061. https://doi.org/10.1021/acs.nanolett.7b02471.

(40) Bondarev, I. V.; Popescu, A.; Younts, R. A.; Hoffman, B.; McAfee, T.; Dougherty, D. B.; Gundogdu, K.; Ade, H. W. Lowest Energy Frenkel and Charge Transfer Exciton Intermixing in One-Dimensional Copper Phthalocyanine Molecular Lattice. *Appl. Phys. Lett.* **2016**, *109* (21), 213302. https://doi.org/10.1063/1.4968821.

(41) Pandey, R.; Moon, A. P.; Bender, J. A.; Roberts, S. T. Extracting the Density of States of Copper Phthalocyanine at the SiO2 Interface with Electronic Sum Frequency Generation. *J. Phys. Chem. Lett.* **2016**, *7* (6), 1060–1066. https://doi.org/10.1021/acs.jpclett.6b00178.

(42) Knupfer, M.; Schwieger, T.; Peisert, H.; Fink, J. Mixing of Frenkel and Charge Transfer Excitons in Quasi-One-Dimensional Copper Phthalocyanine Molecular Crystals. *Phys. Rev. B* **2004**, *69* (16), 165210. https://doi.org/10.1103/PhysRevB.69.165210.

(43) Naumann, M.; Knupfer, M. Complex Momentum Behavior of Electronic Excitations in β -CuPc. *J. Chem. Phys.* **2018**, *149* (8), 084704. https://doi.org/10.1063/1.5046388.

(44) Yoshida, H.; Tokura, Y.; Koda, T. Charge-Transfer Excitation Bands in Electro-Absorption Spectra of Metal (Co, Ni, Cu, Zn)-Phthalocyanine Films. *Chem. Phys.* **1986**, *109* (2–3), 375–382. https://doi.org/10.1016/0301-0104(86)87066-5.

(45) Feng, S.; Wang, Y. C.; Ke, Y.; Liang, W. Z.; Zhao, Y. Effect of Charge-Transfer States on the Vibrationally Resolved Absorption Spectra and Exciton Dynamics in ZnPc Aggregates: Simulations from a Non-Makovian Stochastic Schrödinger Equation. *J. Chem. Phys.* **2020**, *153* (3), 034116. https://doi.org/10.1063/5.0013935.

(46) Feng, S.; Wang, Y.-C.; Liang, W.; Zhao, Y. Vibrationally Resolved Absorption Spectra and Ultrafast Exciton Dynamics in α-Phase and β-Phase Zinc Phthalocyanine Aggregates. *Phys. Chem. Chem. Phys.* **2022**, *24* (5), 2974–2987. https://doi.org/10.1039/D1CP03600A.

(47) *Marie Curie the scientist | Biog, facts & quotes*. Marie Curie. https://www.mariecurie.org.uk/who/our-history/marie-curie-the-scientist (accessed 2023-08-30).

(48) Planck, M. Ueber Das Gesetz Der Energieverteilung Im Normalspectrum. *Ann. Phys.* **1901**, *309* (3), 553–563. https://doi.org/10.1002/andp.19013090310.

(49) Einstein, A. Über Einen Die Erzeugung Und Verwandlung Des Lichtes Betreffenden Heuristischen Gesichtspunkt. *Ann. Phys.* **1905**, *322* (6), 132–148. https://doi.org/10.1002/andp.19053220607.

(50) Bohr, N. I. On the Constitution of Atoms and Molecules. *Lond. Edinb. Dublin Philos. Mag. J. Sci.* **1913**, *26* (151), 1–25. https://doi.org/10.1080/14786441308634955.

(51) *"Waves and Quanta" in Nature, a weekly journal of science, No. 2815, Vol. 112, October 13, 1923, p. 540. de Broglie, Louis de:: Akzeptabel Half cloth binding. (1923) |*

Antiquariat Braun. https://www.iberlibro.com/Waves-Quanta-Nature-weekly-journal-science/30090545312/bd (accessed 2023-08-23).

(52) Schrodinger, E.; Lindemann, F. A. Contributions to Born's New Theory of the Electromagnetic Field. *Proc. R. Soc. Lond. Ser. - Math. Phys. Sci.* **1997**, *150* (870), 465–477. https://doi.org/10.1098/rspa.1935.0116.

(53) Born, M.; Oppenheimer, R. Zur Quantentheorie Der Molekeln. *Ann. Phys.* **1927**, *389* (20), 457–484. https://doi.org/10.1002/andp.19273892002.

(54) McNab, I. R. Rotational Spectroscopy, Theory. In *Encyclopedia of Spectroscopy and Spectrometry (Third Edition)*; Lindon, J. C., Tranter, G. E., Koppenaal, D. W., Eds.; Academic Press: Oxford, 2017; pp 978–987. https://doi.org/10.1016/B978-0-12-803224-4.00273-9.

(55) Heisenberg, W. Über den anschaulichen Inhalt der quantentheoretischen Kinematik und Mechanik. *Z. Für Phys.* **1927**, *43* (3), 172–198. https://doi.org/10.1007/BF01397280.

(56) Mulliken, R. S. Electronic Structures of Polyatomic Molecules and Valence. II. General Considerations. *Phys. Rev.* **1932**, *41* (1), 49–71. https://doi.org/10.1103/PhysRev.41.49.

(57) *The Nobel Prize in Chemistry 1966*. NobelPrize.org. https://www.nobelprize.org/prizes/chemistry/1966/summary/ (accessed 2023-10-31).

(58) Hund, F. *Linienspektren und Periodisches System der Elemente*; Springer: Vienna, 1927. https://doi.org/10.1007/978-3-7091-5695-7.

(59) *Wade & Simek, Organic Chemistry, Global Edition, 10th Edition*. https://www.pearson.com/se/Nordics-Higher-Education/subject-catalogue/chemistry/wade-simek-Organic-Chemistry-Global-Edition-10e.html (accessed 2023-07-05).

(60) Miessler, G. L.; Fischer, P. J.; Tarr, D. A. *Inorganic Chemistry*, Fifth edition.; Pearson: Boston, 2014.

(61) Brütting, W. Introduction to the Physics of Organic Semiconductors. In *Physics of Organic Semiconductors*; John Wiley & Sons, Ltd, 2005; pp 1–14. https://doi.org/10.1002/3527606637.ch.

(62) Abragam, A.; Bleaney, B.; Abragam, A.; Bleaney, B. *Electron Paramagnetic Resonance of Transition Ions*; Oxford Classic Texts in the Physical Sciences; Oxford University Press: Oxford, New York, 2012.

(63) Atkins, P.; de Paula, J. Physical Chemistry. *Oxf. Univ. Press* **2014**, *10th ed.*, 365–366.

(64) Joshi, G.; Teferi, M. Y.; Miller, R.; Jamali, S.; Baird, D.; van Tol, J.; Malissa, H.; Lupton, J. M.; Boehme, C. Isotropic Effective Spin-Orbit Coupling in a Conjugated Polymer. *J. Am. Chem. Soc.* **2018**, *140* (22), 6758–6762. https://doi.org/10.1021/jacs.8b03069.

(65) Ballhausen, C. J. Introduction to Ligand Field Theory. *McGraw-Hill* **1962**.

(66) Slater, J. C. The Theory of Complex Spectra. *Phys. Rev.* **1929**, *34* (10), 1293–1322. https://doi.org/10.1103/PhysRev.34.1293.

(67) Pauli, W. Über den Zusammenhang des Abschlusses der Elektronengruppen im Atom mit der Komplexstruktur der Spektren. *Z. Für Phys.* **1925**, *31* (1), 765–783. https://doi.org/10.1007/BF02980631.

(68) Hund, F. Zur Deutung verwickelter Spektren, insbesondere der Elemente Scandium bis Nickel. *Z. Für Phys.* **1925**, *33* (1), 345–371. https://doi.org/10.1007/BF01328319.

(69) Hund, F. Zur Deutung der Molekelspektren. III. *Z. Für Phys.* **1927**, *43* (11), 805–826. https://doi.org/10.1007/BF01397249.

(70) *The Nobel Prize in Chemistry 1981*. NobelPrize.org. https://www.nobelprize.org/prizes/chemistry/1981/summary/ (accessed 2023-08-23).

(71) Seeman, J. I. Kenichi Fukui, Frontier Molecular Orbital Theory, and the Woodward-Hoffmann Rules. Part II. A Sleeping Beauty in Chemistry†**. *Chem. Rec.* **2022**, *22* (4), e202100300. https://doi.org/10.1002/tcr.202100300.

(72) Bruice, P. Y. *Organic Chemistry*; Pearson/Prentice Hall, 2004.

(73) Frenkel, J. On the Transformation of Light into Heat in Solids. I. *Phys. Rev.* **1931**, *37* (1), 17–44. https://doi.org/10.1103/PhysRev.37.17.

(74) Kasha, M. Relation between Exciton Bands and Conduction Bands in Molecular Lamellar Systems. *Rev. Mod. Phys.* **1959**, *31* (1), 162–169. https://doi.org/10.1103/RevModPhys.31.162.

(75) Philipps, K.; Ie, Y.; van der Zee, B.; Png, R.-Q.; Ho, P. K. H.; Chua, L.-L.; del Pino Rosendo, E.; Ramanan, C.; Wetzelaer, G.-J. A. H.; Blom, P. W. M.; Michels, J. J. Role of Linker Functionality in Polymers Exhibiting Main-Chain Thermally Activated Delayed Fluorescence. *Adv. Sci.* **2022**, *9* (19), 2200056. https://doi.org/10.1002/advs.202200056.

(76) Marcus, R. A. On the Theory of Oxidation-Reduction Reactions Involving Electron Transfer. I. *J. Chem. Phys.* **2004**, *24* (5), 966–978. https://doi.org/10.1063/1.1742723.

(77) Condon, E. A Theory of Intensity Distribution in Band Systems. *Phys. Rev.* **1926**, *28* (6), 1182–1201. https://doi.org/10.1103/PhysRev.28.1182.

(78) Franck, J.; Dymond, E. G. Elementary Processes of Photochemical Reactions. *Trans. Faraday Soc.* **1926**, *21* (February), 536–542. https://doi.org/10.1039/TF9262100536.

(79) Jablonski, A. Efficiency of Anti-Stokes Fluorescence in Dyes. *Nature* **1933**, *131* (3319), 839–840. https://doi.org/10.1038/131839b0.

(80) Valentiner, S.; Rössiger, M. Die Energieausbeute der Fluoreszenzstrahlung von Fluoreszeinlösungen bei antistokesscher Erregung. *Z. Für Phys.* **1926**, *36* (2), 81–91. https://doi.org/10.1007/BF01380125.

(81) Wawilow, S. J. Die Fluoreszenzausbeute von Farbstofflösungen als Funktion der Wellenlänge des anregenden Lichtes. II. *Z. Für Phys.* **1927**, *42* (4), 311–318. https://doi.org/10.1007/BF01397622.

(82) Kautsky, H. Energie-Umwandlungen an Grenzflächen, II. Mitteil.: H. Kautky, A. Hirsch, W. Baumeister: Photoluminescenz Fluorescierender Farbstoffe an Grenzflächen. *Berichte Dtsch. Chem. Ges. B Ser.* **1931**, *64* (8), 2053–2059. https://doi.org/10.1002/cber.19310640828.

(83) Jabłoński, A. über das Entstehen der breiten Absorptions- und Fluoreszenzbanden in Farbstofflösungen. *Z. Für Phys.* **1932**, *73* (7), 460–469. https://doi.org/10.1007/BF01349853.

(84) Lewis, G. N.; Kasha, M. Phosphorescence and the Triplet State. *J. Am. Chem. Soc.* **1944**, *66* (12), 2100–2116. https://doi.org/10.1021/ja01240a030.

(85) Frackowiak, D. The Jablonski Diagram. *J. Photochem. Photobiol. B* **1988**, *2* (3), 399. https://doi.org/10.1016/1011-1344(88)85060-7.

(86) *Physics of Organic Semiconductors*, 1st ed.; John Wiley & Sons, Ltd, 2005. https://doi.org/10.1002/3527606637.

(87) Maciejewski, A.; Safarzadeh-Amiri, A.; Verrall, R. E.; Steer, R. P. Radiationless Decay of the Second Excited Singlet States of Aromatic Thiones: Experimental Verification of the Energy Gap Law. *Chem. Phys.* **1984**, *87* (2), 295–303. https://doi.org/10.1016/0301-0104(84)85054-5.

(88) A Crash Course in Photophysics and a Classification of Primary Photoreactions. In *Photochemistry of Organic Compounds*; John Wiley & Sons, Ltd, 2009; pp 25–72. https://doi.org/10.1002/9781444300017.ch2.

(89) Siebrand, W. Radiationless Transitions in Polyatomic Molecules. I. Calculation of Franck—Condon Factors. *J. Chem. Phys.* **2004**, *46* (2), 440–447. https://doi.org/10.1063/1.1840685.

(90) Kasha, M. Characterization of Electronic Transitions in Complex Molecules. *Discuss. Faraday Soc.* **1950**, *9* (0), 14–19. https://doi.org/10.1039/DF9500900014.

(91) Stokes, G. G. XXX. On the Change of Refrangibility of Light. *Philos. Trans. R. Soc. Lond.* **1997**, *142*, 463–562. https://doi.org/10.1098/rstl.1852.0022.

(92) Giachino, G. G.; Kearns, D. R. Nature of the External Heavy-Atom Effect on Radiative and Nonradiative Singlet–Triplet Transitions. *J. Chem. Phys.* **2003**, *52* (6), 2964–2974. https://doi.org/10.1063/1.1673425.

(93) El-Sayed, M. A. Triplet State. Its Radiative and Nonradiative Properties. *Acc. Chem. Res.* **1968**, *1* (1), 8–16. https://doi.org/10.1021/ar50001a002.

(94) El-Sayed, M. A. Spin—Orbit Coupling and the Radiationless Processes in Nitrogen Heterocyclics. *J. Chem. Phys.* **2004**, *38* (12), 2834–2838. https://doi.org/10.1063/1.1733610.

(95) Hauser, A. Light-Induced Spin Crossover and the High-Spin→Low-Spin Relaxation. In *Spin Crossover in Transition Metal Compounds II*; Gütlich, P., Goodwin, H. A., Eds.; Topics in Current Chemistry; Springer: Berlin, Heidelberg, 2004; pp 155–198. https://doi.org/10.1007/b95416.

(96) Zhang, J.; Mukamel, S.; Jiang, J. Aggregation-Induced Intersystem Crossing: Rational Design for Phosphorescence Manipulation. *J. Phys. Chem. B* **2020**, *124* (11), 2238–2244. https://doi.org/10.1021/acs.jpcb.0c00654.

(97) Chen, T.; Li, M.; Liu, J. π–π Stacking Interaction: A Nondestructive and Facile Means in Material Engineering for Bioapplications. *Cryst. Growth Des.* **2018**, *18* (5), 2765–2783. https://doi.org/10.1021/acs.cgd.7b01503.

(98) McRae, E. G.; Kasha, M. The Molecular Exciton Model. In *Physical Processes in Radiation Biology*; Augenstein, L., Mason, R., Rosenberg, B., Eds.; Academic Press, 1964; pp 23–42. https://doi.org/10.1016/B978-1-4831-9824-8.50007-4.

(99) Kasha, M. Energy Transfer Mechanisms and the Molecular Exciton Model for Molecular Aggregates. *Radiat. Res.* **1963**, *20* (1), 55–70. https://doi.org/10.2307/3571331.

(100) Braslavsky, S. E. Glossary of Terms Used in Photochemistry, 3rd Edition (IUPAC Recommendations 2006). *Pure Appl. Chem.* **2007**, *79* (3), 293–465. https://doi.org/10.1351/pac200779030293.

(101) Davydov, A. S. *Theory of Molecular Excitons*; Springer US: Boston, MA, 1971. https://doi.org/10.1007/978-1-4899-5169-4.

(102) *Physical and Chemical Mechanisms in Molecular Radiation Biology*; Glass, W. A., Varma, M. N., Eds.; Springer US: Boston, MA, 1991. https://doi.org/10.1007/978-1-4684-7627-9.

(103) Knoester, J. Optical Properties of Molecular Aggregates. In *Organic Nanostructures: Science and Applications*; IOS Press, 2002; pp 149–186. https://doi.org/10.3254/978-1-61499-005-5-149.

(104) Scheibe, G. Über Die Veränderlichkeit Der Absorptionsspektren in Lösungen Und Die Nebenvalenzen Als Ihre Ursache. *Angew. Chem.* **1937**, *50* (11), 212–219. https://doi.org/10.1002/ange.19370501103.

(105) Scheibe, G.; Kandler, L.; Ecker, H. Polymerisation und polymere Adsorption als Ursache neuartiger Absorptionsbanden von organischen Farbstoffen. *Naturwissenschaften* **1937**, *25* (5), 75–75. https://doi.org/10.1007/BF01493278.

(106) Jelley, E. E. Spectral Absorption and Fluorescence of Dyes in the Molecular State. *Nature* **1936**, *138* (3502), 1009–1010. https://doi.org/10.1038/1381009a0.

(107) Jelley, E. E. Molecular, Nematic and Crystal States of I: I-Diethyl--Cyanine Chloride. *Nature* **1937**, *139* (3519), 631–631. https://doi.org/10.1038/139631b0.

(108) Würthner, F.; Kaiser, T. E.; Saha-Möller, C. R. J-Aggregates: From Serendipitous Discovery to Supramolecular Engineering of Functional Dye Materials. *Angew. Chem. Int. Ed.* **2011**, *50* (15), 3376–3410. https://doi.org/10.1002/anie.201002307.

(109) Cooper, W. Multiplet Structure of Aggregated States in 1,1'-Diethyl-2,2'-Cyanine Dye. *Chem. Phys. Lett.* **1970**, *7* (1), 73–77. https://doi.org/10.1016/0009-2614(70)80252-4.

(110) Mott, N. F.; Gurney, R. W. *Electronic Processes in Ionic Crystals, by N.F. Mott and R.W. Gurney*, 2d ed.; International series of monographs on physics; Clarendon Press: Oxford, 1940.

(111) Wannier, G. H. The Structure of Electronic Excitation Levels in Insulating Crystals. *Phys. Rev.* **1937**, *52* (3), 191–197. https://doi.org/10.1103/PhysRev.52.191.

(112) Gajdos, F.; Valner, S.; Hoffmann, F.; Spencer, J.; Breuer, M.; Kubas, A.; Dupuis, M.; Blumberger, J. Ultrafast Estimation of Electronic Couplings for Electron Transfer between π-Conjugated Organic Molecules. *J. Chem. Theory Comput.* **2014**, *10* (10), 4653–4660. https://doi.org/10.1021/ct500527v.

(113) Kim, J. H.; Schembri, T.; Bialas, D.; Stolte, M.; Würthner, F. Slip-Stacked J-Aggregate Materials for Organic Solar Cells and Photodetectors. *Adv. Mater.* **2022**, *34* (22), 2104678. https://doi.org/10.1002/adma.202104678.

(114) Vauthey, E. Photoinduced Symmetry-Breaking Charge Separation. *ChemPhysChem* **2012**, *13* (8), 2001–2011. https://doi.org/10.1002/cphc.201200106.

(115) Petelenz, P. Mixing of Frenkel Excitons and Ionic Excited States in a Linear Crystal of Donor-Acceptor Complex. *Phys. Status Solidi B* **1979**, *94* (2), 371–379. https://doi.org/10.1002/pssb.2220940206.

(116) Young, R. M.; Wasielewski, M. R. Mixed Electronic States in Molecular Dimers: Connecting Singlet Fission, Excimer Formation, and Symmetry-Breaking Charge Transfer. *Acc. Chem. Res.* **2020**, *53* (9), 1957–1968. https://doi.org/10.1021/ACS.ACCOUNTS.0C00397.

(117) *The Nobel Prize in Chemistry 1999*. NobelPrize.org. https://www.nobelprize.org/prizes/chemistry/1999/summary/ (accessed 2024-01-20).

(118) Scholes, G. D.; Fleming, G. R.; Olaya-Castro, A.; van Grondelle, R. Lessons from Nature about Solar Light Harvesting. *Nat. Chem.* **2011**, *3* (10), 763–774. https://doi.org/10.1038/nchem.1145.

(119) Feldman, T. B.; Smitienko, O. A.; Shelaev, I. V.; Gostev, F. E.; Nekrasova, O. V.; Dolgikh, D. A.; Nadtochenko, V. A.; Kirpichnikov, M. P.; Ostrovsky, M. A. Femtosecond Spectroscopic Study of Photochromic Reactions of Bacteriorhodopsin and Visual Rhodopsin. *J. Photochem. Photobiol. B* **2016**, *164*, 296–305. https://doi.org/10.1016/j.jphotobiol.2016.09.041.

(120) Knowles, K. E. Three Applications of Ultrafast Transient Absorption Spectroscopy of Semiconductor Thin Films: Spectroelectrochemistry, Microscopy, and Identification of Thermal Contributions. *J. Mater. Chem. C* **2018**.

(121) Zewail, A. H. Femtochemistry: Atomic-Scale Dynamics of the Chemical Bond. *J. Phys. Chem. A* **2000**, *104* (24), 5660–5694. https://doi.org/10.1021/jp001460h.

(122) LAMBDA 850/950/1050 UV/Vis and UV/Vis/NIR Spectrophotometers.

(123) Li, P.; Askes, S. H. C.; del Pino Rosendo, E.; Ariese, F.; Ramanan, C.; von Hauff, E.; Baldi, A. Nanoscale Thermometry of Plasmonic Structures via Raman Shifts in Copper Phthalocyanine. *J. Phys. Chem. C* **2023**, *127* (20), 9690–9698. https://doi.org/10.1021/acs.jpcc.3c01561.

(124) *USB400 Miniature CCD-Array Spectrometer*. https://www.photonics.com/Products/USB400_Miniature_CCD-Array_Spectrometer/pr25793 (accessed 2023-08-31).

(125) Skoog, D.; Holler, F.; Crouch, S. *Principles of Instrumental Analysis*; Cengage Learning EMEA, 2017.

(126) Gnahore Guy Oscar, R.; Koffi, T.; Bagui, O.; Kouacou, A.; Kristensson, E.; Zoueu, J.; Berrocal, E. Quantitative Measurements of Turbid Liquids via Structured Laser Illumination Planar Imaging Where Absorption Spectrophotometry Fails. *Appl. Opt.* **2017**, *56*. https://doi.org/10.1364/AO.56.003929.

(127) Complete_FluoroLog3_Manual.Pdf.

(128) Cabanillas-Gonzalez, J.; Grancini, G.; Lanzani, G. Pump-Probe Spectroscopy in Organic Semiconductors: Monitoring Fundamental Processes of Relevance in Optoelectronics. *Adv. Mater.* **2011**, *23* (46), 5468–5485. https://doi.org/10.1002/adma.201102015.

(129) Berera, R.; van Grondelle, R.; Kennis, J. T. M. Ultrafast Transient Absorption Spectroscopy: Principles and Application to Photosynthetic Systems. *Photosynth. Res.* **2009**, *101* (2), 105–118. https://doi.org/10.1007/s11120-009-9454-y.

(130) Silfvast, W. T. *Laser Fundamentals*; Cambridge University Press, 2008.

(131) Einstein, A. Zur Quantentheorie Der Strahlung. *Phys. Z.* **1917**, *18*, 121–128.

(132) Keller, U. Recent Developments in Compact Ultrafast Lasers. *Nature* **2003**, *424* (6950), 831–838. https://doi.org/10.1038/nature01938.

(133) Kerr, J. XL. A New Relation between Electricity and Light: Dielectrified Media Birefringent. *Lond. Edinb. Dublin Philos. Mag. J. Sci.* **1875**, *50* (332), 337–348. https://doi.org/10.1080/14786447508641302.

(134) *PHAROS Femtosecond Lasers*. LIGHT CONVERSION. https://lightcon.com/product/pharos-femtosecond-lasers/ (accessed 2023-09-03).

(135) Grupp, A.; Budweg, A.; Fischer, M. P.; Allerbeck, J.; Soavi, G.; Leitenstorfer, A.; Brida, D. Broadly Tunable Ultrafast Pump-Probe System Operating at Multi-kHz Repetition Rate. *J. Opt.* **2017**, *20* (1), 014005. https://doi.org/10.1088/2040-8986/aa9b07.

(136) Strickland, D.; Mourou, G. Compression of Amplified Chirped Optical Pulses. *Opt. Commun.* **1985**, *55* (6), 447–449. https://doi.org/10.1016/0030-4018(85)90151-8.

(137) Weiner, A. M. Manipulation of Ultrashort Pulses. In *Ultrafast Optics*; John Wiley & Sons, Ltd, 2009; pp 362–421. https://doi.org/10.1002/9780470473467.ch8.

(138) ORPHEUS User's Manual.

(139) SX_Manual.Pdf.

(140) Ruckebusch, C.; Sliwa, M.; Pernot, P.; De Juan, A.; Tauler, R. Comprehensive Data Analysis of Femtosecond Transient Absorption Spectra: A Review. *J. Photochem. Photobiol. C Photochem. Rev.* **2012**, *13* (1), 1–27. https://doi.org/10.1016/j.jphotochemrev.2011.10.002.

(141) Van Stokkum, I. H. M.; Larsen, D. S.; Van Grondelle, R. Global and Target Analysis of Time-Resolved Spectra. *Biochim. Biophys. Acta - Bioenerg.* **2004**, *1657* (2–3), 82–104. https://doi.org/mu.

(142) *Glotaran: a tool for global and target analysis for time-resolved spectroscopy data*. https://glotaran.org/ (accessed 2024-04-06).

(143) Beechem, J. M. [2] Global Analysis of Biochemical and Biophysical Data. In *Methods in Enzymology*; Elsevier, 1992; Vol. 210, pp 37–54. https://doi.org/10.1016/0076-6879(92)10004-W.

(144) Snellenburg, J. J.; Laptenok, S.; Seger, R.; Mullen, K. M.; van Stokkum, I. H. M. Glotaran: A Java-Based Graphical User Interface for the R Package TIMP. *J. Stat. Softw.* **2012**, *49* (3), 1–22. https://doi.org/10.18637/jss.v049.i03.

(145) Hippius, C.; Van Stokkum, I. H. M.; Zangrando, E.; Williams, R. M.; Würthner, F. Excited State Interactions in Calix[4]arene−Perylene Bisimide Dye Conjugates: Global and Target Analysis of Supramolecular Building Blocks. *J. Phys. Chem. C* **2007**, *111* (37), 13988–13996. https://doi.org/10.1021/jp0733825.

(146) Rosendo, E. del P.; Yildiz, O.; Pisula, W.; Marszalek, T.; Blom, P. W. M.; Ramanan, C. Symmetry-Breaking Charge Transfer and Intersystem Crossing in Copper Phthalocyanine Thin Films. *Phys. Chem. Chem. Phys.* **2023**, *25* (9), 6847–6856. https://doi.org/10.1039/D2CP05240G.

(147) *Substance Information - ECHA*. https://echa.europa.eu/substance-information/-/substanceinfo/100.005.169 (accessed 2023-07-22).

(148) Shaibat, M. A.; Casabianca, L. B.; Siberio-Pérez, D. Y.; Matzger, A. J.; Ishii, Y. Distinguishing Polymorphs of the Semiconducting Pigment Copper Phthalocyanine by Solid-State NMR and Raman Spectroscopy. *J. Phys. Chem. B* **2010**, *114* (13), 4400–4406. https://doi.org/10.1021/jp9061412.

(149) Gregory, P. Industrial Applications of Phthalocyanines. *J. Porphyr. Phthalocyanines* **2000**, *04* (04), 432–437. https://doi.org/10.1002/(SICI)1099-1409(200006/07)4:4\textless432::AID-JPP254\textgreater3.0.CO;2-N.

(150) Braz, A.; López-López, M.; Montalvo, G.; Ruiz, C. G. Forensic Discrimination of Inkjet-Printed Lines by Raman Spectroscopy and Surface-Enhanced Raman Spectroscopy. *Aust. J. Forensic Sci.* **2014**.

(151) Simpson, W. T. On the Theory of the π-Electron System in Porphines. *J. Chem. Phys.* **2004**, *17* (12), 1218–1221. https://doi.org/10.1063/1.1747145.

(152) Danziger, J.; Lee, P.; Nebesny, K. W.; Armstrong, N. R.; Dodelet, J. P. Heterojunctions Formed from Phthalocyanine and Perylene Thin Films: Photoelectrochemical Characterization. *Chem. Mater.* **1991**, *3* (5), 821–829. https://doi.org/10.1021/cm00017a017.

(153) Peumans, P.; Forrest, S. R. Very-High-Efficiency Double-Heterostructure Copper Phthalocyanine/C-60 Photovoltaic Cells. *Appl. Phys. Lett.* **2001**, *79* (1), 126–128.

(154) Dutton, G. J.; Robey, S. W. Exciton Dynamics at CuPc/C 60 Interfaces: Energy Dependence of Exciton Dissociation. *J. Phys. Chem. C* **2012**, *116* (36), 19173–19181. https://doi.org/10.1021/jp305637r.

(155) Kim, I.; Haverinen, H. M.; Wang, Z.; Madakuni, S.; Kim, Y.; Li, J.; Jabbour, G. E. Efficient Organic Solar Cells Based on Planar Metallophthalocyanines. *Chem. Mater.* **2009**, *21* (18), 4256–4260. https://doi.org/10.1021/cm901320p.

(156) Snedden, E. W.; Monkman, A. P.; Dias, F. B. Photophysics of the Geminate Polaron-Pair State in Copper Phthalocyanine Organic Photovoltaic Blends: Evidence for Enhanced Intersystem Crossing. *Adv. Mater.* **2013**, *25* (13), 1930–1938. https://doi.org/10.1002/adma.201201350.

(157) Sasaki, T.; Tabata, K.; Tsukagoshi, K.; Beckel, A.; Lorke, A.; Yamamoto, Y. Control of Molecular Orientation and Morphology in Organic Bilayer Solar Cells: Copper Phthalocyanine on Gold Nanodots. *Thin Solid Films* **2014**, *562*, 467–470. https://doi.org/10.1016/j.tsf.2014.03.090.

(158) Cheng, C.-H.; Fan, Z.-Q.; Yu, S.-K.; Jiang, W.-H.; Wang, X.; Du, G.-T.; Chang, Y.-C.; Ma, C.-Y. 1.1μm near-Infrared Electrophosphorescence from Organic Light-Emitting Diodes Based on Copper Phthalocyanine. *Appl. Phys. Lett.* **2006**, *88* (21), 213505. https://doi.org/10.1063/1.2206678.

(159) El Ouedghiri-Idrissi, I.; Lougdali, M.; Makir, Z.; Niasse, O. A.; Sofiani, Z. Photoluminescence of Organic Thin Film Copper Phthalocyanine CuPc for LED Application. *Mater. Today Proc.* **2022**. https://doi.org/10.1016/j.matpr.2022.03.294.

(160) Mutz, N.; Park, S.; Schultz, T.; Sadofev, S.; Dalgleish, S.; Reissig, L.; Koch, N.; List-Kratochvil, E. J. W.; Blumstengel, S. Excited-State Charge Transfer Enabling MoS2/Phthalocyanine Photodetectors with Extended Spectral Sensitivity. *J. Phys. Chem. C* **2020**, *124* (5), 2837–2843. https://doi.org/10.1021/acs.jpcc.9b10877.

(161) Krishnan K, N.; Sreedharan, A.; Sagar, S.; Thomas Manamel, L.; Mukherjee, A.; Das, B. C. Self-Powered Broadband Photodetection of Copper Phthalocyanine by Enhancing Photogating Effect with Monolayer MoS2 Flakes. *Appl. Surf. Sci.* **2021**, *568*, 150818. https://doi.org/10.1016/J.APSUSC.2021.150818.

(162) Monama, G. R.; Modibane, K. D.; Ramohlola, K. E.; Molapo, K. M.; Hato, M. J.; Makhafola, M. D.; Mashao, G.; Mdluli, S. B.; Iwuoha, E. I. Copper(II) Phthalocyanine/Metal Organic Framework Electrocatalyst for Hydrogen Evolution Reaction Application. *Int. J. Hydrog. Energy* **2019**, *44* (34), 18891–18902. https://doi.org/10.1016/j.ijhydene.2019.02.052.

(163) Bian, J.; Sun, L.; Zhang, Z.; Li, Z.; Chu, M.; Li, X.; Tang, D.; Jing, L. Au-Modulated Z-Scheme CuPc/BiVO4 Nanosheet Heterojunctions toward Efficient CO2 Conversion under Wide-Visible-Light Irradiation. *ACS Sustain. Chem. Eng.* **2021**, *9* (5), 2400–2408. https://doi.org/10.1021/ACSSUSCHEMENG.0C09256.

(164) Gui, L.; Zhou, J.; Zhou, L.; Wei, S. A Smart Copper-Phthalocyanine Framework Nanoparticle for Enhancing Photodynamic Therapy in Hypoxic Conditions by Weakening Cells through ATP Depletion. *J. Mater. Chem. B* **2018**, *6* (14), 2078–2088. https://doi.org/10.1039/C8TB00334C.

(165) Abramczyk, H.; Szymczyk, I. Aggregation of Phthalocyanine Derivatives in Liquid Solutions and Human Blood. *J. Mol. Liq.* **2004**, *110* (1–3), 51–56. https://doi.org/10.1016/j.molliq.2003.08.017.

(166) Lo, P. C.; Rodríguez-Morgade, M. S.; Pandey, R. K.; Ng, D. K. P.; Torres, T.; Dumoulin, F. The Unique Features and Promises of Phthalocyanines as Advanced Photosensitisers for Photodynamic Therapy of Cancer. *Chem. Soc. Rev.* **2020**, *49* (4), 1041–1056. https://doi.org/10.1039/c9cs00129h.

(167) Cruickshank, A. C.; Dotzler, C. J.; Din, S.; Heutz, S.; Toney, M. F.; Ryan, M. P. The Crystalline Structure of Copper Phthalocyanine Films on ZnO(1Ī00). *J. Am. Chem. Soc.* **2012**, *134* (35), 14302–14305. https://doi.org/10.1021/ja305760b.

(168) Djurišić et al. - 2002 - Optical Properties of Copper Phthalocyanine-Annotated.Pdf.

(169) Maggioni, G.; Quaranta, A.; Carturan, S.; Patelli, A.; Tonezzer, M.; Ceccato, R.; Della Mea, G. Deposition of Copper Phthalocyanine Films by Glow-Discharge-Induced Sublimation. *Chem. Mater.* **2005**, *17* (7), 1895–1904. https://doi.org/10.1021/CM0487122/SUPPL_FILE/CM0487122SI20041105_092730.PDF.

(170) Heutz, S.; Bayliss, S. M.; Middleton, R. L.; Rumbles, G.; Jones, T. S. Polymorphism in Phthalocyanine Thin Films: Mechanism of the α → β Transition. *J. Phys. Chem. B* **2000**, *104* (30), 7124–7129. https://doi.org/10.1021/jp0000836.

(171) Berger, O.; Fischer, W.-J.; Adolphi, B.; Tierbach, S.; Melev, V.; Schreiber, J. Studies on Phase Transformations of Cu-Phthalocyanine Thin Films. *J. Mater. Sci. Mater. Electron.* **2000**, *11* (4), 331–346. https://doi.org/10.1023/A:1008933516940.

(172) E, J.; Kim, S.; Lim, E.; Lee, K.; Cha, D.; Friedman, B. Effects of Substrate Temperature on Copper(II) Phthalocyanine Thin Films. *Appl. Surf. Sci.* **2003**, *205* (1–4), 274–279. https://doi.org/10.1016/S0169-4332(02)01115-7.

(173) Lucia, E. A.; Verderame, F. D. Spectra of Polycrystalline Phthalocyanines in the Visible Region. *J. Chem. Phys.* **1968**, *48* (6), 2674–2681. https://doi.org/10.1063/1.1669501.

(174) Mullen, K. M.; Stokkum, I. H. M. van. TIMP : An R Package for Modeling Multi-Way Spectroscopic Measurements. *J. Stat. Softw.* **2007**, *18* (3), 1–46. https://doi.org/10.18637/jss.v018.i03.

(175) Claessens, C. G.; Hahn, U.; Torres, T. Phthalocyanines: From Outstanding Electronic Properties to Emerging Applications. *Chem. Rec.* **2008**, *8* (2), 75–97. https://doi.org/10.1002/tcr.20139.

(176) Sharp, J. H.; Abkowitz, M. Dimeric Structure of a Copper Phthalocyanine Polymorph. *J. Phys. Chem.* **1973**, *77* (4), 477–481. https://doi.org/10.1021/j100623a012.

(177) Zou, T.; Wang, X.; Ju, H.; Zhao, L.; Guo, T.; Wu, W.; Wang, H.; Zou, T.; Wang, X.; Ju, H.; Zhao, L.; Guo, T.; Wu, W.; Wang, H. Controllable Molecular Packing Motif and Overlap Type in Organic Nanomaterials for Advanced Optical Properties. *Crystals* **2018**, *8* (1), 22. https://doi.org/10.3390/cryst8010022.

(178) *Molecular Magnets: Physics and Applications*; Bartolomé, J., Luis, F., Fernández, J. F., Eds.; NanoScience and Technology; Springer Berlin Heidelberg: Berlin, Heidelberg, 2014.

(179) Zhang, X. F.; Xi, Q.; Zhao, J. Fluorescent and Triplet State Photoactive J-Type Phthalocyanine Nano Assemblies: Controlled Formation and Photosensitizing Properties. *J. Mater. Chem.* **2010**, *20* (32), 6726–6733. https://doi.org/10.1039/c0jm00695e.

(180) El-Nahass, M. M.; Bahabri, F. S.; Al Ghamdi, a a; Al-Harbi, S. R. Structural and Transport Properties of Copper Phthalocyanine (CuPc) Thin Films. *Egypt J Sol* **2002**, *25* (2), 307–321.

(181) Davidson, A. T. The Effect of the Metal Atom on the Absorption Spectra of Phthalocyanine Films. *J. Chem. Phys.* **1982**, *77* (1), 168–172. https://doi.org/10.1063/1.443636.

(182) Tokura, Y.; Koda, T.; Iyechika, Y.; Kuroda, H. Electro-Reflectance Spectra of Charge-Transfer Excitations in Copper Phthalocyanine Single Crystals. *Chem. Phys. Lett.* **1983**, *102* (2–3), 174–178. https://doi.org/10.1016/0009-2614(83)87387-4.

(183) Minami, N.; Asai, M. Photocurrent Spectra of Phthalocyanine Films in Relation to Excited State Properties. *Jpn. J. Appl. Phys.* **1987**, *26* (10 R), 1754–1758. https://doi.org/10.1143/JJAP.26.1754.

(184) Yadav, A.; Jin, Y.; Chan, P. K. L.; Shtein, M.; Pipe, K. P. Intermolecular Electronic Coupling in Organic Molecular Thin Films Measured by Temperature Modulation Spectroscopy. *Appl. Phys. Lett.* **2010**, *97* (20), 203307. https://doi.org/10.1063/1.3516040.

(185) McVie, J.; Sinclair, R. S.; Truscott, T. G. Triplet States of Copper and Metal-Free Phthalocyanines. *J. Chem. Soc. Faraday Trans. 2 Mol. Chem. Phys.* **1978**, *74*, 1870–1879. https://doi.org/10.1039/F29787401870.

(186) Caplins, B. W.; Mullenbach, T. K.; Holmes, R. J.; Blank, D. A. Femtosecond to Nanosecond Excited State Dynamics of Vapor Deposited Copper Phthalocyanine Thin Films. *Phys. Chem. Chem. Phys.* **2016**, *18* (16), 11454–11459. https://doi.org/10.1039/c6cp00958a.

(187) Frackowiak, D.; Planner, A.; Waszkowiak, A.; Boguta, A.; Ion, R. M.; Wiktorowicz, K. Yield of Intersystem (Singlet-Triplet) Crossing in Phthalocyanines Evaluated on the Basis of a Time in Resolved Photothermal Method. *J. Photochem. Photobiol. Chem.* **2001**, *141* (2–3), 101–108. https://doi.org/10.1016/S1010-6030(01)00438-5.

(188) Savolainen, J.; van der Linden, D.; Dijkhuizen, N.; Herek, J. L. Characterizing the Functional Dynamics of Zinc Phthalocyanine from Femtoseconds to Nanoseconds. *J. Photochem. Photobiol. Chem.* **2008**, *196* (1), 99–105. https://doi.org/10.1016/j.jphotochem.2007.11.018.

(189) Tran-Thi, T. H.; Lipskier, J. F.; Houde, D.; Pépin, C.; Keszei, E.; Jay-Gerin, J. P. Subpicosecond Excitation of Strongly Coupled Porphyrin–Phthalocyanine Mixed Dimers. *J. Chem. Soc. Faraday Trans.* **1992**, *88* (15), 2129–2137. https://doi.org/10.1039/FT9928802129.

(190) Nikolaitchik, A. V. Crown Ether Substituted Monomeric and Cofacial Dimeric Metallophthalocyanines. 1. Photophysical Studies of the Free Base, Zinc(II), and Copper(II) Variants. *J. Phys. Chem. A* **1999**, *103* (38), 7587–7596. https://doi.org/10.1021/jp9911651.

(191) Eastwood, D.; Edwards, L.; Gouterman, M.; Steinfeld, J. Spectra of Porphyrins: Part VII. Vapor Absorption and Emission of Phthalocyanines. *J. Mol. Spectrosc.* **1966**, *20* (4), 381–390. https://doi.org/10.1016/0022-2852(66)90009-9.

(192) Vincett, P. S.; Voigt, E. M.; Rieckhoff, K. E. Phosphorescence and Fluorescence of Phthalocyanines. *J. Chem. Phys.* **1971**, *55* (8), 4127–4131. https://doi.org/10.1063/1.1676714.

(193) Yoshino, K.; Hikida, M.; Tatsuno, K.; Kaneto, K.; Inuishi, Y. Emission Spectra of Phthalocyanine Crystals. *J. Phys. Soc. Jpn.* **1973**, *34* (2), 441–445. https://doi.org/10.1143/JPSJ.34.441.

(194) Iagatti, A.; Doria, S.; Marcelli, A.; Angelini, N.; Notarantonio, S.; Paoletti, A. M.; Pennesi, G.; Rossi, G.; Zanotti, G.; Calogero, G.; Foggi, P. Photophysical Processes Occurring in

a Zn-Phthalocyanine in Ethanol Solution and on TiO_2 Nanostructures. *J. Phys. Chem. C* **2015**, *119* (35), 20256–20264. https://doi.org/10.1021/acs.jpcc.5b04978.

(195) Doria, S.; Lapini, A.; Donato, M. D.; Righini, R.; Azzaroli, N.; Iagatti, A.; Caram, J. R.; Sinclair, T. S.; Cupellini, L.; Jurinovich, S.; Mennucci, B.; Zanotti, G.; Paoletti, A. M.; Pennesi, G.; Foggi, P. Understanding the Influence of Disorder on the Exciton Dynamics and Energy Transfer in Zn-Phthalocyanine H-Aggregates. *Phys. Chem. Chem. Phys.* **2018**, *20* (34), 22331–22341. https://doi.org/10.1039/C8CP02172D.

(196) Uemura, T.; Furumoto, M.; Nakano, T.; Akai-Kasaya, M.; Saito, A.; Aono, M.; Kuwahara, Y. Local-Plasmon-Enhanced up-Conversion Fluorescence from Copper Phthalocyanine. *Chem. Phys. Lett.* **2007**, *448* (4–6), 232–236. https://doi.org/10.1016/j.cplett.2007.09.084.

(197) Okada, A.; Kanazawa, K.; Hayashi, K.; Okawa, N.; Kurita, T.; Takeuchi, O.; Shigekawa, H. Anomalous Light Emission from Metal Phthalocyanine Films on Au(111) Activated by Tunneling-Current-Induced Surface Plasmon. *Appl. Phys. Express* **2010**, *3* (1), 015201. https://doi.org/10.1143/APEX.3.015201.

(198) Albert-Seifried, S.; Friend, R. H. Measurement of Thermal Modulation of Optical Absorption in Pump-Probe Spectroscopy of Semiconducting Polymers. *Appl. Phys. Lett.* **2011**, *98* (22), 223304. https://doi.org/10.1063/1.3595340.

(199) Ichikawa, M.; Fukumura, H.; Masuhara, H. Picosecond Regular Reflection Spectroscopic Study on Ultrafast Photoinduced Heat Generation in Copper Phthalocyanine Solid. *J. Phys. Chem.* **1994**, *98* (47), 12211–12214. https://doi.org/10.1021/j100098a015.

(200) Ma, Y. Z.; Xiao, K.; Shaw, R. W. Exciton-Exciton Annihilation in Copper-Phthalocyanine Single-Crystal Nanowires. *J. Phys. Chem. C* **2012**, *116* (40), 21588–21593. https://doi.org/10.1021/jp3057543.

(201) Padgaonkar, S.; Amsterdam, S. H.; Bergeron, H.; Su, K.; Marks, T. J.; Hersam, M. C.; Weiss, E. A. Molecular-Orientation-Dependent Interfacial Charge Transfer in Phthalocyanine/MoS 2 Mixed-Dimensional Heterojunctions. *J. Phys. Chem. C* **2019**, *123* (21), 13337–13343. https://doi.org/10.1021/acs.jpcc.9b04063.

(202) Cacioppo, M.; Scharl, T.; Đorđević, L.; Cadranel, A.; Arcudi, F.; Guldi, D. M.; Prato, M. Symmetry-Breaking Charge-Transfer Chromophore Interactions Supported by Carbon Nanodots. *Angew. Chem. - Int. Ed.* **2020**, *59* (31), 12779–12784. https://doi.org/10.1002/anie.202004638.

(203) Liao, M. S.; Scheiner, S. Electronic Structure and Bonding in Metal Phthalocyanines, metal=Fe, Co, Ni, Cu, Zn, Mg. *J. Chem. Phys.* **2001**, *114* (22), 9780–9791. https://doi.org/10.1063/1.1367374.

(204) Ha-Thi, M. H.; Shafizadeh, N.; Poisson, L.; Soep, B. An Efficient Indirect Mechanism for the Ultrafast Intersystem Crossing in Copper Porphyrins. *J. Phys. Chem. A* **2013**, *117* (34), 8111–8118. https://doi.org/10.1021/jp4008015.

(205) Wu, W. Exchange Interaction between the Triplet Exciton and the Localized Spin in Copper-Phthalocyanine. *J. Chem. Phys.* **2014**, *140* (22), 224301. https://doi.org/10.1063/1.4881897.

(206) Lozzi, L.; Santucci, S.; La Rosa, S.; Delley, B.; Picozzi, S. Electronic Structure of Crystalline Copper Phthalocyanine. *J. Chem. Phys.* **2004**, *121* (4), 1883–1889. https://doi.org/10.1063/1.1766295.

(207) Caplins, B. W.; Mullenbach, T. K.; Holmes, R. J.; Blank, D. A. Intermolecular Interactions Determine Exciton Lifetimes in Neat Films and Solid State Solutions of Metal-Free Phthalocyanine. *J. Phys. Chem. C* **2015**, *119* (49), 27340–27347. https://doi.org/10.1021/acs.jpcc.5b09817.

(208) Hirasawa, M.; Sakazaki, Y.; Hane, H.; Kobayashi, T. Direct Observation of Vibrational Dynamics in Tin Phthalocyanine. *Chem. Phys. Lett.* **2004**, *392* (4–6), 390–395. https://doi.org/10.1016/j.cplett.2004.03.154.

(209) Lin, C.; Kim, T.; Schultz, J. D.; Young, R. M.; Wasielewski, M. R. Accelerating Symmetry-Breaking Charge Separation in a Perylenediimide Trimer through a Vibronically Coherent Dimer Intermediate. *Nat. Chem. 2022* **2022**, 1–8. https://doi.org/10.1038/S41557-022-00927-Y.

(210) Tsushima, M.; Ikeda, N.; Yonehara, H.; Etori, H.; Pac, C.; Ohno, T. A Charge-Separated Pair in Thin Crystals of Oxotitanium(IV) Phthalocyanine Revealed by Means of Femtosecond Time-Resolved Absorption. *Coord. Chem. Rev.* **2002**, *229* (1–2), 3–8. https://doi.org/10.1016/S0010-8545(02)00103-0.

(211) Mi, J.; Guo, L.; Liu, Y.; Liu, W.; You, G.; Qian, S. Excited-State Dynamics of Magnesium Phthalocyanine Thin Film. *Phys. Lett. Sect. Gen. At. Solid State Phys.* **2003**, *310* (5–6), 486–492. https://doi.org/10.1016/S0375-9601(03)00458-4.

(212) Aster, A.; Licari, G.; Zinna, F.; Brun, E.; Kumpulainen, T.; Tajkhorshid, E.; Lacour, J.; Vauthey, E. Tuning Symmetry Breaking Charge Separation in Perylene Bichromophores by Conformational Control. *Chem. Sci.* **2019**, *10* (45), 10629–10639. https://doi.org/10.1039/c9sc03913a.

(213) Sebastian, E.; Hariharan, M. Symmetry-Breaking Charge Separation in Molecular Constructs for Efficient Light Energy Conversion. *ACS Energy Lett.* **2022**, *44*, 696–711. https://doi.org/10.1021/ACSENERGYLETT.1C02412.

(214) Smith, M. B.; Michl, J. Singlet Fission. *Chem. Rev.* **2010**, *110* (11), 6891–6936. https://doi.org/10.1021/cr1002613.

(215) Smith, M. B.; Michl, J. Recent Advances in Singlet Fission. *Annu. Rev. Phys. Chem.* **2013**, *64* (1), 361–386. https://doi.org/10.1146/annurev-physchem-040412-110130.

(216) Monahan, N.; Zhu, X.-Y. Charge Transfer–Mediated Singlet Fission. *Annu. Rev. Phys. Chem.* **2015**, *66* (1), 601–618. https://doi.org/10.1146/annurev-physchem-040214-121235.

(217) Mirjani, F.; Renaud, N.; Gorczak, N.; Grozema, F. C. Theoretical Investigation of Singlet Fission in Molecular Dimers: The Role of Charge Transfer States and Quantum Interference. *J. Phys. Chem. C* **2014**, *118* (26), 14192–14199. https://doi.org/10.1021/jp503398a.

(218) Felter, K. M.; Grozema, F. C. Singlet Fission in Crystalline Organic Materials: Recent Insights and Future Directions. *J. Phys. Chem. Lett.* **2019**, *10* (22), 7208–7214. https://doi.org/10.1021/acs.jpclett.9b00754.

(219) Renaud, N.; Grozema, F. C. Intermolecular Vibrational Modes Speed Up Singlet Fission in Perylenediimide Crystals. *J. Phys. Chem. Lett.* **2015**, *6* (3), 360–365. https://doi.org/10.1021/jz5023575.

(220) Wu, T.; Ni, W.; Gurzadyan, G. G.; Sun, L. Singlet Fission from Upper Excited Singlet States and Polaron Formation in Rubrene Film. *RSC Adv.* **2021**, *11* (8), 4639–4645. https://doi.org/10.1039/D0RA10780H.

(221) Singh, S.; Jones, W. J.; Siebrand, W.; Stoicheff, B. P.; Schneider, W. G. Laser Generation of Excitions and Fluorescence in Anthracene Crystals. *J. Chem. Phys.* **1965**, *42*, 330–342. https://doi.org/10.1063/1.1695695.

(222) Shockley, W.; Queisser, H. J. Detailed Balance Limit of Efficiency of *p-n* Junction Solar Cells. *J. Appl. Phys.* **1961**, *32* (3), 510–519. https://doi.org/10.1063/1.1736034.

(223) Lee, J.; Jadhav, P.; Reusswig, P. D.; Yost, S. R.; Thompson, N. J.; Congreve, D. N.; Hontz, E.; Van Voorhis, T.; Baldo, M. A. Singlet Exciton Fission Photovoltaics. *Acc. Chem. Res.* **2013**, *46* (6), 1300–1311. https://doi.org/10.1021/ar300288e.

(224) Hanna, M. C.; Nozik, A. J. Solar Conversion Efficiency of Photovoltaic and Photoelectrolysis Cells with Carrier Multiplication Absorbers. *J. Appl. Phys.* **2006**, *100* (7), 074510. https://doi.org/10.1063/1.2356795.

(225) Le, A. K.; Bender, J. A.; Roberts, S. T. Slow Singlet Fission Observed in a Polycrystalline Perylenediimide Thin Film. *J. Phys. Chem. Lett.* **2016**, *7* (23), 4922–4928. https://doi.org/10.1021/acs.jpclett.6b02320.

(226) Hartnett, P. E.; Margulies, E. A.; Mauck, C. M.; Miller, S. A.; Wu, Y.; Wu, Y.-L.; Marks, T. J.; Wasielewski, M. R. Effects of Crystal Morphology on Singlet Exciton Fission in Diketopyrrolopyrrole Thin Films. *J. Phys. Chem. B* **2016**, *120* (7), 1357–1366. https://doi.org/10.1021/acs.jpcb.5b10565.

(227) Ramanan, C.; Smeigh, A. L.; Anthony, J. E.; Marks, T. J.; Wasielewski, M. R. Competition between Singlet Fission and Charge Separation in Solution-Processed Blend Films of 6,13-Bis(Triisopropylsilylethynyl)Pentacene with Sterically-Encumbered Perylene-3,4:9,10-Bis(Dicarboximide)s. *J. Am. Chem. Soc.* **2012**, *134* (1), 386–397. https://doi.org/10.1021/ja2080482.

(228) Eaton, S. W.; Shoer, L. E.; Karlen, S. D.; Dyar, S. M.; Margulies, E. A.; Veldkamp, B. S.; Ramanan, C.; Hartzler, D. A.; Savikhin, S.; Marks, T. J.; Wasielewski, M. R. Singlet Exciton Fission in Polycrystalline Thin Films of a Slip-Stacked Perylenediimide. *J. Am. Chem. Soc.* **2013**, *135* (39), 14701–14712. https://doi.org/10.1021/ja4053174.

(229) Chen, M.; Bae, Y. J.; Mauck, C. M.; Mandal, A.; Young, R. M.; Wasielewski, M. R. Singlet Fission in Covalent Terrylenediimide Dimers: Probing the Nature of the Multiexciton State Using Femtosecond Mid-Infrared Spectroscopy. *J. Am. Chem. Soc.* **2018**, *140* (29), 9184–9192. https://doi.org/10.1021/jacs.8b04830.

(230) Schuster, R.; Knupfer, M.; Berger, H. Exciton Band Structure of Pentacene Molecular Solids: Breakdown of the Frenkel Exciton Model. *Phys. Rev. Lett.* **2007**, *98* (3), 037402. https://doi.org/10.1103/PhysRevLett.98.037402.

(231) Sanders, S. N.; Kumarasamy, E.; Pun, A. B.; Trinh, M. T.; Choi, B.; Xia, J.; Taffet, E. J.; Low, J. Z.; Miller, J. R.; Roy, X.; Zhu, X.-Y.; Steigerwald, M. L.; Sfeir, M. Y.; Campos, L. M. Quantitative Intramolecular Singlet Fission in Bipentacenes. *J. Am. Chem. Soc.* **2015**, *137* (28), 8965–8972. https://doi.org/10.1021/jacs.5b04986.

(232) Yamagata, H.; Norton, J.; Hontz, E.; Olivier, Y.; Beljonne, D.; Brédas, J. L.; Silbey, R. J.; Spano, F. C. The Nature of Singlet Excitons in Oligoacene Molecular Crystals. *J. Chem. Phys.* **2011**, *134* (20), 204703. https://doi.org/10.1063/1.3590871.

(233) Alam, B.; Morrison, A. F.; Herbert, J. M. Charge Separation and Charge Transfer in the Low-Lying Excited States of Pentacene. *J. Phys. Chem. C* **2020**, *124* (45), 24653–24666. https://doi.org/10.1021/acs.jpcc.0c07932.

(234) Broch, K.; Dieterle, J.; Branchi, F.; Hestand, N. J.; Olivier, Y.; Tamura, H.; Cruz, C.; Nichols, V. M.; Hinderhofer, A.; Beljonne, D.; Spano, F. C.; Cerullo, G.; Bardeen, C. J.; Schreiber, F. Robust Singlet Fission in Pentacene Thin Films with Tuned Charge Transfer Interactions. *Nat. Commun.* **2018**, *9* (1), 954. https://doi.org/10.1038/s41467-018-03300-1.

(235) Rao, A.; Friend, R. H. Harnessing Singlet Exciton Fission to Break the Shockley–Queisser Limit. *Nat. Rev. Mater.* **2017**, *2* (11), 17063. https://doi.org/10.1038/natrevmats.2017.63.

(236) Greyson, E. C.; Vura-Weis, J.; Michl, J.; Ratner, M. A. Maximizing Singlet Fission in Organic Dimers: Theoretical Investigation of Triplet Yield in the Regime of Localized Excitation and Fast Coherent Electron Transfer. *J. Phys. Chem. B* **2010**, *114* (45), 14168–14177. https://doi.org/10.1021/jp907392q.

(237) Teichen, P. E.; Eaves, J. D. A Microscopic Model of Singlet Fission. *J. Phys. Chem. B* **2012**, *116* (37), 11473–11481. https://doi.org/10.1021/jp208905k.

(238) Johnson, J. C.; Nozik, A. J.; Michl, J. High Triplet Yield from Singlet Fission in a Thin Film of 1,3-Diphenylisobenzofuran. *J. Am. Chem. Soc.* **2010**, *132* (46), 16302–16303. https://doi.org/10.1021/ja104123r.

(239) Pope, M.; Geacintov, N. E.; Vogel, F. Singlet Exciton Fission and Tri Plet-Tri Plet Exciton Fusion in Crystalline Tet Racene. *Mol. Cryst.* **1969**, *6* (1), 83–104. https://doi.org/10.1080/15421406908082953.

(240) Rao, A.; Wilson, M. W. B.; Albert-Seifried, S.; Di Pietro, R.; Friend, R. H. Photophysics of Pentacene Thin Films: The Role of Exciton Fission and Heating Effects. *Phys. Rev. B* **2011**, *84* (19), 195411. https://doi.org/10.1103/PhysRevB.84.195411.

(241) Casanova, D. Theoretical Modeling of Singlet Fission. *Chem. Rev.* **2018**, *118* (15), 7164–7207. https://doi.org/10.1021/acs.chemrev.7b00601.

(242) Burdett, J. J.; Müller, A. M.; Gosztola, D.; Bardeen, C. J. Excited State Dynamics in Solid and Monomeric Tetracene: The Roles of Superradiance and Exciton Fission. *J. Chem. Phys.* **2010**, *133* (14), 144506. https://doi.org/10.1063/1.3495764.

(243) Burdett, J. J.; Gosztola, D.; Bardeen, C. J. The Dependence of Singlet Exciton Relaxation on Excitation Density and Temperature in Polycrystalline Tetracene Thin Films: Kinetic

Evidence for a Dark Intermediate State and Implications for Singlet Fission. *J. Chem. Phys.* **2011**, *135* (21), 214508. https://doi.org/10.1063/1.3664630.

(244) Busby, E.; Xia, J.; Wu, Q.; Low, J. Z.; Song, R.; Miller, J. R.; Zhu, X.-Y.; Campos, L. M.; Sfeir, M. Y. A Design Strategy for Intramolecular Singlet Fission Mediated by Charge-Transfer States in Donor–Acceptor Organic Materials. *Nat. Mater.* **2015**, *14* (4), 426–433. https://doi.org/10.1038/nmat4175.

(245) Trinh, M. T.; Zhong, Y.; Chen, Q.; Schiros, T.; Jockusch, S.; Sfeir, M. Y.; Steigerwald, M.; Nuckolls, C.; Zhu, X. Intra- to Intermolecular Singlet Fission. *J. Phys. Chem. C* **2015**, *119* (3), 1312–1319. https://doi.org/10.1021/jp512650g.

(246) Kaczmarek-Kędziera, A.; Ośmiałowski, B.; Żuchowski, P. S.; Kędziera, D. Supramolecular Approach to Tuning the Photophysical Properties of Quadrupolar Squaraines. *Front. Chem.* **2022**, *9*.

(247) Tong, L.; Bixian, P. The In¯uence of N-Alkyl Groups on the Properties of Squarylium Cyanine Dyes.

(248) Zheng, C.; Zhong, C.; Collison, C. J.; Spano, F. C. Non-Kasha Behavior in Quadrupolar Dye Aggregates: The Red-Shifted H-Aggregate. *J. Phys. Chem. C* **2019**, *123* (5), 3203–3215. https://doi.org/10.1021/acs.jpcc.8b11416.

(249) Treibs, A.; Jacob, K. Von Der Quadratsäure Abgeleitete Cyclotrimethinfarbstoffe. *Angew. Chem.* **1965**, *77* (15), 680–681. https://doi.org/10.1002/ange.19650771509.

(250) Beverina, L.; Salice, P. Squaraine Compounds: Tailored Design and Synthesis towards a Variety of Material Science Applications. *Eur. J. Org. Chem.* **2010**, *2010* (7), 1207–1225. https://doi.org/10.1002/ejoc.200901297.

(251) Timmer, D.; Zheng, F.; Gittinger, M.; Quenzel, T.; Lünemann, D. C.; Winte, K.; Zhang, Y.; Madjet, M. E.; Zablocki, J.; Lützen, A.; Zhong, J.-H.; De Sio, A.; Frauenheim, T.; Tretiak, S.; Lienau, C. Charge Delocalization and Vibronic Couplings in Quadrupolar Squaraine Dyes. *J. Am. Chem. Soc.* **2022**, *144* (41), 19150–19162. https://doi.org/10.1021/jacs.2c08682.

(252) Balzer, F.; Kollmann, H.; Schulz, M.; Schnakenburg, G.; Lützen, A.; Schmidtmann, M.; Lienau, C.; Silies, M.; Schiek, M. Spotlight on Excitonic Coupling in Polymorphic and Textured Anilino Squaraine Thin Films. *Cryst. Growth Des.* **2017**, *17* (12), 6455–6466. https://doi.org/10.1021/acs.cgd.7b01131.

(253) Freese, S.; Lässing, P.; Jakob, R.; Schulz, M.; Lützen, A.; Schiek, M.; Nilius, N. Photoluminescence of Squaraine Thin Films: Spatial Homogeneity and Temperature Dependence. *Phys. Status Solidi B* **2019**, *256* (3), 1800450. https://doi.org/10.1002/pssb.201800450.

(254) Das, S.; Thomas, K. G.; Kamat, P. V.; George, M. V. Photosensitizing Properties of Squaraine Dyes. *J. Chem. Sci.* **1993**, *105* (6), 513–525. https://doi.org/10.1007/BF03040823.

(255) Bernhardt, R.; Manrho, M.; Zablocki, J.; Rieland, L.; Lützen, A.; Schiek, M.; Meerholz, K.; Zhu, J.; Jansen, T. L. C.; Knoester, J.; Van Loosdrecht, P. H. M. Structural Disorder as the Origin of Optical Properties and Spectral Dynamics in Squaraine Nano-Aggregates. *J. Am. Chem. Soc.* **2022**, *144* (42), 19372–19381. https://doi.org/10.1021/jacs.2c07064.

(256) Hestand, N. J.; Zheng, C.; Penmetcha, A. R.; Cona, B.; Cody, J. A.; Spano, F. C.; Collison, C. J. Confirmation of the Origins of Panchromatic Spectra in Squaraine Thin Films Targeted for Organic Photovoltaic Devices. *J. Phys. Chem. C* **2015**, *119* (33), 18964–18974. https://doi.org/10.1021/acs.jpcc.5b05095.

(257) Chen, G.; Sasabe, H.; Sasaki, Y.; Katagiri, H.; Wang, X.-F.; Sano, T.; Hong, Z.; Yang, Y.; Kido, J. A Series of Squaraine Dyes: Effects of Side Chain and the Number of Hydroxyl Groups on Material Properties and Photovoltaic Performance. *Chem. Mater.* **2014**, *26* (3), 1356–1364. https://doi.org/10.1021/cm4034929.

(258) Dirk, C. W.; Herndon, W. C.; Cervantes-Lee, F.; Selnau, H.; Martinez, S.; Kalamegham, P.; Tan, A.; Campos, G.; Velez, M. Squarylium Dyes: Structural Factors Pertaining to the Negative Third-Order Nonlinear Optical Response. *J. Am. Chem. Soc.* **1995**, *117* (8), 2214–2225. https://doi.org/10.1021/ja00113a011.

(259) Brück, S.; Krause, C.; Turrisi, R.; Beverina, L.; Wilken, S.; Saak, W.; Lützen, A.; Borchert, H.; Schiek, M.; Parisi, J. Structure–Property Relationship of Anilino-Squaraines in Organic Solar Cells. *Phys. Chem. Chem. Phys.* **2013**, *16* (3), 1067–1077. https://doi.org/10.1039/C3CP54163K.

(260) Zablocki, J.; Schulz, M.; Schnakenburg, G.; Beverina, L.; Warzanowski, P.; Revelli, A.; Grüninger, M.; Balzer, F.; Meerholz, K.; Lützen, A.; Schiek, M. Structure and Dielectric Properties of Anisotropic *n* -Alkyl Anilino Squaraine Thin Films. *J. Phys. Chem. C* **2020**, *124* (41), 22721–22732. https://doi.org/10.1021/acs.jpcc.0c07498.

(261) Law, K.-Y. Squaraine Chemistry: Effects of Solvent and Temperature on the Fluorescence Emission of Squaraines. *J. Photochem. Photobiol. Chem.* **1994**, *84* (2), 123–132. https://doi.org/10.1016/1010-6030(94)03849-X.

(262) Kamat, P. V.; Das, S.; Thomas, K. G.; George, M. V. Photochemistry of Squaraine Dyes. 1. Excited Singlet, Triplet, and Redox States of Bis[4-(Dimethylamino)Phenyl]Squaraine and Bis[4-(Dimethylamino)-2-Hydroxyphenyl]Squaraine. *J. Phys. Chem.* **1992**, *96* (1), 195–199. https://doi.org/10.1021/j100180a038.

(263) Zheng, C.; Bleier, D.; Jalan, I.; Pristash, S.; Penmetcha, A. R.; Hestand, N. J.; Spano, F. C.; Pierce, M. S.; Cody, J. A.; Collison, C. J. Phase Separation, Crystallinity and Monomer-Aggregate Population Control in Solution Processed Small Molecule Solar Cells. *Sol. Energy Mater. Sol. Cells* **2016**, *157*, 366–376. https://doi.org/10.1016/j.solmat.2016.05.060.

(264) Zheng, C.; Mark, M. F.; Wiegand, T.; Diaz, S. A.; Cody, J.; Spano, F. C.; McCamant, D. W.; Collison, C. J. Measurement and Theoretical Interpretation of Exciton Diffusion as a Function of Intermolecular Separation for Squaraines Targeted for Bulk Heterojunction Solar Cells. *J. Phys. Chem. C* **2020**, *124* (7), 4032–4043. https://doi.org/10.1021/acs.jpcc.9b11816.

(265) Schreck, M. H.; Breitschwerdt, L.; Marciniak, H.; Holzapfel, M.; Schmidt, D.; Würthner, F.; Lambert, C. Fs–Ps Exciton Dynamics in a Stretched Tetraphenylsquaraine Polymer. *Phys. Chem. Chem. Phys.* **2019**, *21* (28), 15346–15355. https://doi.org/10.1039/C9CP02900A.

(266) Brück, S.; Krause, C.; Turrisi, R.; Beverina, L.; Wilken, S.; Saak, W.; Lützen, A.; Borchert, H.; Schiek, M.; Parisi, J. Structure–Property Relationship of Anilino-Squaraines in Organic Solar Cells. *Phys Chem Chem Phys* **2014**, *16* (3), 1067–1077. https://doi.org/10.1039/C3CP54163K.

(267) Chen, G.; Sasabe, H.; Sasaki, Y.; Katagiri, H.; Wang, X.-F.; Sano, T.; Hong, Z.; Yang, Y.; Kido, J. A Series of Squaraine Dyes: Effects of Side Chain and the Number of Hydroxyl Groups on Material Properties and Photovoltaic Performance. *Chem. Mater.* **2014**, *26* (3), 1356–1364. https://doi.org/10.1021/cm4034929.

(268) Zheng, C.; Penmetcha, A. R.; Cona, B.; Spencer, S. D.; Zhu, B.; Heaphy, P.; Cody, J. A.; Collison, C. J. Contribution of Aggregate States and Energetic Disorder to a Squaraine System Targeted for Organic Photovoltaic Devices. *Langmuir* **2015**, *31* (28), 7717–7726. https://doi.org/10.1021/acs.langmuir.5b01045.

(269) Zheng, C.; Jalan, I.; Cost, P.; Oliver, K.; Gupta, A.; Misture, S.; Cody, J. A.; Collison, C. J. Impact of Alkyl Chain Length on Small Molecule Crystallization and Nanomorphology in Squaraine-Based Solution Processed Solar Cells. *J. Phys. Chem. C* **2017**, *121* (14), 7750–7760. https://doi.org/10.1021/acs.jpcc.7b01339.

(270) Lambert, C.; Hoche, J.; Schreck, M. H.; Holzapfel, M.; Schmiedel, A.; Selby, J.; Turkin, A.; Mitric, R. Ultrafast Energy Transfer Dynamics in a Squaraine Heterotriad. *J. Phys. Chem. A* **2021**, *125* (12), 2504–2511. https://doi.org/10.1021/acs.jpca.1c00349.

(271) De Miguel, G.; Marchena, M.; Zitnan, M.; Pandey, S. S.; Hayase, S.; Douhal, A. Femto to Millisecond Observations of Indole-Based Squaraine Molecules Photodynamics in Solution. *Phys Chem Chem Phys* **2012**, *14* (5), 1796–1805. https://doi.org/10.1039/C1CP22864A.

(272) Timmer, D.; Zheng, F.; Gittinger, M.; Quenzel, T.; Lünemann, D. C.; Winte, K.; Zhang, Y.; Madjet, M. E.; Zablocki, J.; Lützen, A.; Zhong, J.-H.; De Sio, A.; Frauenheim, T.; Tretiak, S.; Lienau, C. Charge Delocalization and Vibronic Couplings in Quadrupolar Squaraine Dyes. *J. Am. Chem. Soc.* **2022**, *144* (41), 19150–19162. https://doi.org/10.1021/jacs.2c08682.

(273) Law, K.-Y. Origin of the Multiple Fluorescence Emission of Unsymmetrical Squaraines. *Chem. Phys. Lett.* **1992**, *200* (1–2), 121–124. https://doi.org/10.1016/0009-2614(92)87055-T.

(274) Spano, F. C. The Spectral Signatures of Frenkel Polarons in H- and J-Aggregates. *Acc. Chem. Res.* **2010**, *43* (3), 429–439. https://doi.org/10.1021/ar900233v.

(275) Aulin, Y. V.; Felter, K. M.; Günbas, D. D.; Dubey, R. K.; Jager, W. F.; Grozema, F. C. Morphology-Independent Efficient Singlet Exciton Fission in Perylene Diimide Thin Films. *ChemPlusChem* **2018**, *83* (4), 230–238. https://doi.org/10.1002/cplu.201700449.

(276) Pun, A.; Asadpoordarvish, A.; Kumarasamy, E.; Tayebjee, M.; Niesner, D.; McCamey, D.; Sanders, S.; Campos, L.; Sfeir, M. Ultra-Fast Intramolecular Singlet Fission to Persistent Multiexcitons by Molecular Design. *Nat. Chem.* **2019**, *11*. https://doi.org/10.1038/s41557-019-0297-7.

(277) Sun, D.; Deng, G.-H.; Xu, B.; Xu, E.; Li, X.; Wu, Y.; Qian, Y.; Zhong, Y.; Nuckolls, C.; Harutyunyan, A. R.; Dai, H.-L.; Chen, G.; Chen, H.; Rao, Y. Anisotropic Singlet Fission in Single Crystalline Hexacene. *iScience* **2019**, *19*, 1079–1089. https://doi.org/10.1016/j.isci.2019.08.053.

(278) Conrad-Burton, F. S.; Liu, T.; Geyer, F.; Costantini, R.; Schlaus, A. P.; Spencer, M. S.; Wang, J.; Sánchez, R. H.; Zhang, B.; Xu, Q.; Steigerwald, M. L.; Xiao, S.; Li, H.; Nuckolls, C. P.; Zhu, X. Controlling Singlet Fission by Molecular Contortion. *J. Am. Chem. Soc.* **2019**, *141* (33), 13143–13147. https://doi.org/10.1021/jacs.9b05357.

(279) Borrego-Varillas, R.; Ganzer, L.; Cerullo, G.; Manzoni, C. Ultraviolet Transient Absorption Spectrometer with Sub-20-Fs Time Resolution. *Appl. Sci.* **2018**, *8* (6), 989. https://doi.org/10.3390/app8060989.

(280) Wei, Z.; Li, J.; Wang, L.; See, S.; Jhon, M.; Zhang, Y.; Shi, F.; Yang, M.; Loh, Z.-H. Elucidating the Origins of Multimode Vibrational Coherences of Polyatomic Molecules Induced by Intense Laser Fields. *Nat. Commun.* **2017**, *8*. https://doi.org/10.1038/s41467-017-00848-2.

(281) Nenov, A.; Borrego-Varillas, R.; Oriana, A.; Ganzer, L.; Segatta, F.; Conti, I.; Segarra-Marti, J.; Omachi, J.; Dapor, M.; Taioli, S.; Manzoni, C.; Mukamel, S.; Cerullo, G.; Garavelli, M. UV-Light-Induced Vibrational Coherences: The Key to Understand Kasha Rule Violation in *Trans* -Azobenzene. *J. Phys. Chem. Lett.* **2018**, *9* (7), 1534–1541. https://doi.org/10.1021/acs.jpclett.8b00152.

(282) Hu, D.; Peng, J.; Chen, L.; Gelin, M. F.; Lan, Z. Spectral Fingerprint of Excited-State Energy Transfer in Dendrimers through Polarization-Sensitive Transient-Absorption Pump–Probe Signals: On-the-Fly Nonadiabatic Dynamics Simulations. *J. Phys. Chem. Lett.* **2021**, *12* (39), 9710–9719. https://doi.org/10.1021/acs.jpclett.1c02640.

(283) Polli, D.; Brida, D.; Mukamel, S.; Lanzani, G.; Cerullo, G. Effective Temporal Resolution in Pump-Probe Spectroscopy with Strongly Chirped Pulses. *Phys. Rev. A* **2010**, *82* (5), 053809. https://doi.org/10.1103/PhysRevA.82.053809.

(284) Mehata, M. S.; Yang, Y.; Han, K. Probing Charge-Transfer and Short-Lived Triplet States of a Biosensitive Molecule, 2,6-ANS: Transient Absorption and Time-Resolved Spectroscopy. *ACS Omega* **2017**, *2* (10), 6782–6785. https://doi.org/10.1021/acsomega.7b00921.

(285) Slavov, C.; Bellakbil, N.; Wahl, J.; Mayer, K.; Rück-Braun, K.; Burghardt, I.; Wachtveitl, J.; Braun, M. Ultrafast Coherent Oscillations Reveal a Reactive Mode in the Ring-Opening Reaction of Fulgides. *Phys. Chem. Chem. Phys.* **2015**, *17* (21), 14045–14053. https://doi.org/10.1039/C5CP01878A.

(286) Siewertsen, R.; Strübe, F.; Mattay, J.; Renth, F.; Temps, F. Electronic and Steric Effects on the Photo-Induced C → E Ring-Opening of Structurally Modified Furylfulgides. *Phys. Chem. Chem. Phys.* **2011**, *13* (34), 15699–15707. https://doi.org/10.1039/C1CP21320B.

(287) Wollscheid, N.; Günther, B.; Rao, V. J.; Berger, F. J.; Lustres, J. L. P.; Motzkus, M.; Zaumseil, J.; Gade, L. H.; Höfener, S.; Buckup, T. Ultrafast Singlet Fission and Intersystem Crossing in Halogenated Tetraazaperopyrenes. *J. Phys. Chem. A* **2020**, *124* (39), 7857–7868. https://doi.org/10.1021/acs.jpca.0c04852.

(288) Schnedermann, C.; Alvertis, A. M.; Wende, T.; Lukman, S.; Feng, J.; Schröder, F. A. Y. N.; Turban, D. H. P.; Wu, J.; Hine, N. D. M.; Greenham, N. C.; Chin, A. W.; Rao, A.; Kukura, P.; Musser, A. J. A Molecular Movie of Ultrafast Singlet Fission. *Nat. Commun.* **2019**, *10* (1), 4207. https://doi.org/10.1038/s41467-019-12220-7.

(289) Alagna, N.; Han, J.; Wollscheid, N.; Perez Lustres, J. L.; Herz, J.; Hahn, S.; Koser, S.; Paulus, F.; Bunz, U. H. F.; Dreuw, A.; Buckup, T.; Motzkus, M. Tailoring Ultrafast Singlet Fission by the Chemical Modification of Phenazinothiadiazoles. *J. Am. Chem. Soc.* **2019**, *141* (22), 8834–8845. https://doi.org/10.1021/jacs.9b01079.

Publications

For this work, relevant publications:

May 2023: Pan Li, Sven H. C. Askes, **Esther del Pino Rosendo**, Freek Ariese, Charusheela Ramanan, Elizabeth von Hauff, and Andrea Baldi. *Nanoscale Thermometry of Plasmonic Structures via Raman Shifts in Copper Phthalocyanine*. DOI: 10.1021/acs.jpcc.3c01561

February 2023: **Esther del Pino Rosendo**, Okan Yildiz, Wojciech Pisula, Tomasz Marszalek, Paul W. M. Blom, and Charusheela Ramanan. *Symmetry-breaking charge transfer and intersystem crossing in copper phthalocyanine thin films*. DOI: 10.1039/D2CP05240G

March 2022: Kai Philipps, Yutaka Ie, Bas van der Zee, Rui-Qi Png, Peter K. H. Ho, Lay-Lay Chua, **Esther del Pino Rosendo**, Charusheela Ramanan, Gert-Jan A. H. Wetzelaer, Paul W. M. Blom, and Jasper J. Michels. *Role of Linker Functionality in Polymers Exhibiting Main-Chain Thermally Activated Delayed Fluorescence*. DOI: 10.1002/advs.202200056

June 2020: Irina Rörich, Quan Niu, Bas van der Zee, **Esther del Pino Rosendo**, Nicoleta Irina Crăciun, Charusheela Ramanan, and Paul W. M. Blom. *Exciton Quenching due to Hole Trap Formation in Aged Polymer Light-Emitting Diodes.* DOI: 10.1002/aelm.201700643

Other Publications:

https://www.researchgate.net/profile/Esther-Del-Pino-Rosendo/research

Curriculum Vitae